FINAL REPORT

Data and Processing Tools for Sonar Classification of Underwater UXO

SERDP Project MR-2230

AUGUST 2015

Raymond Lim
Naval Surface Warfare Center Panama City

Distribution Statement A
This document has been cleared for public release

SERDP
DOD ▪ EPA ▪ DOE

REPORT DOCUMENTATION PAGE

Form Approved
OMB No. 0704-0188

Public reporting burden for this collection of information is estimated to average 1 hour per response, including the time for reviewing instructions, searching existing data sources, gathering and maintaining the data needed, and completing and reviewing this collection of information. Send comments regarding this burden estimate or any other aspect of this collection of information, including suggestions for reducing this burden to Department of Defense, Washington Headquarters Services, Directorate for Information Operations and Reports (0704-0188), 1215 Jefferson Davis Highway, Suite 1204, Arlington, VA 22202-4302. Respondents should be aware that notwithstanding any other provision of law, no person shall be subject to any penalty for failing to comply with a collection of information if it does not display a currently valid OMB control number. **PLEASE DO NOT RETURN YOUR FORM TO THE ABOVE ADDRESS.**

1. REPORT DATE *(DD-MM-YYYY)*
24-09-2015

2. REPORT TYPE
final

3. DATES COVERED *(From - To)*
Apr 2012 - Jul 2015

4. TITLE AND SUBTITLE

Data and Processing Tools for Sonar Classification of Underwater UXO

5a. CONTRACT NUMBER

5b. GRANT NUMBER

5c. PROGRAM ELEMENT NUMBER
0603716D87

5d. PROJECT NUMBER
MR 2230

5e. TASK NUMBER

5f. WORK UNIT NUMBER

6. AUTHOR(S)

Raymond Lim

7. PERFORMING ORGANIZATION NAME(S) AND ADDRESS(ES)

Naval Surface Warfare Center Panama City Division
110 Vernon Ave
Code X11
Panama City, FL 32407

8. PERFORMING ORGANIZATION REPORT NUMBER

9. SPONSORING / MONITORING AGENCY NAME(S) AND ADDRESS(ES)

SERDP and ESTCP Office
4800 Mark Center Drive
Suite 17D08
Alexandria, VA 22350-3605

10. SPONSOR/MONITOR'S ACRONYM(S)

11. SPONSOR/MONITOR'S REPORT NUMBER(S)

12. DISTRIBUTION / AVAILABILITY STATEMENT

Approved for Public Release; distribution is unlimited.

13. SUPPLEMENTARY NOTES

14. ABSTRACT

Under SERDP project MR-2230, NSWC PCD worked towards resolving issues affecting sonar detection and classification/identification (C/ID) of underwater UXO. Two main objectives were: 1) build a database of realistic sonar responses from UXO and clutter targets deployed in sand and mud underwater environments that could be used to develop and evaluate C/ID algorithms for separating UXO from bottom clutter and 2) use this database to search for physics-based features capable of robust automated target recognition (ATR) performance.

15. SUBJECT TERMS

acoustic scattering, automated target recognition, classification, feature vector, finite element method, resonance, ROC curve, time-frequency distribution, target strength

16. SECURITY CLASSIFICATION OF:			**17. LIMITATION OF ABSTRACT**	**18. NUMBER OF PAGES**	**19a. NAME OF RESPONSIBLE PERSON**
					Raymond Lim
a. REPORT	**b. ABSTRACT**	**c. THIS PAGE**	SAR	64	**19b. TELEPHONE NUMBER** *(include area code)* 850-235-5178

Standard Form 298 (Rev. 8-98)
Prescribed by ANSI Std. Z39.18

Table of Contents

Data and Processing Tools for Sonar Classification of Underwater UXO i
Table of Contents ii
Table of Figures ii
List of Tables iv
Acronyms iv
Keywords v
Acknowledgements v
Abstract 1
Objective/Background 2
Materials and Methods 2
Controlled field measurements: 4
Finite Element (FE) simulations/model development: 7
ATR processing and analysis tools: 10
Results and Discussion 12
FE simulations/model development: 20
Classification analysis of shallow grazing angle data: 30
..... 37
..... 38
Classification analysis of high grazing angle data: 41
Conclusions and Implications for Future Research/Implementation 49
Literature Cited 51
APPENDIX A: Supporting Data 53
List of FEM models built 54
APPENDIX B: List of Scientific/Technical Publications 56
Journal/Conference publications: 57
Conference/Symposium Abstracts: 57

Table of Figures

Figure 1. TREX 2012-13 and BAYEX 2014 sites. 5
Figure 2. A target deployment utilized in TREX 2012. 5
Figure 3. Typical target layout at TREX 2013. 6
Figure 4. Typical target layout at BAYEX 2014 with targets labeled according to Table 3. 8
Figure 5. Acoustic color plot for backscatter by a buried solid steel cylinder in NSWC PCD's small-scale test bed facility. 11
Figure 6. SAS imagery processed from TREX data collected in 2012. 13
Figure 7. Target strength plots of the four targets located at a ground range of 15 m. Top and bottom rows refer to the 105 mm artillery round and 155 mm Howitzer shell, respectively. Left and right column are associated with the west and east target, respectively. 13
Figure 8. Sample SAS imagery of targets deployed at (a) shorter ranges and (b-e) longer ranges processed from the 2013 TREX. 15
Figure 9. A comparison of acoustic color for a partially buried 105 mm artillery round UXO processed from (a) 2013 TREX data and (b) NSWC PCD pond data. 15
Figure 10. FEM-computed surface field displacements are displayed for the 105 mm artillery round deployed proud on a sand seafloor. In (a), an 8 kHz plane wave incident at 220° aspect and 21.5^o grazing excites the UXO into a horizontal bending mode. In (b), an 18.5 kHz plane wave at 180° aspect and 21.5^o grazing excites the UXO into a vertical wave mode along the length of the round. 16
Figure 11. An illustration of the dependence of acoustic color on range for a proud 100 mm Al UXO replica deployed during TREX. The replica is at 15 m range in (a) and 40 m in range in (b). 17

Figure 12. A matrix showing the cross-correlation magnitude between the acoustic color plots of TREX targets in Table 4. 18
Figure 13. An illustration of the dependence of acoustic color on range for a proud 100 mm Al UXO replica deployed during BAYEX. The replica is at 10 m range in (a) and 25 m in range in (b). 19
Figure 14. A matrix showing the cross-correlation magnitude between the acoustic color plots of BAYEX targets in Table 5. 19
Figure 15. Acoustic color plots corresponding to full 3-D FE simulations of a partially buried 105 mm artillery round in (a) proud, (b) half-buried, and (c) 55° tilted configurations. 20
Figure 16. Sample calculations of acoustic color for more complex UXO and clutter configurations. On the left is a group of UXO consisting of a pair of proud horizontal 155 mm Howitzer shells with a tilted 105 mm artillery round embedded in the sediment between. On the right is a tire with a cinder block in the middle. 21
Figure 17. Schematic of the 155 mm Howitzer deployed in TREX, with different material components distinguished by color. 22
Figure 18. A comparison of acoustic color plots for a proud Howitzer shell, insonified at about 20° grazing and processed from (a) circular rail pond data, (b) 3D FEM simulated data using assumed parameters for the orange ceramic band, and (c) 3D FEM simulated data assuming the ceramic band is steel. 23
Figure 19. The GUI for the Matlab-based visualization tool created to read and animate surface displacement fields on targets simulated via NSWC PCD's 3D FEM software. 24
Figure 20. Acoustic color plots generated from free-field FEM calculations for the proud 100 mm Al replica UXO. Dominant target-seafloor multipaths are added in to mimic TREX deployments at grazing angles (a) 5°, (b) 10°, (c) 15°, (d) 20°, and (e) 25°. 25
Figure 21. Acoustic color plots generated from free-field FEM calculations for the proud 100 mm Al replica UXO. Dominant target-seafloor multipaths and noise from seafloor roughness are added in to mimic TREX deployments at grazing angles (a) 5°, (b) 10°, (c) 15°, (d) 20°, and (e) 25°. 26
Figure 22. Acoustic color plots generated by PC SWAT from free-field FEM calculations to approximate environmental effects for a flush buried (left) and proud (right) 100 mm Al replica UXO deployed on mud at a range of 10m. Dominant target-seafloor multipaths are added in for the proud case to mimic BAYEX deployment on a mud halfspace. 27
Figure 23. A comparison of the backscatter form-function of a 10:1 prolate Al spheroid computed with the new spherical-basis T matrix (red) and NSWC PCD's spheroidal-basis benchmark (black). 30
Figure 24. (a) ROC curve for class separating all UXO (entries 1-11) in Table 3. (b) Pd and Pfa curves used to generate ROC curve. 31
Figure 25. (a) ROC curve for class separating all 105 mm artillery round cases in Table 3. (b) Pd and Pfa curves used to generate ROC curve. 32
Figure 26. (a) ROC curve for class separating all 100 mm UXO shapes in Table 3. (b) Pd and Pfa curves used to generate ROC curve. 32
Figure 27. ROC curves for separating all UXO from clutter in Table 6 by correlating against templates in selected low-pass frequency bands. In the three cases shown the templates used as UXO exemplars correspond to: (a) all templates in Table 7, (b) only simulated templates in Table 7, and (c) only experimental pond templates. 36
Figure 28. ROC curves for separating all UXO from clutter in Table 6 by correlating against templates in selected 5 kHz bandwidth intervals. In the three cases shown the templates used as UXO exemplars correspond to: (a) all templates in Table 7, (b) only simulated templates in Table 7, and (c) only experimental pond templates. 37
Figure 29. ROC curves for separating all UXO from clutter in Table 6 by correlating against templates in selected high-pass frequency bands. In the three cases shown the templates used as UXO exemplars correspond to: (a) all templates in Table 7, (b) only simulated templates in Table 7, and (c) only experimental pond templates. 38

Figure 30. ROC curves for separating all UXO from clutter in Table 6 by correlating data in selected aspect windows against the Table 7 templates. In the three cases shown, the width of the data aspect windows are: (a) 15°, (b) 30°, and (c) 45°. 40
Figure 31. Binomial TFD plots of circular rail test pond data for an aluminum replica of a 100 mm UXO target. (a) Proud. (b) Partially buried. 42
Figure 32. Born-Jordan TFD plot of circular rail test pond data for a proud aluminum replica of a 100 mm UXO target. A whispering-gallery wave is exhibited in this TFD. 42
Figure 33. Binomial TFD results for 4 target types. 43
Figure 34. Beamformed and mosaicked image of TREX field from the BOSS system. 44
Figure 35. Target type N4 data from Pond and TREX 45
Figure 36. Target type T25 data from Pond and TREX 45
Figure 37. Power spectra of the same target collected by different systems in two underwater environments with sand sediment. The WG-PR sequences are marked on the red line. 46
Figure 38. 2-D Principal Coordinate plane created by transforming 4-D feature vectors. The blue stars are buried 155 mm Howitzer shells. 48
Figure 39. k-means clustering based on 2-D Principal Coordinates. The black asterisk cluster contains all buried 155 mm Howitzers along with a few cylindrical proud targets. 48
Figure 40. k-means clustering based on 2-D Principal Coordinates where an estimate of the burial state was included in the feature vector for each target. Burial state can be determined from the beamformed volumetric created by beamforming BOSS data. Adding burial state as an element in the feature vector before principal coordinate analysis separates the buried Howitzers (blue asterisks) from the other targets in the field. 49

List of Tables

Table 1. Original TREX13 Targets 6
Table 2. Additional Targets Provided by NRL 6
Table 3. BAYEX 2014 TARGET LIST 7
Table 4. Legend for Fig. 12 Correlation Matrix 18
Table 5. Legend for Fig. 14 Correlation Matrix 19
Table 6. Targets and clutter with descriptions 34
Table 7. Templates with descriptions 34

Acronyms

Al - Aluminum
APL-UW – Applied Physics Laboratory at University of Washington
ATR – Automated Target Recognition
BAYEX – Bay Experiment
BOSS – Bottom Object Scanning Sonar
C/ID – Classification/Identification
COMSOL – software trade name, formerly FEMLAB
DEU – Diver Evaluation Unit
FAU – Florida Atlantic University
FE – Finite Element
FEM – Finite Element Method
FY – Fiscal Year
GUI – graphical user interface
IEEE – Institute of Electrical and Electronics Engineers
k – wave number

kHz – kilohertz
L – longest dimension of target
Matlab - software trade name, Matrix laboratory
MHz – MegaHertz
NRL – Naval Research Laboratory
NSWC PCD – Naval Surface Warfare Center Panama City Division (formerly CSS and NCSC)
ONR – Office of Naval Research
PC SWAT – Personal Computer Shallow Water Acoustic Toolset
P_d – Probability of correct classification
P_{fa} – Probability of False Alarm
PR – Pseudo-Rayleigh
ROC – Receiver Operating Characteristics
R/V – Research Vessel
SAS – Synthetic Aperture Sonar
SERDP – Strategic Environmental Research and Development Program
SNR – Signal-to-Noise Ratio
T-matrix – Transition matrix
TFD – Time-Frequency Distribution
TREX – Target Reverberation Experiment
UXO – UneXploded Ordnance
WG – Whispering Gallery
WSU – Washington State University
X – NSWC PCD organizational code

Keywords

acoustic scattering, automated target recognition, classification, feature vector, finite element method, resonance, ROC curve, time-frequency distribution, target strength, template matching, transition matrix

Acknowledgements

Several people contributed their efforts to the tasks described in this report for developing a non-imaging sonar classification capability for underwater UXO. Dr. Joseph L. Lopes coordinated much of the NSWC PCD logistics support of TREX and BAYEX. Mr. D. Malphurs and Ms. I. Paustian participated in the data collection, data processing, and analysis. Dr. K. Lee developed and ran the FEM target models and Dr. G Sammelmann combined the FEM results with PC SWAT to produce the simulations used as exemplar acoustic color templates for matching with the TREX and BAYEX results. Dr. J. Prater and Mr. R. Arrieta initiated the non-image template-matching and cluster-analysis schemes, respectively, for class separating UXO from the TREX and BAYEX data.

Data and Processing Tools for Sonar Classification of Underwater UXO

POC: Dr. Raymond Lim
Naval Surface Warfare Center Panama City Division, Code HS-11, 110 Vernon Ave.
Panama City, FL, 32407, 850-235-5178, raymond.lim@navy.mil

Abstract

Objectives: Under SERDP project MR-2230, NSWC PCD worked towards resolving issues affecting sonar detection and classification/identification (C/ID) of underwater UXO. Two main objectives were: 1) build a database of realistic sonar responses from UXO and clutter targets deployed in sand and mud underwater environments that could be used to develop and evaluate C/ID algorithms for separating UXO from bottom clutter and 2) use this database to search for physics-based features capable of robust automated target recognition (ATR) performance.
Technical Approach: The primary effort towards building the UXO database involved providing logistical and technical support for three controlled sonar measurements from a linear rail deployed in the Gulf of Mexico off Panama City, FL in 2012-2013 and in St. Andrews Bay off Panama City, FL in 2014. These measurements leveraged Navy sponsored bottom reverberation and target scattering experiments led by Applied Physics Laboratory at the University of Washington (APL-UW) to collect sonar data from targets deployed on a sand and a mud ocean floor. A secondary effort to augment existing databases using finite element method (FEM) and T-matrix modeling was also carried out. Both sets of data were processed to check sonar model simulations against more realistic data for UXO applications and to further the evaluation of backscatter phenomena for extraction of classification features. Classification analysis of this data was carried out by projecting target strength onto two primary spaces: frequency vs target aspect and frequency vs time. The frequency-aspect (acoustic color) representation was primarily used for targets detected at long ranges/shallow grazing angles, where aspect-dependent phenomena are most distinguishable and useful for carrying out template-matching studies. The time-frequency representation was used for high grazing angle data at aspects exhibiting strong backscatter such as broadside so that the viability of resonance-based features could be studied.
Results: A database of target responses has been assembled from the field experiments and from simulated data for targets deployed proud and buried in a sand and mud seafloor. These data represent responses of the target over a full 360° aspect range, a 5-30 kHz frequency band, and deployment ranges of 5-40m corresponding to grazing angles from 36° to 5°, respectively. The use of simulated data to augment target databases is found to be a worthwhile alternative to costly data collection but accurate input parameters are needed. Input parameters such as target dimensions, casing material moduli, environmental layering, and environmental material parameters can vary enough that generic values can produce poor simulation matches with experiments. Template-matching studies were performed on the data processed into acoustic color plots. These studies were used to demonstrate discrimination trends under various conditions that show what parameters template-based discrimination is sensitive to. Template matching of data processed into time-frequency plots was also tried but with less success due to sensitivity to processing parameters. However, algorithms to extract parameters associated with resonances in the frequency spectrum were devised and these parameters were used to form feature vectors. When fed to a clustering algorithm, these feature vectors appear to cluster difficult UXO targets reasonably well.
Benefits: The results of this project will help further the development of ATR for underwater UXO by providing a database of UXO sonar responses for algorithm testing and training. Analysis performed so far should provide classification benchmarks to guide future directions to pursue.
.

Objective/Background

State and national concerns continue to grow over the dangers posed by unexploded ordnance (UXO) dropped or disposed of underwater along US coastlines, rivers, and other bodies of water near communities since the Civil War. For this reason, SERDP maintains a call for research to work towards detecting, classifying and remediating this danger. The research performed in this project responds to needs outlined in SERDP's statement of need MRSON-12-02. Here studies focusing on "the phenomenology of underwater munitions and underwater site conditions that impact their detection by magnetic, electromagnetic induction, optical and acoustic sensors" are called for. Understanding the phenomenology dictating the response of targets within its environment is expected to not only lead to better sensor choices for detection but better features for classification. In particular, the Navy has developed sonar into a proven technology for detection and discrimination of underwater objects on the order of 1m in size or larger from clutter through analysis of image features. However, new features need to be identified for many UXO because their smaller size make them harder to distinguish from clutter, and difficulties arise for buried ordnance (like many UXO) because the wave attenuation and inhomogeneity in ocean sediments make detection with sonar less predictable and high-resolution imaging more difficult. In fact, imaging with state-of-the-art sonar designed for sub-bottom objects, such as the Bottom Object Scanning Sonar (BOSS) designed by Florida Atlantic University (FAU) for the Navy, shows important image features (e.g., highlight/shadow features) are lost with burial and, because resolution is on the order of several inches, image-based classification of UXO approaching this size is unreliable.

Of particular interest in this effort are identifying target phenomena in sonar data yielding new features with robust discriminatory power for separating UXO from clutter. Searching for such phenomena requires a database of sonar target responses that represents desired targets under a wide variety of environmental conditions. One of the goals of this project is to build such a database with realistic sonar responses from UXO and clutter targets deployed in sand and mud underwater environments. Another goal is to use this database to search for physics-based features that could be used to develop and evaluate classification/identification (C/ID) algorithms for separating UXO from bottom clutter without imaging. Therefore, modeling, data collection, and data analysis is performed as a means to achieve these goals by enabling an understanding of factors that affect the acoustic response of proud and buried munitions when searched with both side-scan sonar used for wide area assessment and bottom-looking sonar for detection of completely buried targets. The knowledge gained would be used to

- test new ways to improve signal-to-noise (SNR) against targets
- improve ability to discriminate UXO from clutter
- validate simulation software for generating sonar data
- enable UXO sonar performance prediction.

This final report will summarize the results obtained towards these goals.

Materials and Methods

Key to developing a robust sonar-based classification capability against UXO is a sufficiently representative database of target responses that can be analyzed for discriminatory features.

Unless the range of feature variability that targets and clutter can exhibit is well represented in the database available, which is typically not known *a priori*, automated target recognition (ATR) algorithms trained on the chosen features are not assured of robustness when tested against new data sets. Thus, deceptively high performance can result from testing against limited data sets. Because collecting sufficient data for training can be very costly, the approach taken to develop the ATR component of sonar performance combines results of several efforts to help ensure a diverse set of data for classifier training and testing is created.

At NSWC PCD, several efforts have been initiated in past projects to facilitate the population of a usable database, including development of a 3D finite element method (FEM) modeling capability for realistic UXO and dedicated UXO and clutter measurements in NSWC PCD's pond facilities (Fig. 1) [1]. In the current project, an effort to acquire more realistic data was made by leveraging Office of Naval Research (ONR) sponsored seafloor reverberation and target scattering measurements in 2012-2014. These measurements, led by the Applied Physics laboratory at the University of Washington (APL-UW) were run in collaboration with NSWC PCD in the Gulf of Mexico and in St. Andrews Bay off Panama City, FL. In 2012, SERDP funded NSWC PCD to provide the additional logistics support needed to augment APL-UW's reverberation study to include integration of sonar used in past NSWC PCD's pond measurements onto APL-UW's rail and to run operational checks to ensure feasibility of data collection using the rail in a sandy area of the Gulf. In 2013, a follow-on measurement was carried out to collect data on several UXO and clutter targets deployed under water on a sandy area of the Gulf. Further measurements against targets deployed in a muddy area of St Andrew Bay off Panama City were performed in 2014.

In conjunction with the Gulf and Bay measurements, 3D FEM calculations of the acoustic response for many of the new targets deployed were carried out both in free-field and in proud configurations. Free-field measurements in NSWC PCD's tank facilities were also collected for comparison. These were meant to check that both the environmental and target parameter inputs used in the simulations would produce responses that match both field measurements sufficiently. The free-field measurements and calculations were also used to generate fast, approximate simulations of the proud target responses by summing appropriate target-bottom echoes with the free-field direct echo as suggested in recent target scattering work [2]. The purpose of the approximate simulations is to provide a practical means to produce a diverse database of target responses for use in ATR training and in investigating the discrimination potential of phenomena exhibited in processed data. An important component of our approach is to assess the quality of our simulated database by training ATR on features extracted from it and performance testing against real data such as that collected in field experiments.

Given a viable database of target responses, an effort was carried out to identify and extract features for ATR training from it based on phenomena associated with elastic waves excited on the target. Such phenomena would be expected to exhibit unique signatures in acoustic color (i.e., target strength as a function of target aspect angle and frequency) or time-frequency plot representations of the associated target responses. Of particular interest are phenomena that aren't strongly modified by sediment loading or damping (e.g., low-frequency resonances) so that burial doesn't strongly affect the response. The premise is that training data requirements

can be reduced if target characteristics known to be unique to UXO can be found. More details for these efforts are as follows.

Controlled field measurements:
Dr. J. Lopes coordinated the logistics support from NSWC PCD required to carry out a preliminary sonar/rail integration test in 2012, the sonar data collection in 2013 in the Gulf of Mexico off Panama City, FL, and the sonar data collection in 2014 in St. Andrews Bay off Panama City, FL. The data collection sites are indicated in Fig. 1. As noted above, all of these efforts leveraged additional seafloor reverberation and target scattering experiments funded by ONR and led by researchers from APL-UW (Drs. S. Kargl and K. Williams). The joint operations became known as Target Reverberation Experiments (TREX) in 2012-13 and Bay Experiments (BAYEX) in 2014. Through both SERDP and ONR support, NSWC PCD was tasked with enabling the target scattering component of these measurements in several ways. In particular, NSWC PCD secured the environmental approvals for testing in waters off Panama City, prepared the test plans subsequently approved by NSWC PCD's Test Safety Review Board, provided test directors and safety observers in accordance with regulations governing operations in the Gulf utilizing government facilities and personnel, provided facility and support services (e.g., transportation, forklift, and crane services, building bay and dock space for assembly and breakdown of equipment, and research vessel docking for loading and off-loading), and provided base escorts for foreign national researchers in accordance with federal security regulations.

Underwater UXO and clutter targets from NSWC PCD's inventory, including new UXO transferred from the Naval Research Laboratory (NRL), were provided for the field deployment and used in the target response measurements. Figure 2 shows a typical target layout for data collection in 2012 at the TREX sand site in Fig. 2. The rail deployed consisted of six 7 m sections connected together to carry a sonar platform along a linear track nominally 40 m long, holding the sonar about 3.6 m above the seafloor. All targets were deployed proud of the surface along several lines parallel to the rail and separated at 5m range increments out to 40m. This allowed target data to be collected at grazing angles from about 36° near the rail to about 5° at the 40m line. Targets were rotated by APL-UW divers in predetermined increments to collect backscatter data from each target over a wide aspect range. Although data collected in 2012 helped to augment existing target response databases for ATR investigations, processing of this data was primarily meant to assess integration of sonar spanning a nominal 5-30 kHz band onto APL-UW's rail for the following tests in 2013 and 2014. Of particular importance was to make sure reverberation with rail structures and cross-talk between transmit and receive channels were not significant and that sonar parameters such as beam orientation, bandwidth, and signal level were controllable and within operational expectations. This was assessed from processed imagery and plots of target strength as a function of aspect and frequency (i.e., acoustic color).

TREX 2013 and BAYEX 2014 were planned to allow target responses to be collected from a variety of targets and clutter in a sandy and muddy underwater environment, respectively. Data were collected as a function of target aspect, frequency, range, and degree of burial. To accommodate all of these variations a fairly diverse set of targets were chosen and deployed in various configurations. Tables 1 and 2 list the set of targets used at TREX 2013. A sample configuration utilized at TREX 2013 is depicted in Fig. 3. As in 2012, divers were utilized to rotate proud targets and to bury targets as needed. After data were collected at a particular range,

divers would redeploy the targets at a different location in the target field. This permitted broadband, multi-aspect data at different ranges for the same target to be collected.
Five different target field configurations were utilized in 2013. Data were processed by projecting onto spaces suitable for extracting ATR features such as image and acoustic color. Due to the close proximity of neighboring targets, an isolation technique was applied to the complex SAS image data to separate backscattered signals so that acoustic color could be

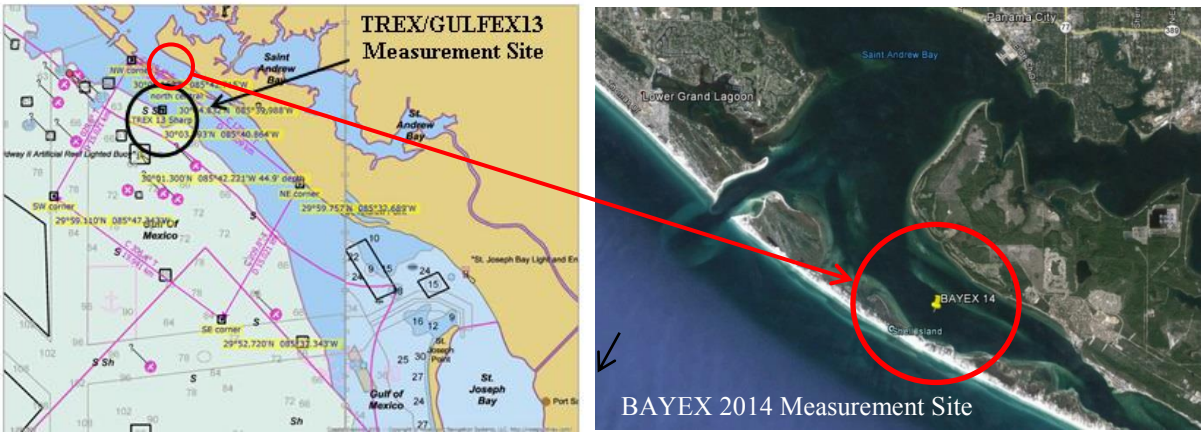

Figure 1. TREX 2012-13 and BAYEX 2014 sites.

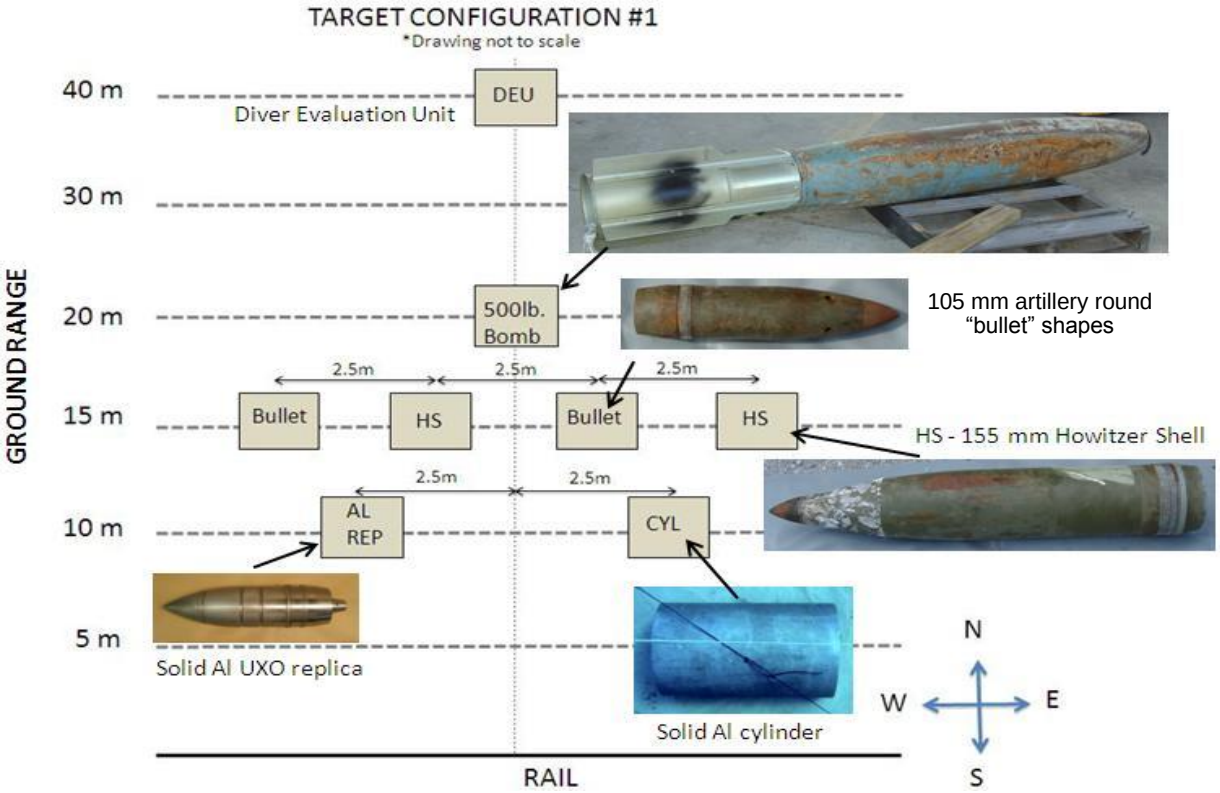

Figure 2. A target deployment utilized in TREX 2012.

Table 1. Original TREX13 Targets

Target #	Target Name
1	DEU trainer
2	Rock
3	55-gallon drum, water filled w/ fixture
4	XXXXXXXXXXXXXXXXXX
5	5:1 aspect telephone pole section
6	55-gallon drum, water-filled
7	3 ft alum cylinder
8	155 mm Howitzer w/o collar
9	155 mm Howitzer w/ collar
10	panel target - Dan Brown
11	152 mm TP-T
12	81 mm mortar
13	Scuba tank, water-filled, w/o stem
14	Scuba tank, water-filled, w/ stem
15	2:1 aspect telephone pole section
16	2 ft alum pipe
17	2 ft alum cylinder
18	Cement block
19	Tire
20	Alum UXO replica
21	Steel UXO replica
22	Original material UXO
23	Solid alum cylinder w/ notch
24	Hollow alum cylinder w/notch
25	Bullet #1
26	XXXXXXXXXXXXXXXXXX
27	XXXXXXXXXXXXXXXXXX
28	155 mm Howitzer w/ collar
29	Bullet #2
30	Finned Shell #1

Table 2. Additional Targets Provided by NRL

N1 5" rocket nose up 60 deg
N2 5" rocket nose up 30 deg
N3 5" rocket horizontal
N4 155mm howitzer horizontal
N5 155mm howitzer horizontal 90 deg
N6 155mm howitzer horizontal 20 cm buried
N7 155mm howitzer nose up 30 deg
N8 155mm howitzer nose up 60 deg
N9 120mm mortar horizontal
N10 large rock
N11 cinder block

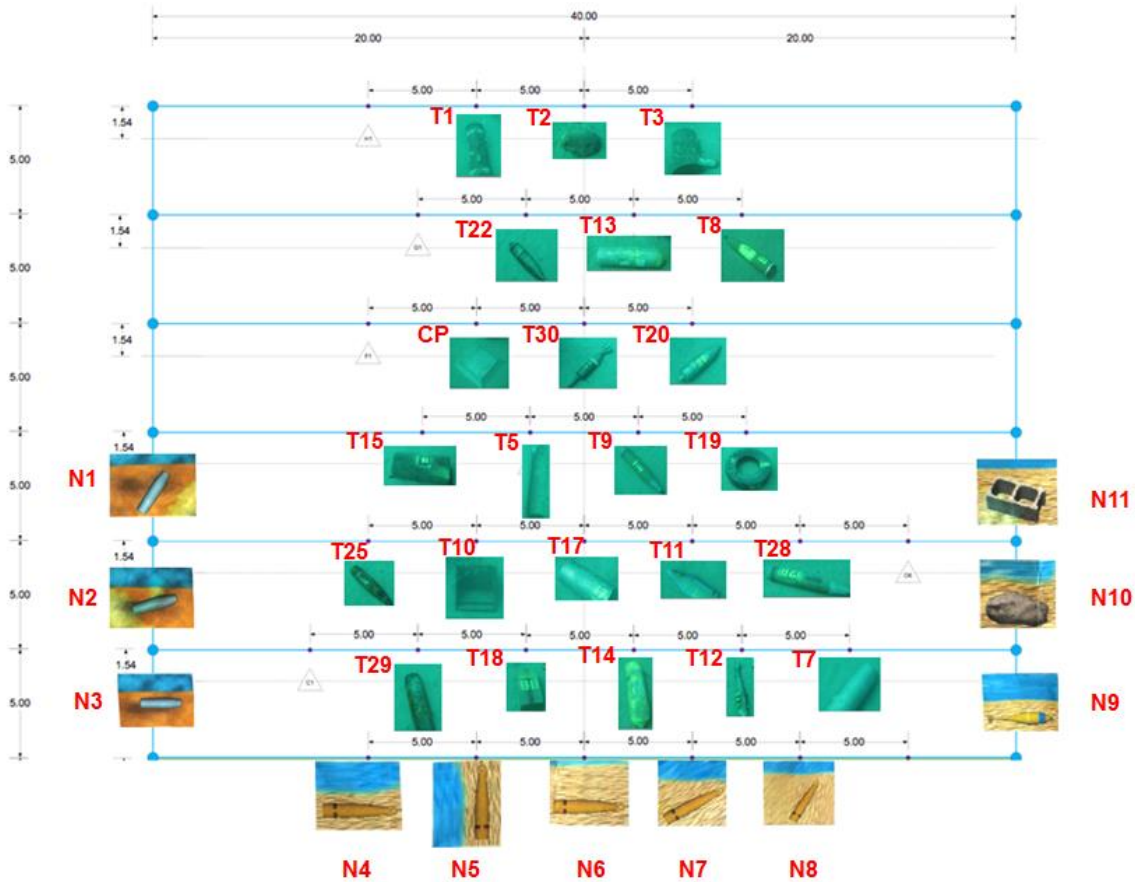

Figure 3. Typical target layout at TREX 2013.

extracted with less noise. The spectral target strength levels from a particular target were determined by removing spreading losses using the sonar equation and a scaling constant. This process was repeated for each of the target rotations, and the data segments were stitched together using a process that averaged overlapping angular sectors.

Compared to TREX, BAYEX in 2014 utilized a site consisting of a mud layer over sand. Divers measured mud layer thicknesses from 2-8 in out to 15 m from the rail and deepening beyond to about 12 in out at the farthest line of deployed targets. The softness of the mud often resulted in difficulties controlling the burial depth of deployed targets so divers measured depths after deployment. The list of targets utilized at BAYEX is given in Table 3. Figure 4 shows one of the four target configurations deployed with targets labeled according to Table 3. Data were processed as for the TREX data.

Finite Element (FE) simulations/model development:
As mentioned above, FEM calculations were carried out to build a database of simulated acoustic target and clutter responses to use for ATR training as well as in analysis of target physics that might lead to improved feature selection for targets of interest. 3D FEM calculations were carried out by Dr. K. Lee on a variety

Table 3. BAYEX 2014 TARGET LIST

Target #	Target Name	Comments
1	DEU trainer	zinc end=tail
2	Rock	arrow points to nose
3	55-gallon drum, water filled w/ fixture	open end=tail
4	5:1 alum cylinder	
5	NOT DEPLOYED	
6	55-gallon drum, water-filled	open end=tail
7	3 ft alum cylinder	
8	155 mm Howitzer w/o collar	
9	NOT DEPLOYED	
10	NOT DEPLOYED	
11	152 mm TP-T	
12	81 mm mortar	
13	Scuba tank, water-filled, w/o stem	Stem=nose
14	Scuba tank, water-filled, w/ stem	Stem=nose
15	NOT DEPLOYED	
16	2 ft alum pipe	
17	2 ft alum cylinder	
18	Cement block	
19	Tire	
20	Alum UXO replica	
21	Steel UXO replica	
22	Original material UXO	
23	Solid alum cylinder w/ notch	Notch=tail
24	Hollow alum cylinder w/notch	Notch=tail
25	Bullet #1	
26	NOT DEPLOYED	
27	XXXXXXXXXXXXXXXXXXX - M	
28	155 mm Howitzer w/ collar	
29	Bullet #2	
30	Finned Shell #1	
31	XXXXXXXXXXXXXXXXXXX - C	
32	XXXXXXXXXXXXXXXXXXX - R	
33	Alum UXO Replica	

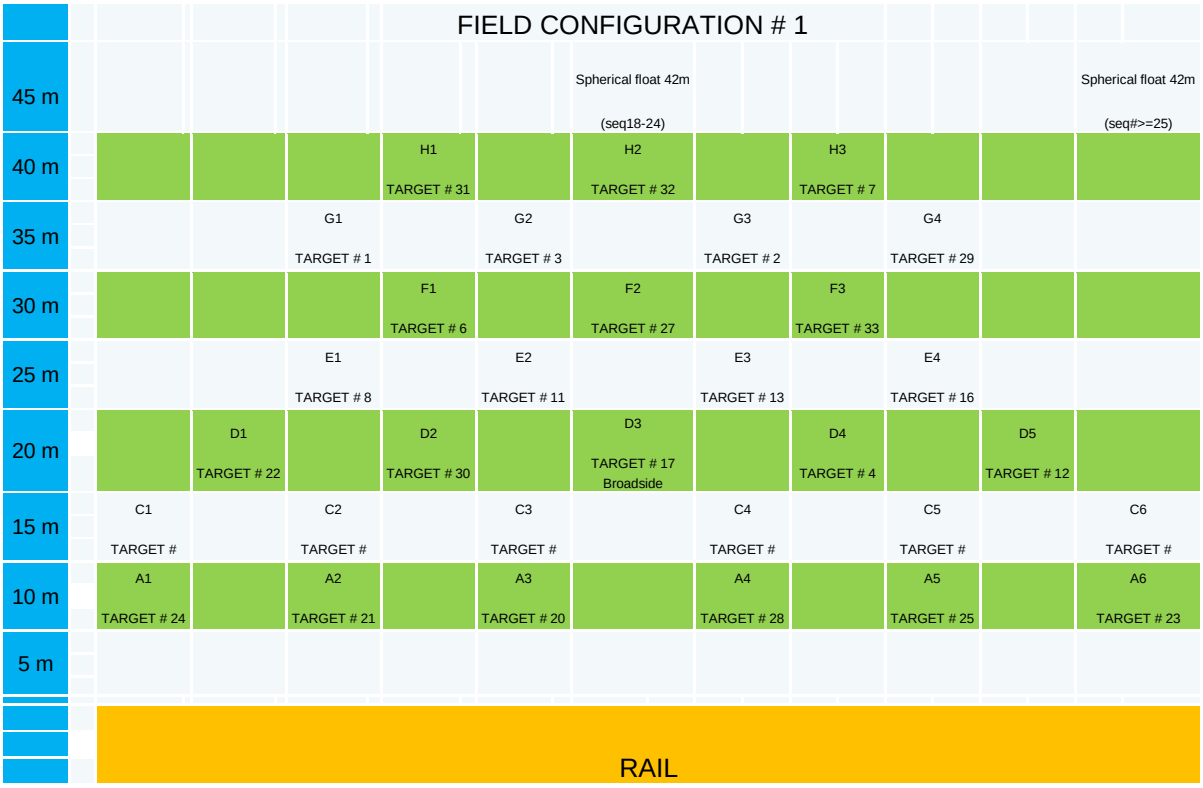

Figure 4. Typical target layout at BAYEX 2014 with targets labeled according to Table 3.

of objects both in free field and deployed on sand and mud bottoms but the targets and clutter planned for deployment in the TREX and BAYEX measurements were emphasized in these calculations. An effort was made to ensure these calculations were faithful representations of the targets deployed by validating against free-field and pond data collected by leveraging ONR funded efforts. Although the 3D FEM algorithms used have been shown to be very reliable, accuracy of the computed results is still subject to convergence limitations set by available memory resources and the accuracy of inputs. Ways to mitigate these issues were necessarily devised as part of the database generation.

For larger targets, convergence degradation was found to become noticeable when frequencies corresponding to scaled values $kL/2>50$ were computed, where k is the wavenumber of water and L is the longest dimension of the target. A careful analysis of the errors incurred as a function of frequency was carried out to refine the algorithm that determines the mesh densities used in FEM target models. Since the rack computer built for NSWC PCD's FEM calculations is currently equipped with the maximum memory possible, adopting a simple linear increase in model mesh density with frequency to improve convergence conflicted with available memory. The refinements made were meant to enable allocation of available memory at lower frequencies for denser meshing in a nonlinear fashion consistent with where errors were greatest. The errors were assessed on a gross level by inspecting the level of numerical noise or rate of convergence

exhibited in calculations or, on a more refined level, by comparisons with data calculated for simple benchmark shapes using spheroidal basis T-matrix algorithms.

Comparisons of FEM target responses for a few of the new UXO with measured responses also exhibited significant departures that were the result of inaccurate inputs due to incorrectly tabulated or unmeasurable dimensions or incorrectly assumed material parameters. Most of the dimensional unknowns were resolved by cannibalizing a target when multiple copies were available. Where assumed material parameters were too far off to produce good agreement with measurements, techniques to measure them have been devised. Among the material inputs needed for acoustic predictions are density and the bulk compressional and shear wave speeds. Density is typically easy to determine for a shell that can be taken apart so that weight measurements can be carried out. High frequency (~40 MHz) time-of-flight acoustic measurements were utilized on shell components to determine bulk compressional speeds where possible. While not ideal, bulk shear speeds were generally estimated from tabulated values. For some UXO shapes, spectral features in the modeled acoustic backscatter are sensitive to the shear speed in the casing material. In this case, a more refined estimate of the bulk shear speed is possible by matching these features to the same features seen in measured data but this can require many FEM runs to determine the best fit.

In past work [1], the large body of simulations required to populate an ATR database motivated the development of a capability to import FEM or T-matrix data into PC SWAT, where it can be inserted into reflectivity maps generated from real field data to produce new data mixed with more realistic background noise. While this approach can generate extensive data sets, it can call for new FEM or T-matrix runs to be carried out when environmental parameters change. A faster approach when one wishes to vary environmental parameters only is to include an extra approximation where only free-field FEM or T-matrix scattering data is imported and only the dominant target-sediment interactions [2, 3] are summed into the target response. Therefore, when proud targets are considered, only the free-field in water responses of targets need be computed for insertion into environments with different sediment types. This simpler approach was carried out by Dr. G. Sammelmann to generate several data sets involving UXO deployed on different sand and mud sediments. Comparisons with TREX data were made to assess how well these approximations reproduce real data. In an effort to balance efficient generation of data sets without sacrificing the quality of features extracted for ATR development, these data will be used to assess the level of fidelity required.

Due to convergence degradation associated with the limited memory resources, 3D FEM calculations for larger targets may not be available over the full band of current measurements. Larger targets of simple structure (i.e., spheres, cylinders, cones, etc.) can still be computed using spheroidal T-matrix codes developed at NSWC PCD but, due to difficulties in calculating spheroidal basis functions at scaled frequencies beyond $kL/2>70$, this is not a great improvement. An attempt to remove this limitation was made by formulating and implementing a new spherical basis T-matrix algorithm adapted from ideas promoted recently by Waterman [4] and Doicu, et al. [5]. The techniques demonstrated by these authors appear capable of generating the scattering response of dielectric objects in electromagnetic scattering at much higher frequencies. In acoustic applications, they will be used to generate fast benchmark acoustic

results as well as allow fast modeling of high frequency phenomena intrinsic to the target, which greatly assists interpretation of these phenomena.

Comparisons of simulated data results with TREX results were generally done after projecting onto the acoustic color space. However, a capability to use intermediate results from the 3D FEM simulations to further physical interpretation of highlights in acoustic color plots was also implemented. This was done by using the complex surface displacement field computed at target surfaces to magnify and animate waves excited at the surface at a given frequency and target aspect. Since the FEM is used to produce frequency-domain solutions, the time dependence needed to animate the steady-state displacement field is simply $e^{-i\omega t}$, where ω is angular frequency and t is time. The position vector $\mathbf{D}(\mathrm{t})$ of a displaced surface element at time t relative to its initial undisplaced position $\mathbf{D}_0$ measured from a target-centered coordinate system is given by

$$\mathbf{D}(\mathrm{t}) = \mathbf{D}_0 + \mathrm{S_f}\,\mathrm{Re}(\,\mathbf{U}(\mathbf{D}_0)\,e^{i\omega t}).$$

where $\mathbf{U}$ is the complex displacement vector for the surface element at $\mathbf{D}_0$ and S_f [~(0.01-0.1)*10^{10}] is a scale factor used to magnify the distortion of the surface. By plotting $\mathbf{D}(\mathrm{t})$ for the entire target as a function of time, details of how waves are excited and travel around the target at particular acoustic color highlights can be seen and, perhaps, used to deduce useful relationships among the highlights or insight on their robustness under different conditions.

ATR processing and analysis tools:

The measurements and FE simulations performed provided data that can be used to train and test ATR algorithms. Non-image-based classification is of particular interest because small UXO are more difficult to image at the resolution needed to achieve high classification performance. A common non-image feature to extract from the available data is the level of correlation between target data represented as acoustic color, although this is expected to work best for detections with good SNR. Therefore, Dr. J. Prater carried out an initial correlation analysis of the proud target TREX data represented in acoustic color space against data collected with the circular rail in NSWC PCD's pond. A simple template matching scheme was devised where a subset of TREX data for which good acoustic color plots were generated were matched against a select set of color plots generated from UXO targets at a single range (~11 m) and grazing angle (~20°) in the pond. A simple correlation formula was used to extract the level of match and a threshold was varied to change the probability of false alarms and correct classifications so that ROC curves could be generated for several two-class separation problems. Mr. D. Malphurs further expanded use of this method to include simulated and BAYEX data and refined it to investigate the potential for isolating frequency and aspect bands that improve classification performance.

For target data exhibiting low SNR, Mr. R. Arrieta and Ms. I. Paustian also carried out studies to develop a non-image-based classifier requiring minimal training by exploiting target-unique elastic phenomena expressed in the data and seeking a representation of it where robust features can be extracted. For non-image feature extraction, acoustic color and time-frequency distribution (TFD) plots are viable candidates for displaying and understanding target scattering effects. In the past [1], both of these methods have been used to extract features for class separating data collected in NSWC PCD's pond facilities. However, when target signal-to-noise

is low so that oblique target aspects are difficult to see in acoustic color plots, acoustic-color-based class separation becomes more difficult. An example of an acoustic color plot exhibiting little usable structure at off-broadside aspects is shown in Fig. 5 for a steel cylinder buried in NSWC PCD's small-scale test bed. The cylinder is scaled so that the 200 kHz – 1.4 MHz band in the test bed encompasses several of the low frequency elastic modes seen in free-field both on and off broadside. For such cases, TFD representations may be preferred since they can be used to extract classifiable information at the aspects exhibiting the highest SNR. Because the TREX data collected in 2012 and data collected in NSWC PCD's pond under ONR funding for buried targets often exhibited low SNR in acoustic color plots, efforts focusing on using target data projections in time-frequency space were expanded to examine the distribution of energy contributed by elastic waves (material dependent) vs. diffracted waves (geometry dependent).

TFDs are amenable to physical interpretation of back-scattered chirps. For example, they can be used to isolate target differences such as hollow vs. solid because elastic waves excited on the surface of a shell and radiating back to a receiver come in at different instances in time than those excited on a solid. However, these two dimensional representations force trade-offs in resolution, computational efficiency, noise reduction, and cross-term generation [6]. Therefore, several time-frequency transforms were applied to modeled and available data to look for representations that best exhibit signal components associated with elastic radiation, especially resonances, which tend to have stable characteristics potentially useful for classification. It is well known that solid metallic cylinders support a variety of surface waves that can be excited acoustically and propagate on the surface of such cylinders. These waves are not confined to solid cylinders and may be detected on any axisymmetric object. Axisymmetric targets such as shells were studied initially because these typically exhibit strong sonar signals at broadside aspects, where simple models can be used to predict circumferential elastic effects. Time-frequency plots of modeled data at these aspects were used to look for and ascertain robustness of these effects in time-frequency plots of real target data.

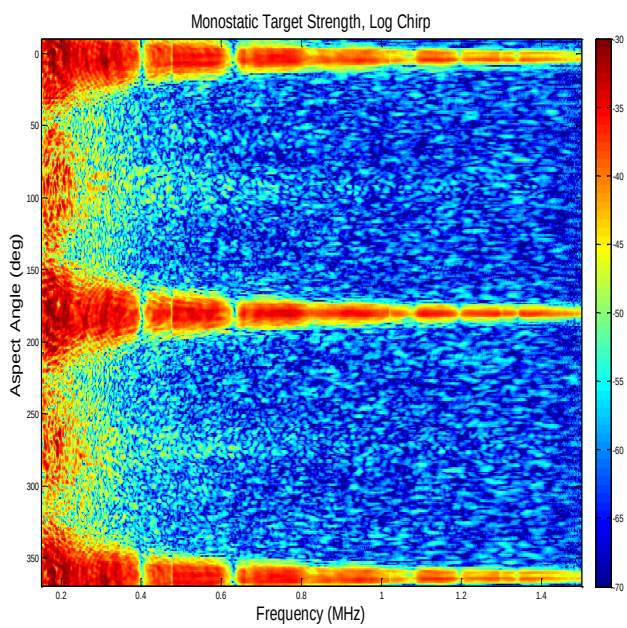

Figure 5. Acoustic color plot for backscatter by a buried solid steel cylinder in NSWC PCD's small-scale test bed facility.

Two wave types propagating on the surface of the object were of particular interest in the work reported here: pseudo-Rayleigh (PR) and Whispering Gallery (WG) waves [7]. By comparison, two other types, the Franz and Stonely waves are dependent on the geometry of the object (not on its composition) and propagate in the medium around the object. A third type, Guided Helical (GH) waves are launched at off-normal incident angles and are guided along the surface of the object along helical paths that are relatively long and have more opportunity to interact with the environment surrounding the object. The physics of PR and WG waves suggests, and experimental evidence collected at NSWC PCD corroborates, that they are less susceptible than the other types to changes in the external environment of the object and may be well-suited for classification of objects that are axisymmetric or nearly so. PR waves can propagate on flat as well as curved surfaces, whereas WG waves are expressed on curved surfaces and seem good candidates as indicators of axisymmetric objects. Since both of these types of waves also propagate on the inner and outer surfaces of thick shells, the approach taken was to develop computer algorithms that can differentiate these types of surface waves in low frequency sonar data projected onto spectral representations like TFDs and use them to classify objects as axisymmetric metallic vs. other. By refining this initial approach, it is conjectured that it will be possible to differentiate within the group of axisymmetric metallic objects and isolate thick shelled, thin shelled, and broken shelled objects; thus, providing additional clues that, fused with other image or non-image-based clues, enable unambiguous classification.

Results and Discussion

Accomplishments of project MM-2230 are described below according to the major tasks performed: field measurements and data analysis, Finite Element (FE) simulations/model development, and processing and ATR training tools.

Field measurements and data analysis:
Two TREX events in 2012-2013 and BAYEX in 2014 were carried out in collaboration with APL/UW in the Gulf of Mexico off Panama City, FL. In addition to supporting test logistics, NSWC PCD was aboard ONR's research vessel (R/V) Sharp to participate in the data collection from bottom targets as shown in Figs. 1 and 3. In 2012, Ms. I. Paustian, Mr. D. Malphurs, and Dr. J. Kennedy collected and processed data into imagery and acoustic color plots to assess whether the integration of sonar onto APL-UW's rail introduced any artifacts needing remediation; e.g., rail reverberation or cross-talk noise. Sample SAS imagery of a target line processed from the data is shown in Fig. 6, including a blow-up of the 500 lb bomb shape. Relative sizes of targets are discernible. In general, imagery is seen to display SNR and resolution comparable to data collected in NSWC PCD's pond. SAS processing appears to filter out most of the additional noise introduced by the environment into imagery.

Sample acoustic color plots of data collected on two pairs of the same UXO deployed proud are shown in Fig. 7. Unlike the imagery, the acoustic color plots appear noisier than versions processed from pond data. The same algorithms used to process pond data were applied here even though the Gulf environment is noisier. A significant source of reverberant noise was noted to be schools of fish within the measurement set-up. The noise level made stitching the

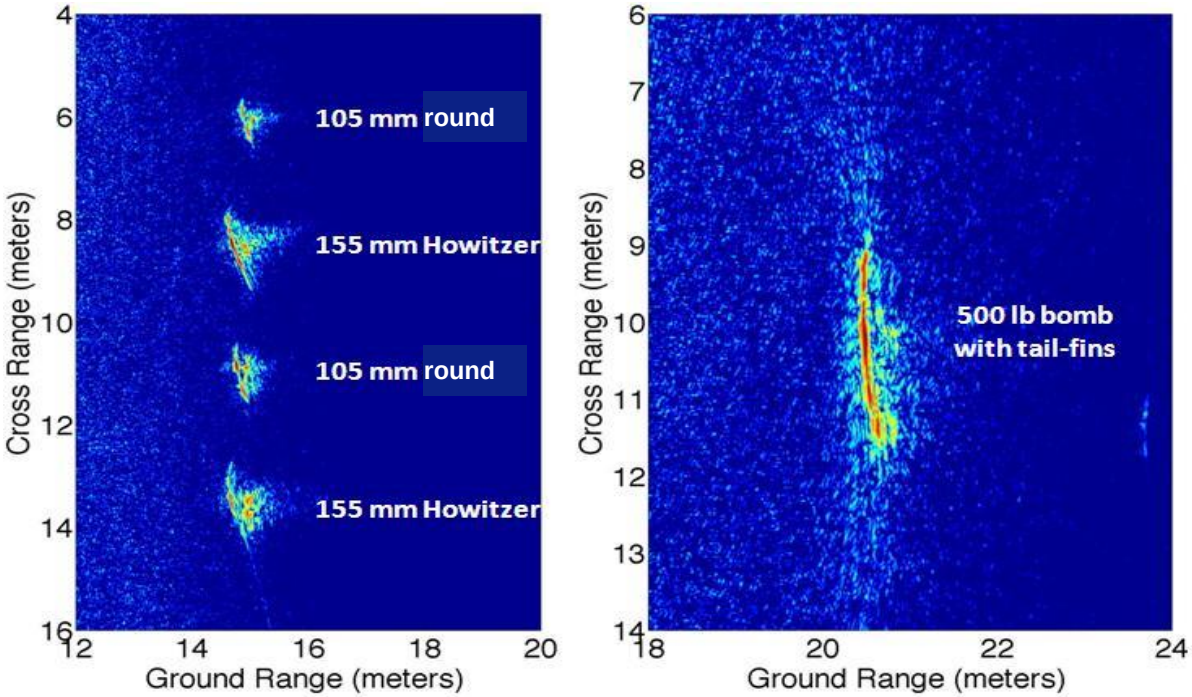

Figure 6. SAS imagery processed from TREX data collected in 2012.

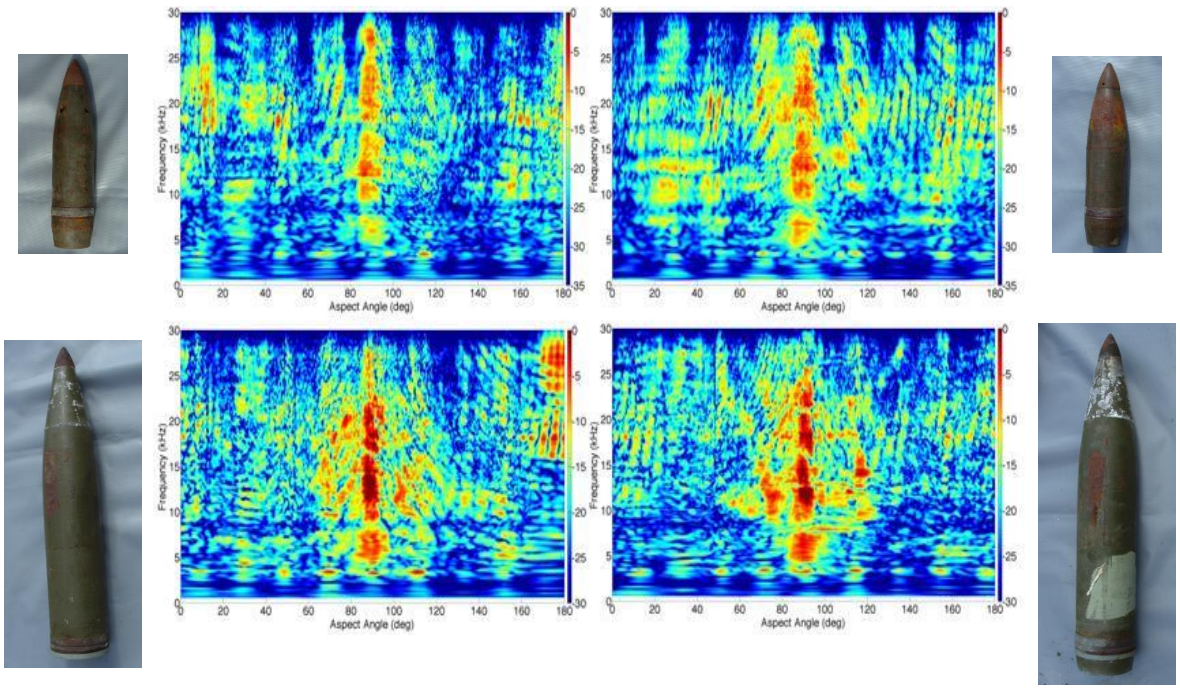

Figure 7. Target strength plots of the four targets located at a ground range of 15 m. Top and bottom rows refer to the 105 mm artillery round and 155 mm Howitzer shell, respectively. Left and right column are associated with the west and east target, respectively.

individually processed angular segments resulting from divers rotating each UXO at regular intervals more difficult. Some stitching artifacts are visible because the overlap regions, where adjacent angular intervals are averaged together, were harder to line up. These plots also show small differences in target strength between similar targets. These may reflect unknown structural differences between the same UXO or differences in the local environments of these UXO. Nevertheless, from an operational standpoint, the sonar integration appeared viable with no significant cross-talk issues or reverberation from rail structures that couldn't be resolved with careful set-up of the target field. The issues with reverberant noise from fish were felt to be resolvable by collecting multiple runs past the same targets so that noisy angular regions are eventually filled in with good data as fish schools move.

In 2013, the more elaborate target fields indicated in Fig. 3 and the target lists of Tables 1 and 2 were deployed. As in the previous year, NSWC PCD provided TREX logistics support and collaborated with APL-UW to collect data aboard the R/V Sharp. Again, this data was processed independently by NSWC PCD into imagery, acoustic color plots, and TFD plots for use in ATR analysis. However, a change in the processing scheme was necessitated by a hardware problem in the sonar during the measurement, which caused a distortion in the sonar beam that resulted in unexpected level variations in the data collected. While less important to processing of imagery, the variations had to be scaled out to obtain the target strength properly in acoustic color plots. To correct these variations, APL-UW made recordings of the transmit pulse at various angles and produced a correction algorithm that had to be added to the processing chain. The acoustic color plots generated at NSWC PCD were processed using APL-UW's correction software.

Figure 8 provides sample SAS imagery of the TREX field in set-up configurations where all targets are oriented with their long axes parallel to the rail. The SAS images in Figs. 8(a) and 8(b) correspond to data collected toward shorter (5 to 10 m target lines) and longer (15 to 40 m target lines) ranges using the fifth and first target field configuration, respectively. Blow-ups of a few of the longer range targets are also shown in Figs. 8(c-e). Backscatter returns from each of the targets are easily observed in both SAS images and relative sizes of detections are discernable. As in past measurements, the imagery is consistent with expectations for SNR and resolution for the available aperture provided by the rail for SAS processing.

An example of a "corrected" acoustic color plot obtained from the TREX data is shown in Fig. 9(a). This plot corresponds to data collected during the fifth target field configuration with a partially buried 105 mm artillery round, which is located at a ground range of 10 m and cross range of about 17 m in Fig. 8(a). The frequency range is from 5 to 30 kHz. A corresponding plot processed from data collected in NSWC PCD's pond that encompasses this band is shown in Fig. 9(b). For both measurements, the grazing angle in which the target is insonified is about 20°. Aspect angles of 0° and 360° correspond to an end-on orientation in which the target nose is pointed toward the acoustic source. An aspect angle of 180° corresponds to the target tail facing the acoustic source. Aspect angles of 90° and 270° are broadside orientations. The comparison shows the correction implemented by APL-UW is working reasonably well. The TREX plot is noticably noisier but this may be a consequence of the noisier Gulf environment. Also, some artifacts resulting from imperfectly stitching the angular aspect intervals set up by divers during TREX data collection is inevitable. The pond data had no stitching problems because it was collected with NSWC PCD's circular rail system [8].

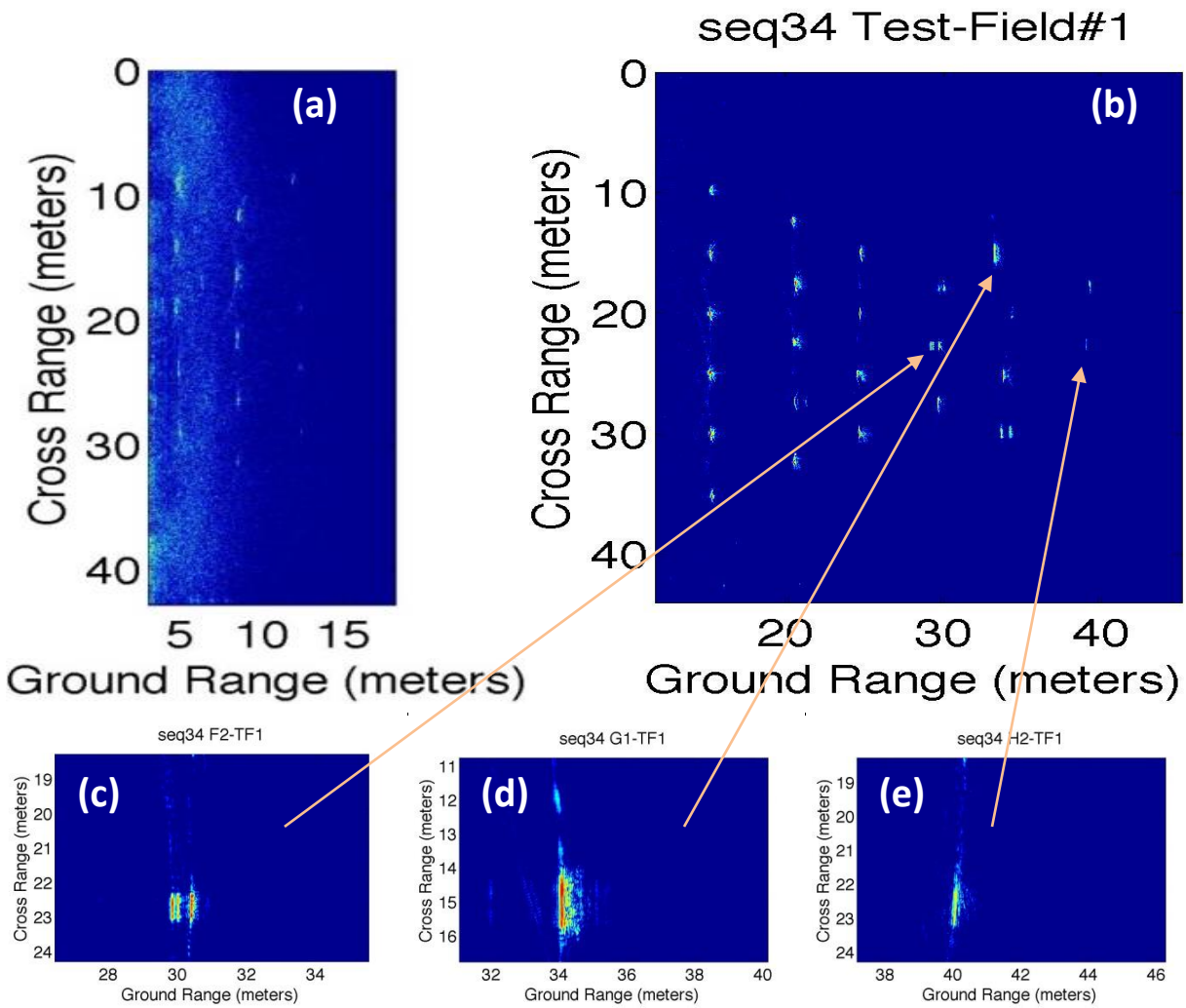

Figure 8. Sample SAS imagery of targets deployed at (a) shorter ranges and (b-e) longer ranges processed from the 2013 TREX.

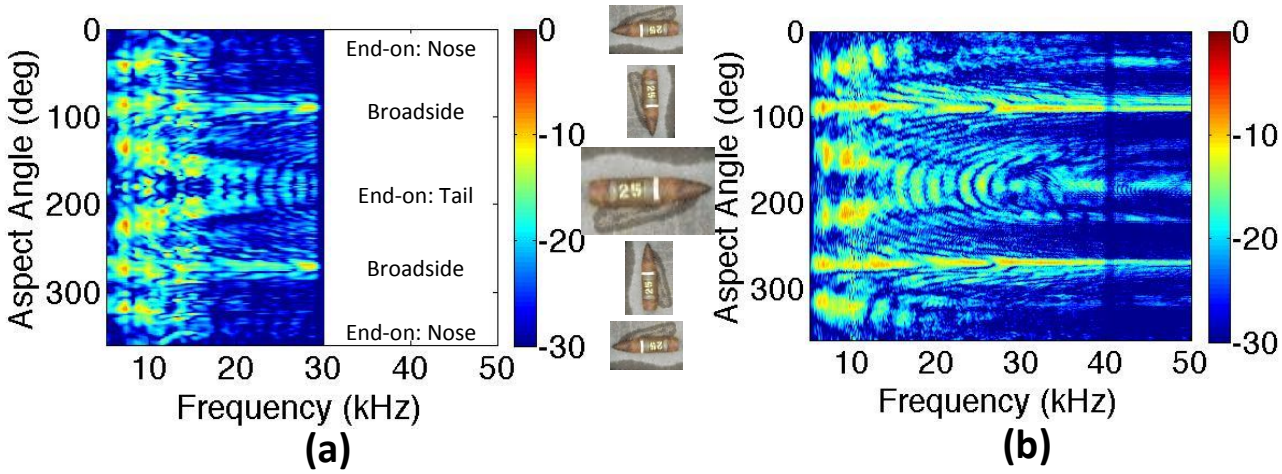

Figure 9. A comparison of acoustic color for a partially buried 105 mm artillery round UXO processed from (a) 2013 TREX data and (b) NSWC PCD pond data.

Several additional observations regarding these acoustic color plots are as follows. At the end-on configurations (0° and 360°) in which the nose is pointed toward the acoustic source, the backscatter levels are understandably very low. At broadside aspects (90° and 270°), high amplitude levels appear across most of the band. Drops in these levels occur when there is destructive interference between the specular return, returns reflected off the sediment, and elastic waves radiated back to the source. At the end-on aspect (180°) where the source is facing the tail, periodic enhancements appear at a 2 kHz interval. These are consistent with interference between the specular scattering from the tail and reradiation by a wave running along the surface of the 105 mm artillery round, reflecting off the nose and traveling back toward the tail end. At aspect angles around 140° and 220°, high-level signals are seen in these plots at an interval of a little greater than 2 kHz. These signals are caused by coupling to low order bending modes. These dynamics are consistent with the displacements observed in plots of the FEM-computed surface fields. This is shown in Fig. 10(a), where the proud 105 mm round is shown excited into a bending mode in the horizontal plane by an 8 kHz plane wave incident at 220° aspect on the round and 21.5^o grazing. A red circle is used to indicate where a blue point on the surface of the unstressed shape has been displaced through interaction with the incident field as observed from a vantage point directly over the UXO. The distances between displaced and undisplaced points are amplified by $8x10^8$ to make them visible. In Fig. 10(b), surface displacements associated with the wave mode excited along the length of the round by an 18.5 kHz plane wave incident at 180° aspect on the round and 21.5^o grazing are amplified and displayed. In this case, the wave mode appears to travel in a vertical plane so the displacements are shown in a side view facing the vertical x-z plane that contains the axis of the 105 mm round. While only the UXO surface displacements are plotted in Fig. 10, it is understood that inclusion of the water/sediment interface is rigorously accounted for in the computations and resides at the z=0 plane in Fig. 10(b).

The range dependence exhibited by targets in the aspect-frequency space is illustrated in Figure 11, which shows examples of acoustic color plots for the proud 100 mm Al UXO replica at 15 m

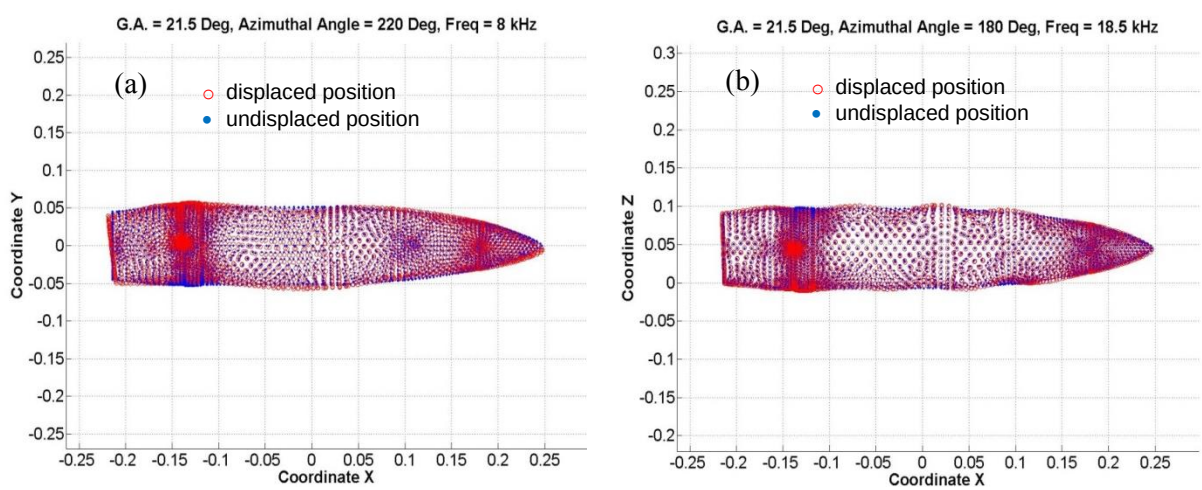

Figure 10. FEM-computed surface field displacements are displayed for the 105 mm artillery round deployed proud on a sand seafloor. In (a), an 8 kHz plane wave incident at 220° aspect and 21.5^o grazing excites the UXO into a horizontal bending mode. In (b), an 18.5 kHz plane wave at 180° aspect and 21.5^o grazing excites the UXO into a vertical wave mode along the length of the round.

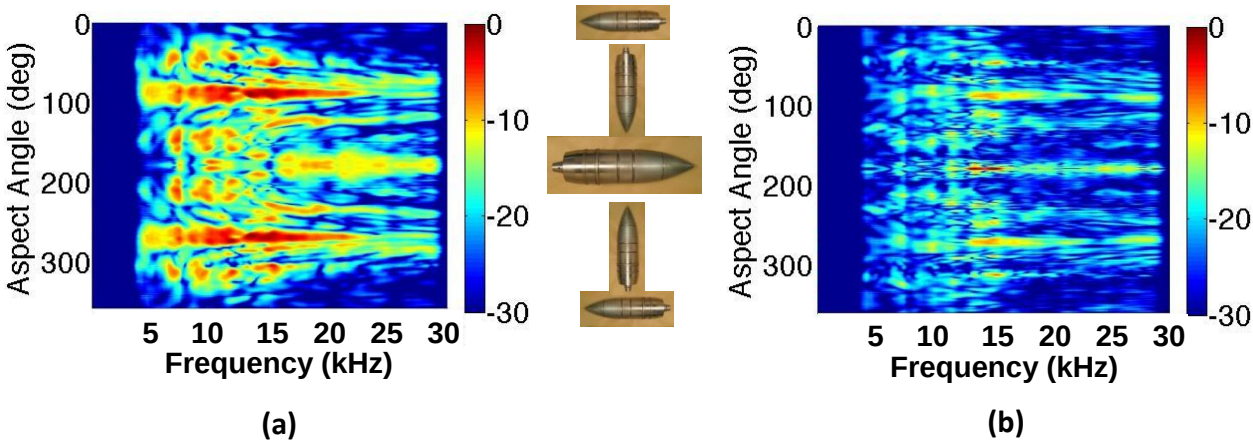

Figure 11. An illustration of the dependence of acoustic color on range for a proud 100 mm Al UXO replica deployed during TREX. The replica is at 15 m range in (a) and 40 m in range in (b).

and 40 m ranges. As in Fig. 9, 0° corresponds to the nose-on aspect. Although definite differences are seen as range increases, a gross underlying pattern appears preserved and, to aid in the search for classification features, it is worth gauging how well these patterns are preserved as conditions change for the same targets.

To gauge the level of similarity between targets at different ranges as well as between each other at the same range, we present in Fig. 12 a color-coded correlation matrix for 22 selected acoustic color plots processed for 6 proud UXO and 5 other proud shapes as listed in Table 4. The shapes considered are grouped so that the first 11 are UXO and the remaining 11 are other shapes. The (n,m) entry in the correlation matrix is computed as follows. A product matrix is generated from the acoustic color image matrices for targets indexed by n and m by converting the target strength amplitudes to a linear scale and then multiplying them together element by element. A raw correlation amplitude for plots n and m, $C_{raw}(n,m)$, is then computed as the sum of all the elements of the product matrix. This matrix of raw correlations is then scaled so that self-correlations (i.e., diagonal elements) are assigned the value 1 using the formula

$$C(n,m) = \frac{C_{raw}(n,m)}{\sqrt{C_{raw}(n,n)C_{raw}(m,m)}},$$

where $C(n,m)$ is the scaled matrix value presented in Fig. 12 according to the colorbar shown. The scaling allows a simple ranking of the level of agreement between plots on a scale of 0 to 1.

A few salient features are worth mentioning. First, the 11 UXO targets appear better correlated among themselves, as indicated by the color of the 11x11 upper left sub-block, than with most of the other targets. This includes the two plots in Fig. 11. The exception is the notched solid Al cylinder, which seems to exhibit some similarity to the UXO. Shape and size similarities among this group may explain some of this, which is preserved even as range changes. The 2 ft Al cylinder doesn't appear similar to any of the other targets. The panel target provided by Dan Brown appears similarly isolated, though to a lesser degree. While correlations between UXO and non-UXO are not perfectly isolated, these results would seem to bode well for using template matching as one feature in ATR discrimination.

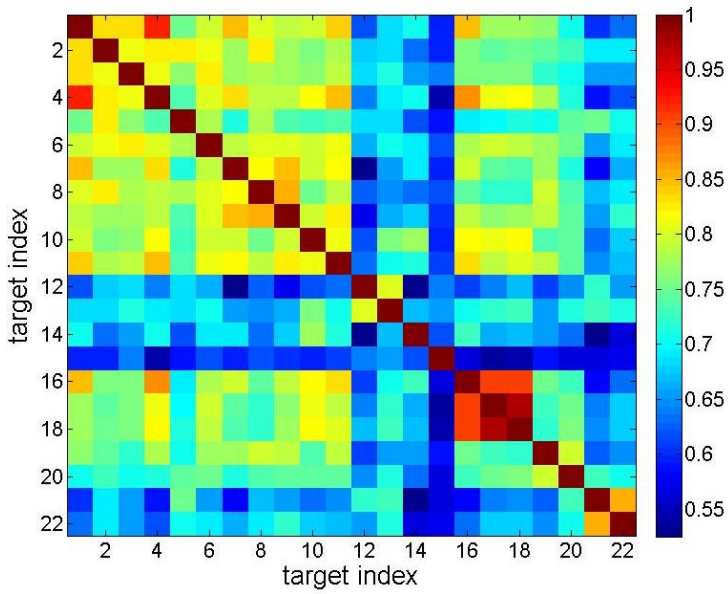

Figure 12. A matrix showing the cross-correlation magnitude between the acoustic color plots of TREX targets in Table 4.

Table 4. Legend for Fig. 12 Correlation Matrix

matrix/ target index	**TREX target**	**range (m)**
1	Al 100 mm UXO replica	15
2	Al 100 mm UXO replica	30
3	Al 100 mm UXO replica	40
4	Steel UXO replica	15
5	Orig. 100 mm UXO	30
6	Orig. 100 mm UXO	40
7	105 mm artillery round #1	15
8	105 mm artillery round #1	20
9	105 mm artillery round #1	25
10	155 mm Howitzer w/collar	25
11	105 mm artillery round #2	25
12	3 ft Al cylinder	30
13	3 ft Al cylinder	40
14	2 ft Al pipe	25
15	2 ft Al cylinder	20
16	Solid Al cylinder w/notch	15
17	Solid Al cylinder w/notch	20
18	Solid Al cylinder w/notch & modified processing window	20
19	Hollow Al cylinder w/notch	15
20	Hollow Al cylinder w/notch	20
21	Panel target – Dan Brown	20
22	Panel target – Dan Brown	25

From Table 4 it is noted that the plots compared for targets 17 and 18 were generated from the same target data and differ only by how the processing windows used in generating their respective acoustic color plots were chosen. This was included as a consistency check on the interpretation of the matrix. The acoustic color of targets 17 and 18 are visually similar and, as expected, both of these plots correlate best to each other and display very similar cross-correlations with the other shapes. These characteristics of similar plots when compared on a correlation matrix may also help to quantify when simulations are to be considered close matches to measured data.

In analogy to work done in 2013 for TREX, NSWC PCD carried out a logistics support/data collection and processing/data analysis effort in collaboration with APL-UW for BAYEX. As with TREX, a target set (Table 3) was deployed and data collected from aboard R/V Sharp. Data were then processed and analyzed independently by NSWC PCD into imagery, acoustic color plots, and TFD plots for use in ATR analysis. When projected onto the aspect-frequency space, BAYEX target signals exhibited differences as a function of range and environment. An example comparison is given in Fig. 13, which shows acoustic color plots for the proud 100 mm Al UXO replica at 10 m and 25 m ranges. Although these ranges are not directly comparable with Fig. 11, decay in SNR at the higher frequencies is also seen in the BAYEX plots compared to those for the same UXO at TREX. The reason for the lower SNR at the muddy site is thought to be due to burial of the UXO in the mud, which subjects the scattered UXO signals to attenuation and dispersion processes in the mud as well as additional reverberation effects between the top and bottom surfaces of the mud layer.

It is of interest to study whether the additional signal attenuation, dispersion and multi-path effects introduce enough variation to disrupt the pattern correlations in acoustic color space

useful for classification. In Fig. 14, a correlation matrix analogous to that in Fig. 12 is presented for a set of BAYEX target data listed in Table 5. The UXO are represented by targets 8-18. While correlations still appear stronger within the UXO group than between UXO and clutter, the preference does not appear as strong as with the TREX examples. To some degree, the extra variability due to uncontrolled burial in mud may explain the difference in correlations but the different target mix may also play a role. For example, the scuba tank (#3) was not considered in Fig. 12 but, here, appears to be better correlated with the UXO than much of the other clutter. The Al notched cylinder (#6) also maintains a significant correlation with the UXO in both TREX and BAYEX environments. An interesting exception to UXOs preferentially correlating higher within the UXO set is the Howitzer shell, especially the collared case (#10). The collared Howitzer shell is capped on the end to keep from free-flooding with water. This shell correlates

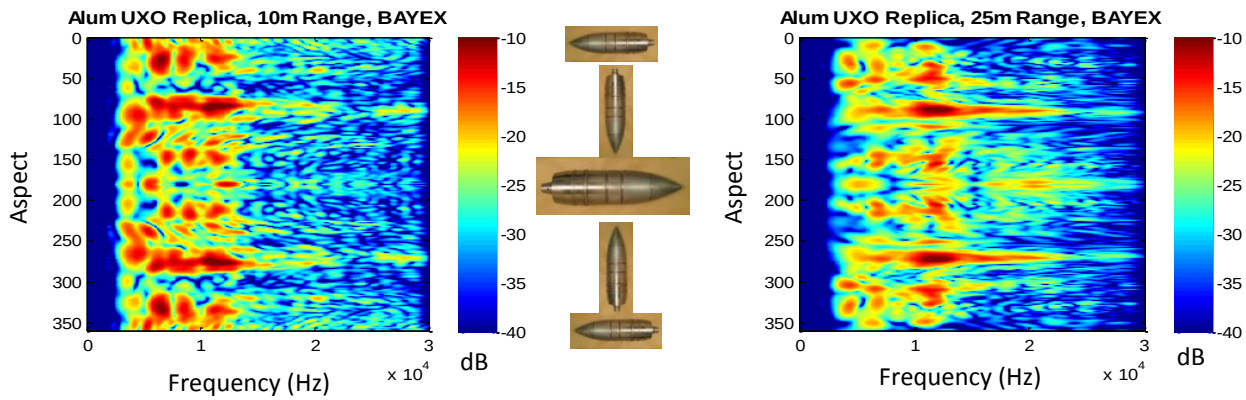

Figure 13. An illustration of the dependence of acoustic color on range for a proud 100 mm Al UXO replica deployed during BAYEX. The replica is at 10 m range in (a) and 25 m in range in (b).

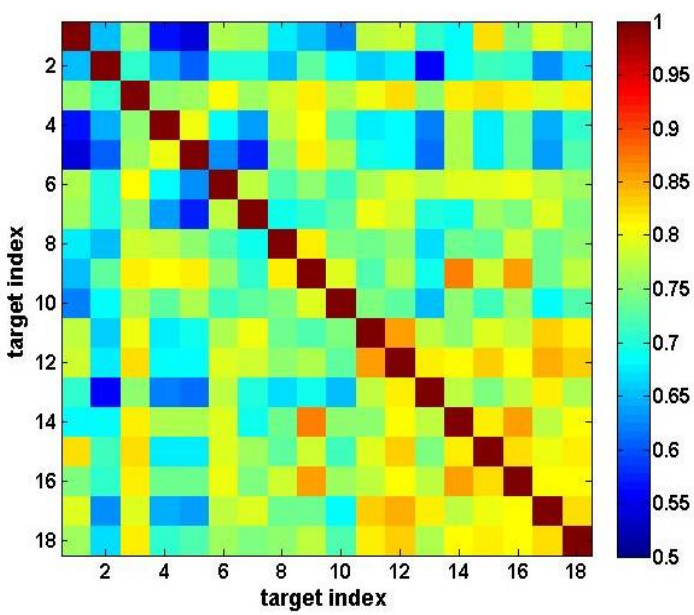

Figure 14. A matrix showing the cross-correlation magnitude between the acoustic color plots of BAYEX targets in Table 5.

Table 5. Legend for Fig. 14 Correlation Matrix

matrix/ target index	BAYEX target	range (m)
1	5:1 alum cylinder	20
2	55-gallon drum, water-filled	25
3	Scuba tank, water-filled, w/o stem	25
4	2 ft alum pipe	10
5	2 ft alum pipe	25
6	Solid alum cylinder w/ notch	10
7	Hollow alum cylinder w/notch	10
8	155 mm Howitzer w/o collar	10
9	155 mm Howitzer w/o collar	25
10	155 mm Howitzer w/ collar	10
11	152 mm TP-T	10
12	152 mm TP-T	25
13	Alum UXO replica	10
14	Steel UXO replica	10
15	Steel UXO replica	25
16	Alum UXO Replica	25
17	Bullet #1	25
18	Bullet #2	10

highest with the free-flooded Howitzer at 25 m rather than the one at the same range, which suggests the reason is more associated with a difference in the deployment environment than the range. It also doesn't appear to exhibit a significant preference for any other UXO. This departure from the usual trend may be a consequence of the greater complexity of this target, leading to a more complex acoustic color plot or one that is more sensitive to the environment.

FE simulations/model development:
FEM calculations based on the commercial COMSOL software package were carried out to build a database of simulated acoustic target and clutter responses. 3D FEM calculations were carried out by Dr. K. Lee on a variety of objects both in free field and deployed on a sandy bottom. Targets and clutter planned for deployment in the TREX and BAYEX measurements were emphasized in these calculations and a list of models completed so far is provided in Appendix A. For those UXO models for which good dimensional and material inputs were found (e.g., through cannibalization of extra copies), quite good agreement was found when comparing acoustic color plots of simulated and NSWC PCD pond data. Sample full 3D FEM calculations are shown in Fig. 15 for the 105 mm artillery round, in proud, partially buried, and 55° tilted configurations and insonified at a grazing angle of about 20°. The last is a configuration considered in pond measurements supported under a separate SERDP project (MR-2439) [9]. All plots span the 5 to 50 kHz frequency range and Fig. 15(b) was calculated to be directly compared with Fig. 9(b) as well as the TREX derived acoustic color plot shown in Fig. 9(a). Each of the acoustic color plots in Figs. 9 and 15(b) exhibit similar structure and amplitude, although the cleaner structure appearing in Fig. 15 is from maintaining a perfectly flat sediment surface model in the FEM calculation so there is no bottom roughness reverberation noise.

In any case, Fig. 15 demonstrates how sensitive acoustic color plots can be to the scattering configuration. Moderate burial with the UXO axis horizontal produces minor changes but tilting the axis can lead to significant changes that can, nevertheless, be rationalized based on geometric

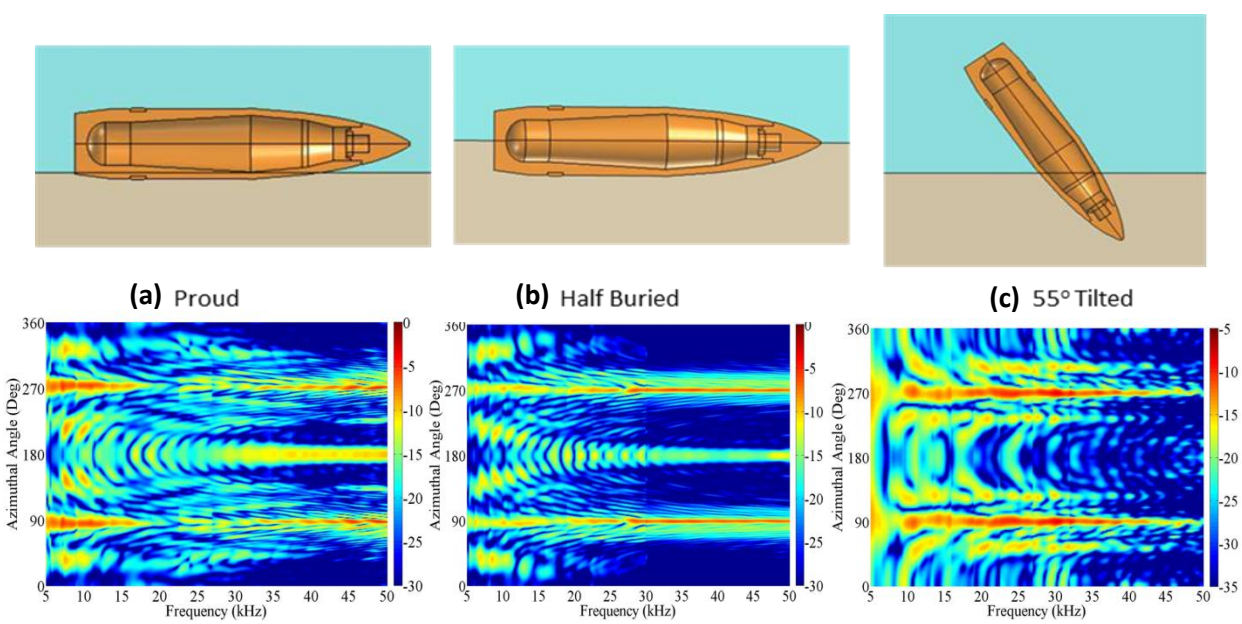

Figure 15. Acoustic color plots corresponding to full 3-D FE simulations of a partially buried 105 mm artillery round in (a) proud, (b) half-buried, and (c) 55° tilted configurations.

arguments. The tail-on aspect (180°) understandably weakens at high frequencies as that end turns away from the receiver. Also, the low-frequency flexural modes seen at frequencies less than 12 kHz and aspects as close to broadside as 45° in Fig. 15(a) would naturally be expected to shift closer to end-on to maintain the coupling angle with the incident field as the target tilt angle increases. That these modes are no longer evident in Fig. 15(c) is consistent with an incident field wave vector at a 20° grazing angle not being able to reach the coupling angle relative to the target for these modes because the target tilt angle (55°) is too high. Broadband enhancements on both sides of broadside appear as a consequence of new reverberant backscatter paths involving the target and the bottom [10].

The diversity seen in Fig. 15 shows ATR based on template matching with acoustic color plots can require an extensive sampling of configurations that may be obtained efficiently through simulation. Other runs that extend beyond the actual target configurations at TREX were also carried out to allow for effects of different interior fills, target clustering, mixed clutter, etc. to be represented in the database. Examples of these cases are shown in Fig. 16(a) for a group of UXO consisting of 2 Howitzer shells and a 105 mm artillery round and in Fig. 16(b) for a tire/cinder block combination.

Part of the process for populating our database of simulated acoustic responses is checking them against measured data when available to ensure sufficient accuracy. In these checks, it was found that simulated acoustic color plots for targets like the Howitzer shell or larger exhibited noisy structure not seen in pond measurements at frequencies beyond 30 kHz. Further checks revealed the origin of the discrepancies to be insufficient convergence of the FEM calculations, which could not be resolved by simply increasing the number of degrees of freedom in the problem due to memory resource limitations on NSWC PCD's FE dedicated rack computer system.

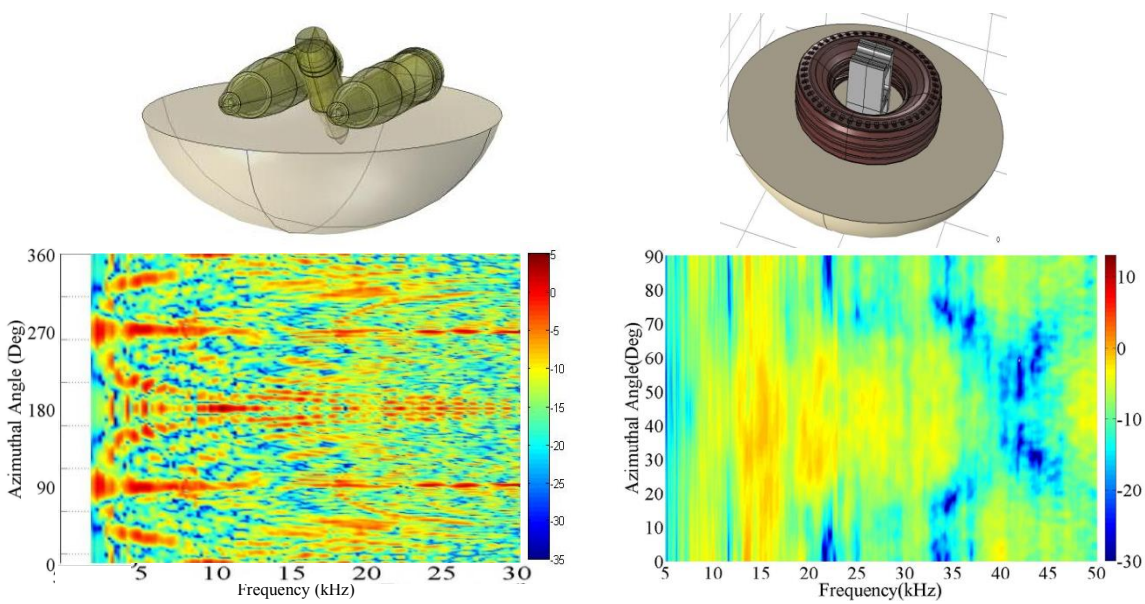

Figure 16. Sample calculations of acoustic color for more complex UXO and clutter configurations. On the left is a group of UXO consisting of a pair of proud horizontal 155 mm Howitzer shells with a tilted 105 mm artillery round embedded in the sediment between. On the right is a tire with a cinder block in the middle.

Therefore, an effort to further refine how the degrees of freedom are distributed in the FE volume was carried out by examining how the various parameters that control mesh density affect convergence. A process for optimizing convergence within available memory resources for larger targets was devised by carrying out reduced scale pre-processing runs on a personal computer to monitor trends in error growth as DOFs are varied among the fluid and target FE domains. From these trend curves, an optimal distribution of DOFs is determined over the desired frequency band along with a way to better estimate the highest frequency feasible for simulating a given 3D problem to a desired level of accuracy. Computations were simplified by splitting the frequency band into 10 sub-bands and generating an optimally accurate 3D FE model for all frequencies within each sub-band.

While the 3D FEM calculations performed with the refined criteria for setting FE DOFs appears to be producing reasonably converged results, agreement with pond data still remains unclear for a few targets for which accurate inputs are not all known. An example is the 155 mm Howitzer shell. Figure 17 (extracted from Ref. [9]) displays a drawing of the shell components found upon cannibalizing one of the available samples. Although interior dimensions are now known, the shell was found to be composed of five different materials, which are distinguished by color in the figure (green-steel, light gray-aluminum, red-copper, orange-ceramic, dark gray-plastic), some of which have material moduli that can vary over a significant range. Figure 18 provides a comparison of measured and modeled acoustic color for a proud Howitzer shell insonified at a grazing angle of about 20°. In Fig. 18(a), pond data processed and collected under separate SERDP funding [9] using NSWC PCD's circular rail is shown and the plots in Figs 18(b) and (c) are processed from simulations for two sets of parameters that differ only in the estimate for the moduli of the outer ceramic band colored orange in Fig. 17. The two simulated plots appear to have some differences in amplitude but fairly similar structure. However, this structure differs somewhat from that seen in the pond data plot around the end-on aspect facing the endcap (i.e., 180°). Drawing from the discussion of the correlation matrices in Figs. 12 and 14, the differences seen may not be significant enough to affect classification based on template matching if correlations remain high among measured and simulated plots for the same target relative to different ones. Nevertheless, classification based on other features extracted from elastically excited phenomena in these plots may still require better matches. Therefore, better ways to estimate relevant parameters will continue to be sought in future efforts.

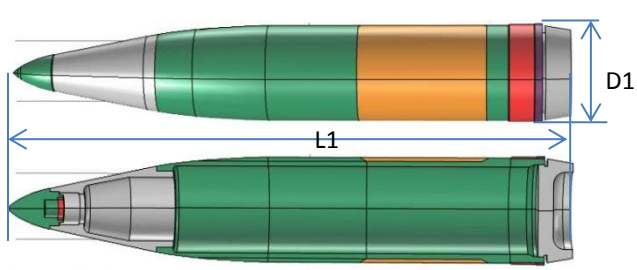

D1 = 0.155 m, L1 = 0.864 m

Figure 17. Schematic of the 155 mm Howitzer deployed in TREX, with different material components distinguished by color.

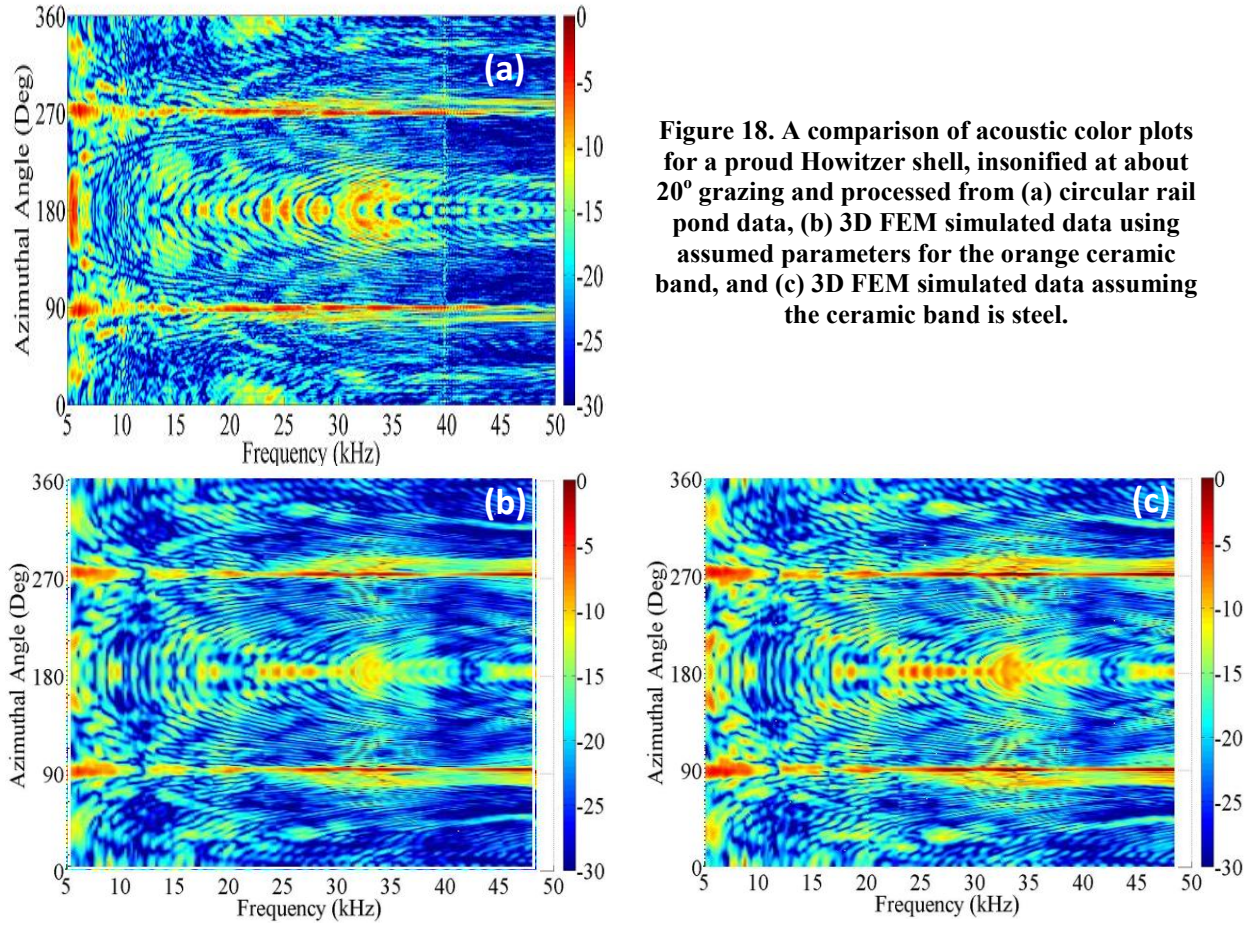

Figure 18. A comparison of acoustic color plots for a proud Howitzer shell, insonified at about 20° grazing and processed from (a) circular rail pond data, (b) 3D FEM simulated data using assumed parameters for the orange ceramic band, and (c) 3D FEM simulated data assuming the ceramic band is steel.

Even with accurate inputs, the target strength structure seen in Fig. 18 is clearly more complex compared to that for simpler UXO; e.g., as compared to Fig. 15 for the 105 mm artillery round. To help associate the structure seen at specific frequency and aspect angle locations with the dynamics excited on the target, a Matlab-based tool was written to read and animate surface field data from output files created by the FEM software used to solve for the scattered displacement fields. This tool was used to create the plots in Fig. 10 for interpreting highlights in backscatter by the 105 mm artillery round. Figure 19 shows the graphical user interface (GUI) created for the tool, displaying a single frame in the animation of the surface displacements on the Howitzer shell. Here, the shell is deployed proud on a sand sediment (water/sand boundary at z=0) and illuminated by a 7 kHz plane wave incident at 21.35^o grazing and 180° target aspect. Blue dots form a grid of undisplaced shell casing positions and red circles move in the animation to show how this grid is displaced as a function of time due to acoustic excitation. The GUI allows several parameters to be controlled in the animation, such as the frame rate, the number of aspects to animate displacements at, the number of cycles at each aspect to run through, the scale factor used to amplify displacements by, which plane to view the animations in, etc.

As seen in Fig. 19, an acoustic color plot can be displayed on the GUI and a black diamond is superposed on it to indicate the aspect and frequency point currently being animated. This enables visual association of highlights in the acoustic color plot with the dynamics being animated. However, it should be noted that significant dynamics can also be generated at

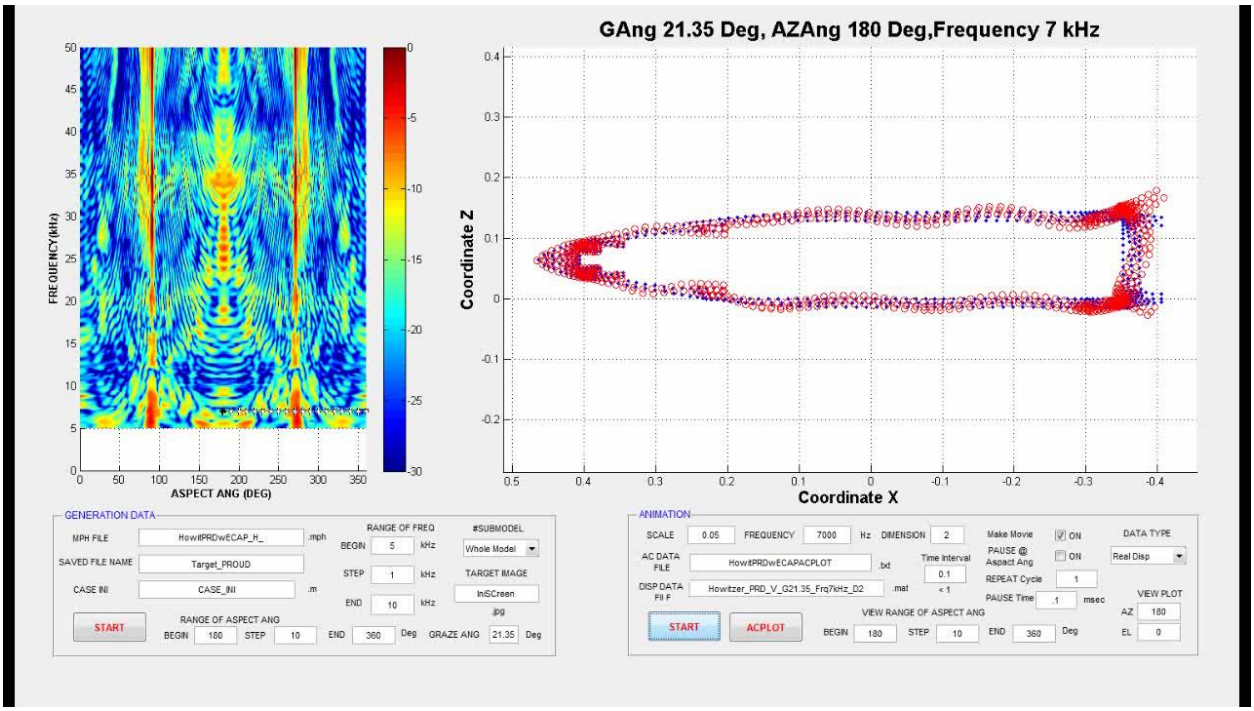

Figure 19. The GUI for the Matlab-based visualization tool created to read and animate surface displacement fields on targets simulated via NSWC PCD's 3D FEM software.

apparent nulls on the plot. This merely means the dynamics seen does not produce radiation in the backscatter direction. In our usage, acoustic color represents target strength in the backscatter direction only.

Although the 3D FEM modeling capability has been used to simulate target data for several targets deployed at TREX and BAYEX, these are still somewhat time-consuming to generate, requiring on the order of 2 days per acoustic color plot to cover the ~25 kHz band of the measurements. To make population of the database more efficient, Dr. G. Sammelmann developed an algorithm to generate data sets for ATR development by importing free-field 3D FEM or T-matrix data into PC SWAT and superposing it with just the dominant target-sediment interactions [2, 3] and simulated seafloor reverberation noise consistent with a power-law seafloor roughness spectrum given by [11]

$$W(\mathbf{k}) = \frac{w_2}{(kh)^{\gamma}},$$

where w_2, γ, and k are the spectral strength, exponent, and wave number, respectively, and h is a distance scale. This approach discards multiple scattering interactions with the seafloor and is useful when only variation caused by different bottom types is desired. However, data sets can be produced faster than previous import schemes. Examples of simulated acoustic color plots based on this method for the 100 mm Al UXO replica deployed proud at TREX are shown without seafloor reverberation noise in Fig. 20 and with simulated noise added in Fig. 21. In these results, sediment parameters associated with a muddy sand sediment were used: sound speed=(1620, -27.98) m/s, density=1.339 g/cm^3, w_2=.00207e-8 m^{-4}, γ=3.25, h=.01 m. The

imaginary part added to the sound speed corresponds to 0.58 dB/m/kHz sediment attenuation. For comparison, Figs. 20(a) and 21(a) truncated at 30 kHz correspond to the plot processed from TREX data in Fig. 11(b). Figure 20(c) and 21(c) truncated at 30 kHz correspond to the plot processed from TREX data in Fig. 11(a).

Each of these figures displays a trend that is immediately apparent. In Fig. 20, intensity depressions associated with interference between the direct target backscatter and the target-seafloor multipaths appear to sweep down in frequency as the grazing angle increases. In Fig. 21, reverberant noise contamination increases with grazing angle. Of course, the level of noise in acoustic color plots, whether processed from field data or simulated data, is a function of both the noise intensity added to the raw signal and the amount of filtering used in the processing to remove it. As signals grow noisier, it is typical to use tighter processing windows around signal components to remove noise, even if some target reradiation is sacrificed. The processing windows used to generate Fig. 21 were kept the same for all plots so that predicted trends in the noise levels can be seen in the plots. While Fig. 21 may not be optimally processed to recover the noise-free cases, the contaminated results show the importance of including realistic noise models in the simulations if trade-offs involving processing gain vs. detection configuration or ATR performance as a function of noise level are to be assessed.

Because target burial at BAYEX was difficult to control, deployment of targets in configurations that could be simulated with NSWC PCD's 3D FEM software was difficult. NSWC PCD's current 3D FEM models are generally configured for targets embedded in two-layered environments. A scattering configuration consisting of a sonar and target deployed in a water halfspace over several plane layers can also be accounted for by modifying the bottom reflection

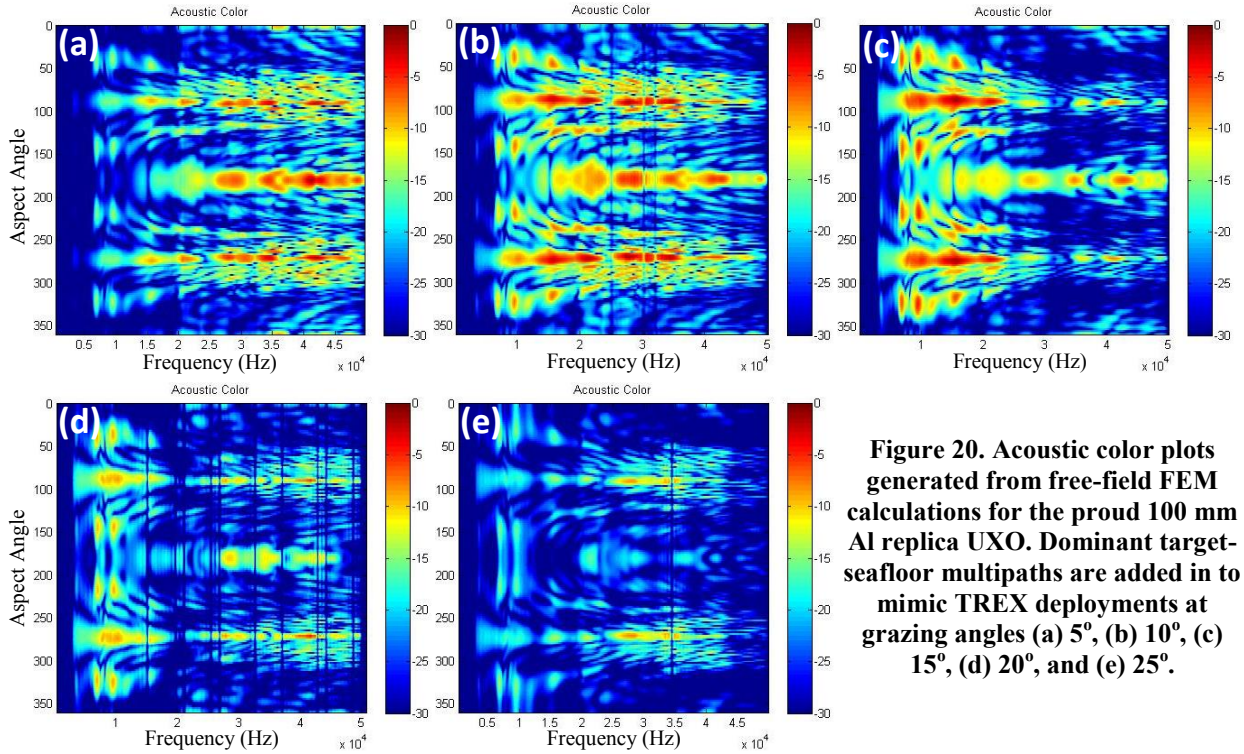

Figure 20. Acoustic color plots generated from free-field FEM calculations for the proud 100 mm Al replica UXO. Dominant target-seafloor multipaths are added in to mimic TREX deployments at grazing angles (a) 5°, (b) 10°, (c) 15°, (d) 20°, and (e) 25°.

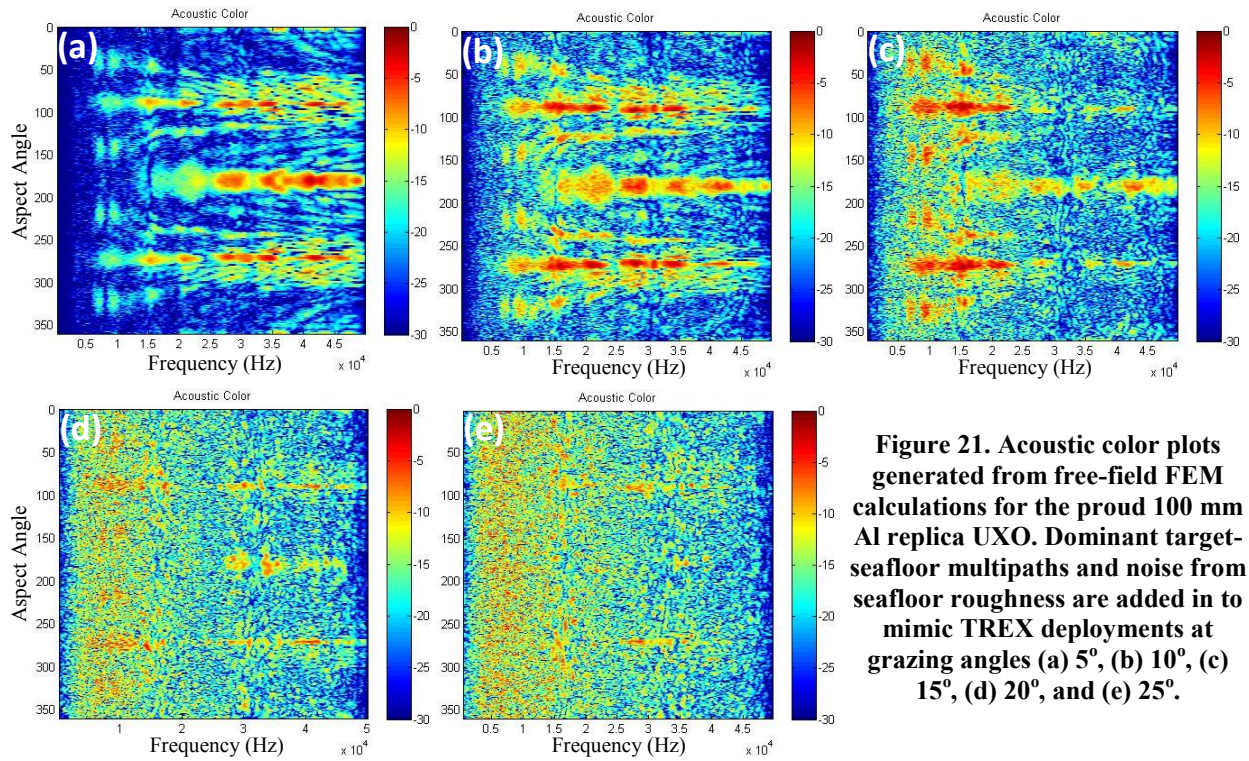

Figure 21. Acoustic color plots generated from free-field FEM calculations for the proud 100 mm Al replica UXO. Dominant target-seafloor multipaths and noise from seafloor roughness are added in to mimic TREX deployments at grazing angles (a) 5°, (b) 10°, (c) 15°, (d) 20°, and (e) 25°.

coefficient but targets embedded between environmental layers involve more complex modifications. Efforts to build and test a capability for 3D FEM modeling in such multi-layer environments is planned for future work but is not available yet. Therefore, for use in the ATR analyses discussed in this report, approximate target sonar responses in acoustic color space for the BAYEX environment were devised assuming a two-layer environment consisting of water over mud. Since diver observations at BAYEX showed targets tend to sink into mud to an uncertain height over the sand after deployment, targets are allowed to sink into the mud in the simulations. The sound speed and impedance chosen for mud are close to that of water: $c_{mud} = 0.984 c_{water}$, $\rho_{mud} c_{mud} = 1.24 \rho_{water} c_{water}$ as reported by Todd Hefner/APL-UW. An attenuation ratio ($Im(c_{mud})/Re(c_{mud})$) of 0.03 is also assumed for the mud properties. With these properties, PC SWAT was used to add environmental effects to imported complex FEM-generated free-field target strength data for both proud and buried deployments. Figure 22 presents sample PC SWAT generated acoustic color without seafloor noise for the 100 mm Al replica UXO in the water over mud environment. The acoustic color plots are simulated at 10 m range and both flush buried and proud deployments relative to the mud layer. Increasing target depth is seen to have the effect of attenuating some of the high frequency structure, which appears in the processed BAYEX plots. Comparing Fig. 22 with Fig. 13 suggests burial in the mud to be a common occurrence at BAYEX.

Fast, accurate simulations of acoustic target responses, even if for simpler UXO-like shapes, have been found to be very useful for carrying out the physical interpretation of phenomena needed in the search for ATR features associated with elastic target dynamics. Therefore, an effort was made to augment the fast simulation capability above, at least for simpler elongated shapes, by improving NSWC PCD's existing T-matrix algorithms so that faster and highly accurate free-field scattering responses could be calculated for targets larger than the 3D FEM

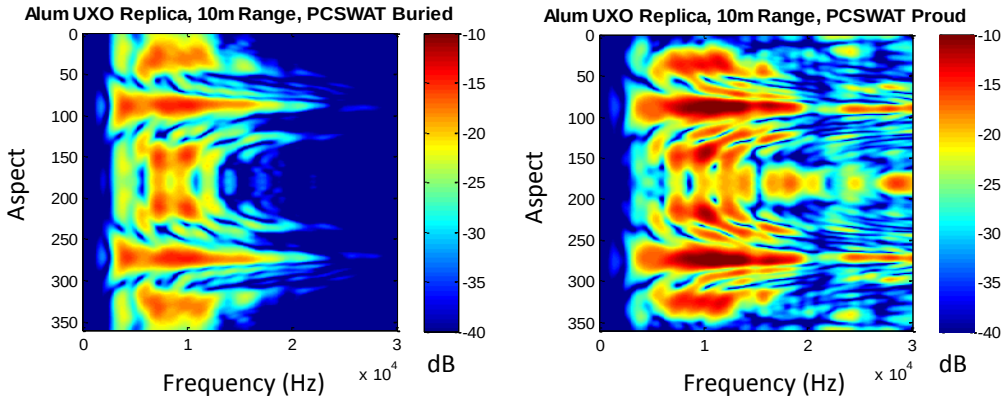

Figure 22. Acoustic color plots generated by PC SWAT from free-field FEM calculations to approximate environmental effects for a flush buried (left) and proud (right) 100 mm Al replica UXO deployed on mud at a range of 10m. Dominant target-seafloor multipaths are added in for the proud case to mimic BAYEX deployment on a mud halfspace.

technique currently handles due to memory limitations. NSWC PCD's current T-matrix capability for elongated shapes is based on a spheroidal-basis formulation [12, 13] that becomes unstable for objects at scaled frequencies kL/2>70 due to difficulties in calculating all the required spheroidal basis functions. To remove this limitation, a new spherical basis T-matrix algorithm adapted from ideas promoted recently by Waterman [4] and Doicu, et al. [5] was formulated and implemented. The new formulation stabilizes standard spherical basis T-matrix scattering solutions for highly aspherical shapes so that their scattering response can be computed by expansions in standard spherical eigenfunctions of the Helmholtz equation. Spherical functions, unlike spheroidal functions, are easy to compute to high orders even at high frequencies.

The new formulation is straightforward to implement and simply involves replacing a set of outgoing spherical basis functions in standard T-matrix formulations with a different spherical basis set consisting of only low order functions but distributed spatially along the symmetry axis of the shape considered. For example, a set of regular (hatted) and outgoing vector spherical functions truncated to a maximum order L takes the form

$$\begin{pmatrix} \widehat{\Psi}_{pml}(\mathbf{r}) \\ \Psi_{pml}(\mathbf{r}) \end{pmatrix} = \frac{1}{k}\nabla \begin{pmatrix} j_l(kr) \\ h_l(kr) \end{pmatrix} Y_{pml}(\theta,\phi),\ m = 0,\ldots,\mathrm{L},\ l\text{=m,…,L},\ p = \mathrm{e},\mathrm{o},$$

where $j_l(k\mathbf{r})$ and $h_l(k\mathbf{r})$ are spherical Bessel and Hankel functions of the first kind, $Y_{pml}(\theta,\phi)$ is a spherical harmonic, k is the medium wave vector, and $\mathbf{r}$ is a space point represented in spherical coordinates by (r, θ, ϕ). This can be substituted with the following spatially distributed set in field expansions

$$\begin{pmatrix} \widehat{\Psi}_{pmm}(\mathbf{r} - z_n\hat{\mathbf{z}}) \\ \Psi_{pmm}(\mathbf{r} - z_n\hat{\mathbf{z}}) \end{pmatrix},\ m = 0,\ldots,\mathrm{L},\ n = 1,\ldots,\mathrm{N},\ p = \mathrm{e},\mathrm{o},$$

where the points z_n are points chosen along the symmetry axis of an axisymmetric scatterer; in this case, oriented in the $\hat{\mathbf{z}}$ direction. Typically, the number N of these points used in expansions will be greater than L because the optimal distribution of these points along the axis to ensure good convergence is not known so more are used than necessary. The justification for using such a set of functions as an expansion basis is discussed in Ref. [5].

Standard spherical basis T-matrix formulations define T as the operator that project a vector of incident field expansion coefficients, α, to a vector of unknown scattered field expansion coefficients, **γ;** i.e., **γ≡Tα**, where these fields are expanded as

$$\boldsymbol{u}^{\mathrm{inc}}(\mathbf{r}) = \sum\nolimits_{pml} \alpha_{pml}(\mathbf{r}_{\mathrm{s}})\, \widehat{\Psi}_{pml}(\mathbf{r}),$$
$$\boldsymbol{u}^{\mathrm{sca}}(\mathbf{r}) = \sum_{pml} \gamma_{pml}\, \Psi_{pml}(\mathbf{r}).$$

The incident field expansion coefficients depend on the position of the source point, $\mathbf{r}_{\mathrm{s}}$, and, for a point source, are simply given by $\alpha_{pml}(\mathbf{r}_{\mathrm{s}}) = \mathrm{c}\Psi_{pml}(\mathbf{r}_{\mathrm{s}})$, where c is a scale constant.

To demonstrate the new T-matrix formulation, consider a typical formulation such as that proposed by Boström [14]. T is given as a product of matrices

$$\mathbf{T} = -\widehat{\mathbf{Q}}\mathbf{R}^{-1}\mathbf{P}(\mathbf{Q}\mathbf{R}^{-1}\mathbf{P})^{-1},$$

where the matrix elements are computed as the following integrals over the scatterer surface *S*:

$$\begin{pmatrix} \hat{Q}_{pml;\tau p'm'l'} \\ Q_{pml;\tau p'm'l'} \end{pmatrix} = \frac{k^3}{\rho\omega^2}\int_S \left[\widehat{\boldsymbol{n}}\cdot\widehat{\Phi}_{\tau p'm'l'}(\boldsymbol{r})\lambda\nabla\cdot\begin{pmatrix}\widehat{\Psi}_{pml}(\boldsymbol{r}) \\ \Psi_{pml}(\boldsymbol{r})\end{pmatrix} - \widehat{\boldsymbol{n}}\cdot\boldsymbol{t}_-\left(\widehat{\Phi}_{\tau p'm'l'}(\boldsymbol{r})\right)\lambda\widehat{\boldsymbol{n}}\cdot\begin{pmatrix}\widehat{\Psi}_{pml}(\boldsymbol{r}) \\ \Psi_{pml}(\boldsymbol{r})\end{pmatrix}\right] dA,$$

$$P_{\tau pml;p'm'l'} = \frac{\kappa_0^3}{\rho_0\omega^2}\int_S \widehat{\boldsymbol{n}}\cdot\widehat{\Psi}_{p'm'l'}(\boldsymbol{r})\,\widehat{\boldsymbol{n}}\cdot\boldsymbol{t}_-\left(\widehat{\Phi}_{\tau pml}(\boldsymbol{r})\right) dA,$$

$$R_{\tau pml;\tau' p'm'l'} = \frac{\kappa_0^3}{\rho_0\omega^2}\int_S \left[\widehat{\boldsymbol{n}}\times\widehat{\Phi}_{\tau' p'm'l'}(\boldsymbol{r})\cdot\boldsymbol{t}_-\left(\widehat{\Phi}_{\tau pml}(\boldsymbol{r})\right) - \widehat{\boldsymbol{n}}\cdot\boldsymbol{t}_-\left(\widehat{\Phi}_{\tau' p'm'l'}(\boldsymbol{r})\right)\widehat{\boldsymbol{n}}\cdot\widehat{\Phi}_{\tau pml}(\boldsymbol{r})\right] dA.$$

Here, λ is the fluid bulk modulus. The interior traction, $\mathbf{t}_-$, in these expressions is defined by

$$\mathbf{t}_-(\mathbf{u}(\mathbf{r})) = \lambda_0\widehat{\mathbf{n}}\nabla\cdot\mathbf{u}(\mathbf{r}) + 2\mu_0\widehat{\mathbf{n}}\cdot\nabla\mathbf{u}(\mathbf{r}) + \mu_0\widehat{\mathbf{n}}\times\nabla\times\mathbf{u}(\mathbf{r}),$$

with λ_0 and μ_0 being the elastic bulk and shear moduli of the interior medium. Longitudinal and transverse spherical vector basis functions, $\widehat{\Phi}_{\tau pml}(\mathbf{r})$, used to expand the elastic wave fields in the interior of the scatterer, are specified in the following form:

$$\widehat{\Phi}_{1pml}(\mathbf{r}) = \left(\frac{k_0}{\kappa_0}\right)^{3/2}\frac{1}{k_0}\nabla\{j_l(k_0r)Y_{pml}(\theta,\varphi)\},$$
$$\widehat{\Phi}_{2pml}(\mathbf{r}) = [l(l+1)]^{-1/2}\nabla\times\{\mathbf{r}j_l(k_0r)Y_{pml}(\theta,\varphi)\},$$
$$\widehat{\Phi}_{3pml}(\mathbf{r}) = \frac{1}{\kappa_0}\nabla\times\widehat{\Phi}_{2pml}(\mathbf{r}).$$

In these formulas, $\tau = 1$ specifies the longitudinal modes with wavenumber k_0 and $\tau = 2, 3$ are the transverse modes with wave number κ_0.

As pointed out by Waterman [4], instability arises in this formulation because the $Q_{pml;\tau p'm'l'}$ matrix elements cannot be integrated accurately at high frequencies if the surface of the scatterer approaches the origin such as when the shape is elongated or flattened. In such cases, the high *l*-order outgoing basis functions $\Psi_{pml}(\mathbf{r})$ grow very large. The approach implemented to stabilize these integrals is to replace these functions with low-order spatially distributed functions. This is done by postulating an invertible basis transformation to exist between these basis sets,

$$\Psi_{pmm}(\mathbf{r} - \mathrm{z_n}) = \sum_{l'} \sigma_{pmm;pml'}(-\mathrm{z_n})\Psi_{pml'}(\mathbf{r}).$$

Denoting the transformation as a nonsquare matrix $\sum$ with elements,

$$\Sigma_{pmn;pml'} = \sigma_{pmm;pml'}(-z_n),$$

and pseudo-inverse $\sum^{-1}$, a new T matrix can be formulated as

$$\boldsymbol{\gamma} \equiv \mathbf{T}\boldsymbol{\alpha} = \mathbf{T}\boldsymbol{\Sigma}^{-1}\boldsymbol{\Sigma}\,\boldsymbol{\alpha} = -\widehat{\mathbf{Q}}\mathbf{R}^{-1}\mathbf{P}(\mathbf{Q}\mathbf{R}^{-1}\mathbf{P})^{-1}\boldsymbol{\Sigma}^{-1}\boldsymbol{\Sigma}\,\boldsymbol{\alpha} = -\widehat{\mathbf{Q}}\mathbf{R}^{-1}\mathbf{P}(\boldsymbol{\Sigma}\mathbf{Q}\mathbf{R}^{-1}\mathbf{P})^{-1}\boldsymbol{\Sigma}\,\boldsymbol{\alpha}$$
$$\equiv \mathbf{T}^{\mathbf{d}}\,\boldsymbol{\Sigma}\,\boldsymbol{\alpha} = \mathbf{T}^{\mathbf{d}}\boldsymbol{\alpha}^{\mathbf{d}}.$$

Here, the matrix product $\boldsymbol{\Sigma}\mathbf{Q}$ merely results in a set of integrals with the normal outgoing functions replaced by low-order distributed functions and the transformed incident field vector $\boldsymbol{\alpha}^{\mathbf{d}}$ becomes a new vector consisting of low-order spatially distributed spherical functions, which are easy to calculate.

To demonstrate the improvement in stability afforded by using this modified version of the T matrix, the broadside backscatter form function for a 10:1 prolate Al spheroid in water is computed at 500 points over the scaled frequency range $0 < kL/2 < 100$ and presented in Fig. 23. Here, L is the spheroid length. The material parameters used for water were 1.0 kg/m^3 density, 1500 m/s sound speed and those for Al were 2.7 kg/m^3 density, 6350 m/s longitudinal wave speed, and 3050 m/s transverse wave speed. The computed spherical-basis result (red line) is plotted over a benchmark computed using the spheroidal-basis T-matrix (black line). Excellent agreement is seen up to kL/2=70 but the spheroidal benchmark is seen to degrade after kL/2=70 and diverge after kL/2=75, while the new spherical-basis computation just appears to accumulate some numerical noise for kL/2>70. If the source of the noise can be identified and removed, it is clear that the new scattering solution will have a more useful range. The noise is believed to be caused by a combination of ill-conditioning in solving matrix equations and insufficient accuracy in computing matrix elements due to integration of increasingly oscillatory integrands in some of these elements. Integration schemes more suitable for highly oscillatory integrands will be tried in future work. Further details of this T-matrix development has been documented in a paper entitled, "A more stable transition matrix for acoustic target scattering by elongated objects," by R. Lim. This paper has been accepted for publication in the Journal of the Acoustical Society of America and a preprint is attached in Appendix B.

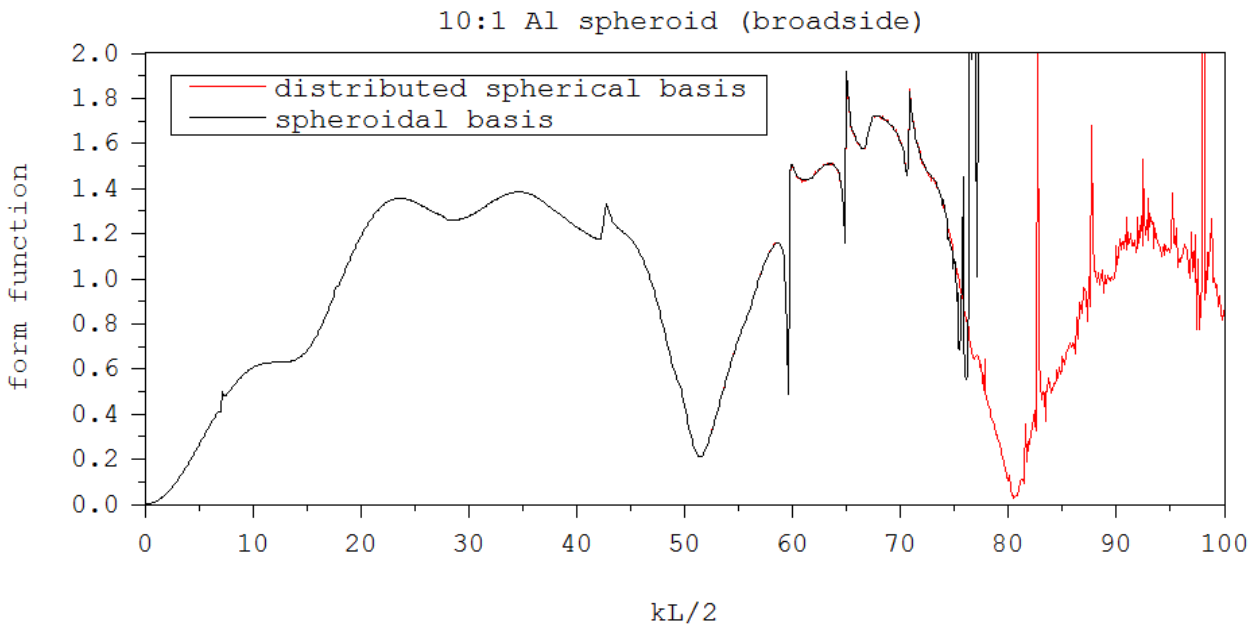

Figure 23. A comparison of the backscatter form-function of a 10:1 prolate Al spheroid computed with the new spherical-basis T matrix (red) and NSWC PCD's spheroidal-basis benchmark (black).

Classification analysis of shallow grazing angle data:
Much of the TREX and BAYEX data has been converted into acoustic color plots for analysis and, given the correlation results shown in Figs. 12 and 14 for the targets and clutter listed in Tables 4 and 5, an effort was made to explore the use of template matching for class separating the items in these tables by Dr. J. Prater and Mr. D. Malphurs. Although the items in Table 4 are all proud, targets are represented at different ranges and the importance of sampling over range has been an issue worth considering. To refine the template matching process for uncovering trends useful for classification, Dr. Prater carried out some simple studies with the TREX targets in Table 3. A few examples are described here. A set of acoustic color plots for 4 of the UXO deployed at TREX but processed from NSWC PCD circular rail pond data were chosen to act as a baseline that the TREX plots in Table 3 would be tested against. The pond data chosen corresponded to 8 plots for a proud and half-buried 100 mm Al replica, 100 mm steel replica, 105 mm artillery round, and 155 mm Howitzer shell. These were truncated to the same frequency band as the TREX plots, resampled by interpolation so that the same frequency and aspect points were represented in all plots, and shifted in aspect angle if necessary to make all axes consistent; e.g., to make sure the nose aspect is the same angle in all plots of the same target. A new correlation table was computed adding the 8 pond plots to the set in Table 3 with the exception that entry 18 was removed since it represented the same data set as entry 17. Altogether, 29 plots were cross-correlated.

Simple binary class separation problems were then posed, using the cross-correlation values between pond and TREX plots relative to a threshold to determine detections and the class that TREX detections belong to. Probabilities of correct detection (P_d) and false alarm (P_{fa}) were determined by counting the number of detections in the desired class that are correct and incorrect and dividing by the total possible correct and incorrect opportunities, respectively. These are monitored as a function of the detection threshold to create a ROC curve. The first

problem posed is whether all UXO in Table 3 (indices 1-11) can be effectively separated by correlating with the pond exemplars. The ROC curve determined for this problem is given in Fig. 24(a) and the corresponding dependence of P_d (blue line) and P_{fa} (red line) on the correlation threshold is given in Fig. 24(b). In computing these curves, if a UXO in the TREX set correlates above the threshold with one or more of the pond exemplars but the maximum correlation is not with the correct UXO type, it is still counted as a correctly classified detection.

Given the limited data set considered, the statistics is admittedly poor and this is reflected in the unsmooth curves. Each jump in Fig. 24(b) corresponds to another UXO (blue line) or non-UXO (red line) detected (lost) as the threshold is lowered (raised). Nevertheless, some suggestive points can be drawn. The ROC curve indicates relatively good performance by correlating with the pond data even though all pond exemplars were at a single range and the TREX targets were distributed over several ranges. From Fig. 24(b), one sees that the imperfect performance occurred when the correlation threshold dropped below 0.8, where three false alarms occurred before the last UXO was detected. The false alarms were: a TREX 2 ft Al pipe was confused with a pond 100 mm solid steel replica, a TREX solid Al cylinder with a notch was confused with a 100 mm solid steel replica, and a TREX hollow Al cylinder with a notch was confused with a pond 105 mm artillery round. The last TREX UXO detected was a 100 mm original UXO, which was matched with a pond 100 mm solid Al replica. Other than these cases, Fig. 24(b) shows the UXO and non-UXO do not overlap much in their correlations with the pond UXO.

A natural assumption is that the low overlap in UXO vs non-UXO correlations may be a consequence of the similar shapes among the UXO. If so, the correlation classifier would perform worse if it were used to separate particular UXO types. This is considered in Fig. 25, where the analogous curves in Fig. 24, are presented for the problem of separating the 105 m bullet shape from all other objects in Table 3. For this problem, TREX 105 mm artillery round correlations with pond 105 mm exemplars above a given threshold are considered missed detections if they are not the strongest correlation; i.e., if the TREX 105 mm round also has a higher correlation with the 100 mm Al replica it is called a 100 mm Al replica and counted as a missed detection. More false alarm opportunities and fewer correct classification opportunities (4

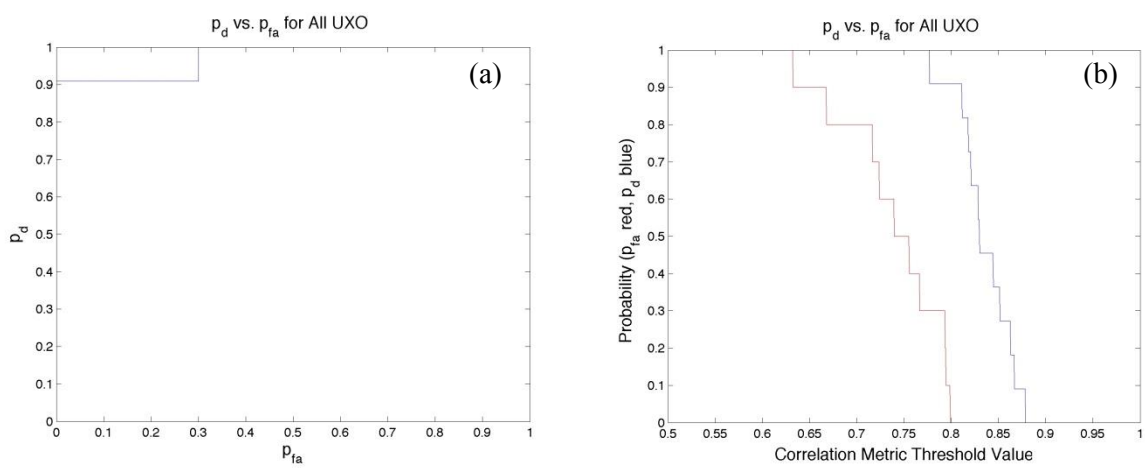

Figure 24. (a) ROC curve for class separating all UXO (entries 1-11) in Table 3. (b) Pd and Pfa curves used to generate ROC curve.

according to Table 3 and Fig. 25(b)) exist for this problem. Still, the performance degradation is not large. The narrow range of correlations for the 105 mm round seen in Fig. 25(b) suggests the plots share a lot of common structure, despite having collected the TREX 105 mm round data at 3 different ranges.

A final example is the problem of separating all 100 mm UXO shapes (entries 1-6) from all others in Table 3. The plots analogous to Fig, 24 for this problem are presented in Fig. 26. As in the previous case, TREX 100 mm UXO shape correlations with pond 100 mm exemplars above a given threshold are considered missed detections if they are not the strongest correlation; i.e., if the TREX 100 mm bullet also has a higher correlation with the 105 mm round, it is called a 105 mm round and counted as a missed detection. However, a TREX 100 mm Al replica can have its maximum correlation above the given threshold with a 100 mm solid steel replica or 100 mm original UXO and still be counted as a correctly classified detection. For this problem, the performance is not as good. Compared to the previous problem, the range of non-100 mm UXO shape correlations seen in Fig. 26(b) is not much different but the range of 100 mm UXO

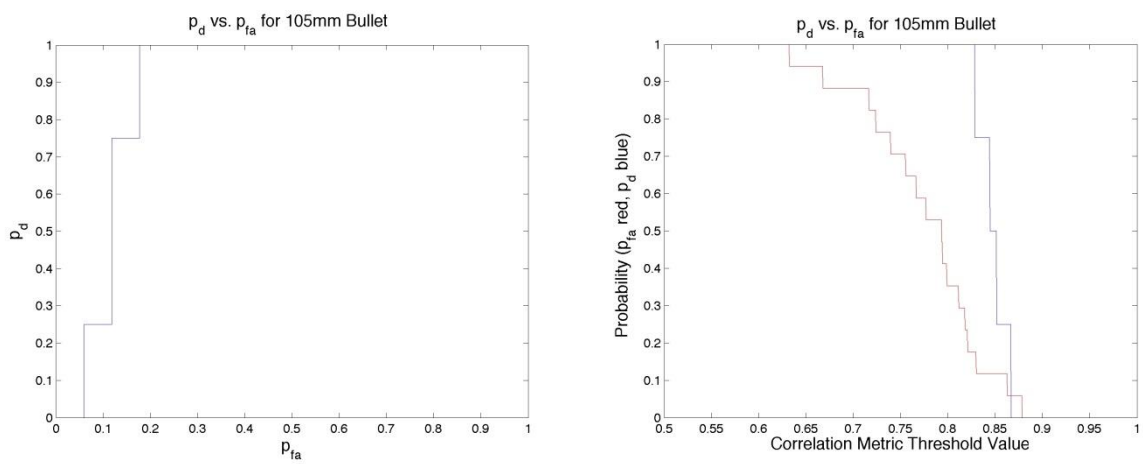

Figure 25. (a) ROC curve for class separating all 105 mm artillery round cases in Table 3. (b) Pd and Pfa curves used to generate ROC curve.

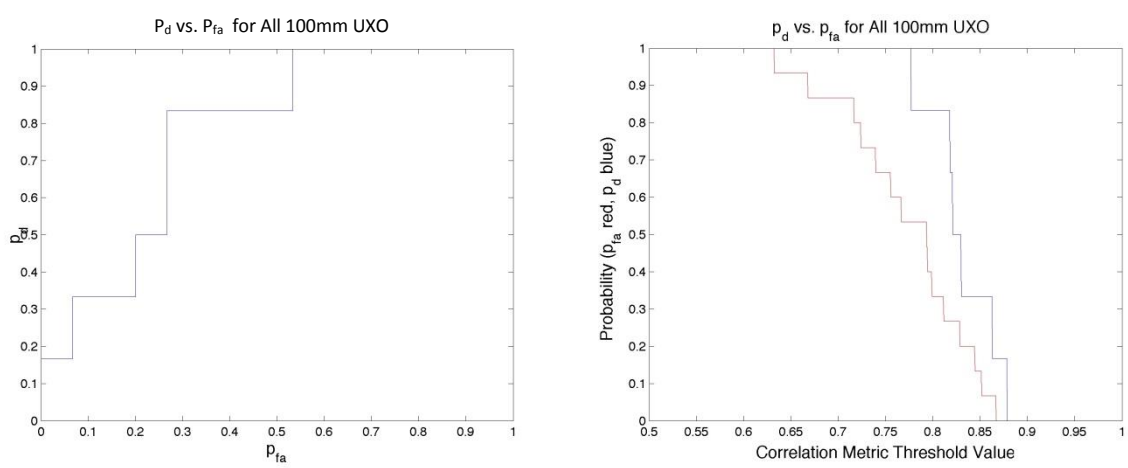

Figure 26. (a) ROC curve for class separating all 100 mm UXO shapes in Table 3. (b) Pd and Pfa curves used to generate ROC curve.

correlations is wider, resulting in more overlap between the two curves. In Fig. 26(b), the last 100 mm UXO shape detected as the threshold is lowered is a 100 mm original UXO, which correlated best with a pond 100 mm Al replica. Since the pond exemplars did not include acoustic color plots for the 100 mm original UXO, it is possible that better performance could have been achieved if they were.

The template matching analysis presented above suggests that range variations may not produce as significant an impact on classification as other factors but expectations will be refined in on-going work as data bases are augmented to improve the statistical significance of results. In the work reported here, the inclusion of BAYEX and simulated data helped in this regard and was also used to explore other issues. Among these, correlations to reveal frequency bands most useful for discrimination were considered to help focus sonar design as well as ATR feature choices. Also, template matches across the entire aspect range are not always possible since sonar data is more often collected over limited aspect angle intervals along linear tracks taken by the sonar platform. How discrimination potential degrades with matching over limited aspect angles was studied by template matching. Assessing use of simulated templates as baselines for testing was also of interest although the choice to use pond data above was motivated by the desire to avoid ambiguities caused by incorrect simulation inputs.

Mr. D. Malphurs continued the template matching analysis to investigate the issues above. BAYEX and simulated data were processed into acoustic color and included in an accessible database of plots. Several algorithms were then written to automatically access and parse the acoustic color data into selected frequency or aspect ranges so that trends in classification capability could be assessed relative to variations in these parameters. Target and clutter data selected from the BAYEX and TREX data sets for these studies were chosen in an attempt to mimic realistic situations while keeping the number of template correlation computations manageable. Each target and clutter object included had to have enough rail data collected on it to stitch a full 360 degree acoustic color plot. An effort was made to include both “difficult” clutter (i.e., similar in size and shape to the UXO) and more common clutter, such as the 55 gallon drum and rocks. Templates to serve as UXO exemplars were selected from both NSWC PCD pond data and FEM/PC SWAT simulations to ensure each UXO is fully represented under relevant environmental conditions. To optimize correlations against simulated data, no noise was included in the simulated acoustic color plots used as exemplars.

To illustrate trends seen in correlation studies so far, consider the list of target and clutter test data chosen to mimic detections in an area with mud and sand given in Table 6 and the list of UXO exemplar data correlated against to create ROC curves given in Table 7. The test data includes seventeen clutter items (Target #’s 1-17) and 15 UXO (Target #’s 18-32). The clutter items include a set of elongated, proud rocks simulated with FEM and PC SWAT to fill a desire for more natural clutter types that are comparable in size and shape to the UXO. Table 7 is populated with data from the two UXO types (100 mm and 105 mm artillery rounds) that have been validated the most in comparisons between controlled pond experiments and FEM simulations. Simulated data for these targets in a mud environment is included to augment the table of exemplars since a similar set of controlled pond data is not available for mud sediment. Because not all UXO in Table 6 or their deployment conditions are represented in Table 7, correlation-based template matching is not expected to produce ideal separation of the listed

Table 6. Targets and clutter with descriptions

Target #	Target Description	Range (m)	Environment	Burial State	Clutter/UXO
1	Rock	35	Mud	proud	clutter
2	5:1 Aluminum Cylinder	20	Mud	proud	clutter
3	Rock	10	mud (simulated)	proud	clutter
4	5:1 Aluminum Cylinder	25	mud	proud	clutter
5	3:1 Aluminum Cylinder	10	mud (simulated)	proud	clutter
6	3:1 Aluminum Cylinder	30	sand	proud	clutter
7	3:1 Aluminum Cylinder	40	sand	proud	clutter
8	PCSWAT Simulated Rock #1	10	mud (simulated)	proud	clutter
9	PCSWAT Simulated Rock #1	20	mud (simulated)	proud	clutter
10	PCSWAT Simulated Rock #1	30	mud (simulated)	proud	clutter
11	PCSWAT Simulated Rock #2	10	mud (simulated)	proud	clutter
12	PCSWAT Simulated Rock #2	20	mud (simulated)	proud	clutter
13	PCSWAT Simulated Rock #2	30	mud (simulated)	proud	clutter
14	Scuba tank, water-filled, w/o stem	25	mud	proud	clutter
15	2:1 Aluminum Pipe	10	mud	proud	clutter
16	2:1 Aluminum Pipe	25	mud	proud	clutter
17	2:1 Aluminum Pipe	25	sand	proud	clutter
18	155mm Howitzer w/o collar	10	mud	proud	UXO
19	155mm Howitzer w/o collar	25	mud	proud	UXO
20	152mm TP-T	10	mud	proud	UXO
21	152mm TP-T	25	mud	proud	UXO
22	100mm Aluminum UXO Replica	5	mud	buried	UXO
23	100mm Aluminum UXO Replica	10	mud	buried	UXO
24	100mm Aluminum UXO Replica	15	sand	proud	UXO
25	100mm Aluminum UXO Replica	20	mud	buried	UXO
26	100mm Aluminum UXO Replica	30	sand	proud	UXO
27	100mm Aluminum UXO Replica	40	sand	proud	UXO
28	100mm Aluminum UXO Replica	25	mud	buried	UXO
29	100mm Aluminum UXO Replica	30	mud	buried	UXO
30	100mm Steel UXO Replica	10	mud	buried	UXO
31	100mm Steel UXO Replica	25	mud	buried	UXO
32	105mm “Bullet” UXO	10	mud	buried	UXO

Table 7. Templates with descriptions

Template #	Target Description	Range (m)	Environment	Burial State	Clutter/UXO
1	100mm Aluminum UXO Replica	12	sand (NSWC PCD pond)	proud	UXO
2	100mm Aluminum UXO Replica	13	sand (NSWC PCD pond)	proud	UXO
3	100mm Steel UXO Replica	12	sand (NSWC PCD pond)	proud	UXO
4	100mm Steel UXO Replica	13	sand (NSWC PCD pond)	proud	UXO
5	105mm “Bullet” UXO	12	sand (NSWC PCD pond)	proud	UXO
6	105mm “Bullet” UXO	13	sand (NSWC PCD pond)	proud	UXO
7	100mm Aluminum UXO Replica	10	mud (simulated)	buried	UXO
8	100mm Aluminum UXO Replica	10	mud (simulated)	buried	UXO
9	100mm Aluminum UXO Replica	10	mud (simulated)	proud	UXO

10	100mm Aluminum UXO Replica	12	sand (NSWC PCD pond)	proud	UXO
11	100mm Aluminum UXO Replica	13	sand (NSWC PCD pond)	proud	UXO
12	100mm Steel UXO Replica	10	mud (simulated)	buried	UXO
13	100mm Steel UXO Replica	10	mud (simulated)	proud	UXO
14	105mm “Bullet” UXO	10	mud (simulated)	buried	UXO
15	105mm “Bullet” UXO	10	mud (simulated)	proud	UXO

items. However, the trends observed in template comparisons are expected to be of value in a relative sense. Thus, similarities revealed between UXO and the exemplars as a group may be relatively robust (i.e., insensitive to deployment differences) and lead to exploitable features.

The problem of separating the UXO in Table 6 from the clutter using acoustic color correlations with the templates in Table 7 is considered in Fig. 27. Three sets of ROC curves are presented to show the classification performance when correlating with (a) all templates listed in Table 7, (b) just the simulated templates, and (c) just the pond data templates. Within each of these sets, ROC curves show the classification performance when limiting the correlations to data in 6 specific low-pass frequency bands: 0-5 kHz, 0-10 kHz, 0-15 kHz, 0-20 kHz, 0-25 kHz, and 0-30 kHz. From these results, a few salient observations are made.

First correlating with all Table 7 templates appears to produce the best ROC curves but these are quite similar to the curves resulting from correlating with only the simulated templates. Therefore, more discriminating correlations are apparently obtained in matching with the simulated exemplars. Two factors may contribute to this result: 1) most of the UXO in Table 6 are in mud, as are the simulated templates in Table 7, and 2) the simulated templates are noise-free. Although further work will be needed to verify the environmental connection, the apparent degradation from correlating with the pond data templates is believed to be primarily due to the environmental difference.

Second, it is noted that the apparent effectiveness of classification based on correlating with simulated templates supports the utility of simulation as a tool for supplementing existing databases. Of course, this assumes accurate material and dimensional inputs for the simulations.

A last observation is that the entire frequency band is not necessary to obtain the best classification performance, at least, when using correlations in acoustic color space as a feature. Depending on how classification criteria are set, data can be collected over narrower bands with the same or better performance. For example, per Fig. 27(a), if one requires all UXO correctly classified with fewest false alarms, data collected over the 0-10 kHz band (red curve) is just as effective as the entire band; i.e., the red curve and cyan curve reach P_d=1 at the same lowest value of P_{fa}. This is not surprising as inspection of plots such as Figs. 9, 11, 13, and 22 show this band contains a significant level of elastic activity like that illustrated in Fig. 10 at off-broadside aspects. It is believed that this elastic activity can be discriminatory for UXO with elongated shapes. This is also consistent with the poor performance associated with the 0-5 kHz band (blue ROC curve) since the acoustic color plots from TREX and BAYEX data typically show little target strength in most of this band.

Further insight can be gained from inspecting ROC curves over different frequency band configurations. In Fig. 28, ROC curves analogous to those in Fig. 27 are shown except the

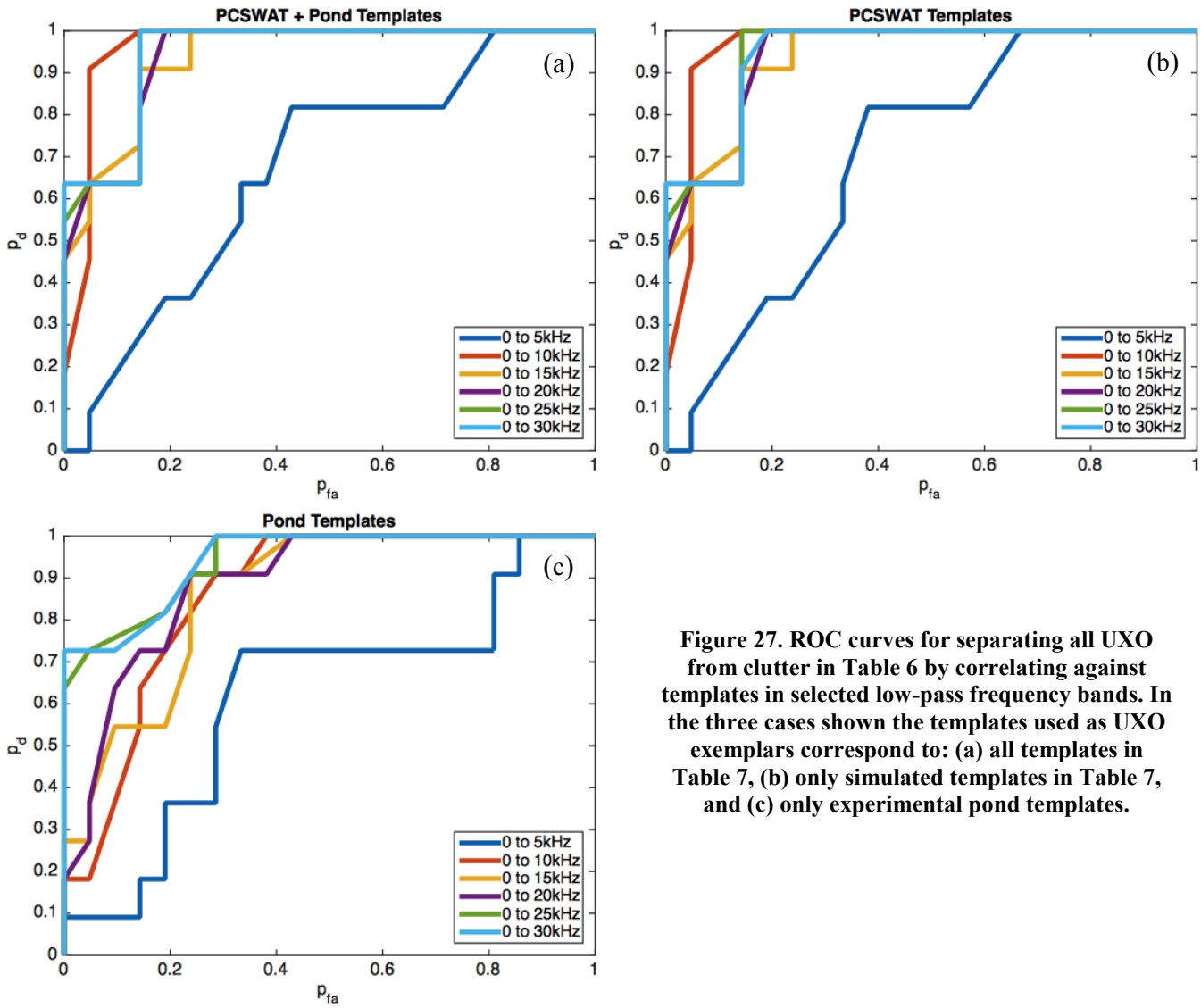

Figure 27. ROC curves for separating all UXO from clutter in Table 6 by correlating against templates in selected low-pass frequency bands. In the three cases shown the templates used as UXO exemplars correspond to: (a) all templates in Table 7, (b) only simulated templates in Table 7, and (c) only experimental pond templates.

template correlations are computed in 6 consecutive non-overlapping bands, 5 kHz wide: 0-5 kHz, 5-10 kHz, 10-15 kHz, 15-20 kHz, 20-25 kHz, and 25-30 kHz. Overall, UXO classification is poorer in these bands compared to the previous results but this could be expected since less information is available to increase the gap in correlations aiding classification. This also produces some unexpected differences. Given the strong 1-10 kHz curve and the weak 0-5 kHz curve in Fig. 27(a), the 5-10 kHz curve in Fig. 28(a) might be expected to be similar to the 1-10 kHz ROC curve but a notable difference is seen. However, a band displaying little classification potential on its own can have a significant effect when added to bands that perform better. For example, this can happen if the added band happens to increase correlations of those UXO that match the UXO exemplars the least and/or decreases the correlations of those clutter items that match the UXO exemplars the best. Referring back to P_d and P_{fa} curves like that in Fig. 24(b), such correlation changes modify the shapes of the curves to reduce the overlapping region; thus, improving the ROC curves.

Unlike the ROC curves in Figs. 27(a) and 27(b), those in Figs. 28(a) and 28(b) are not as similar.

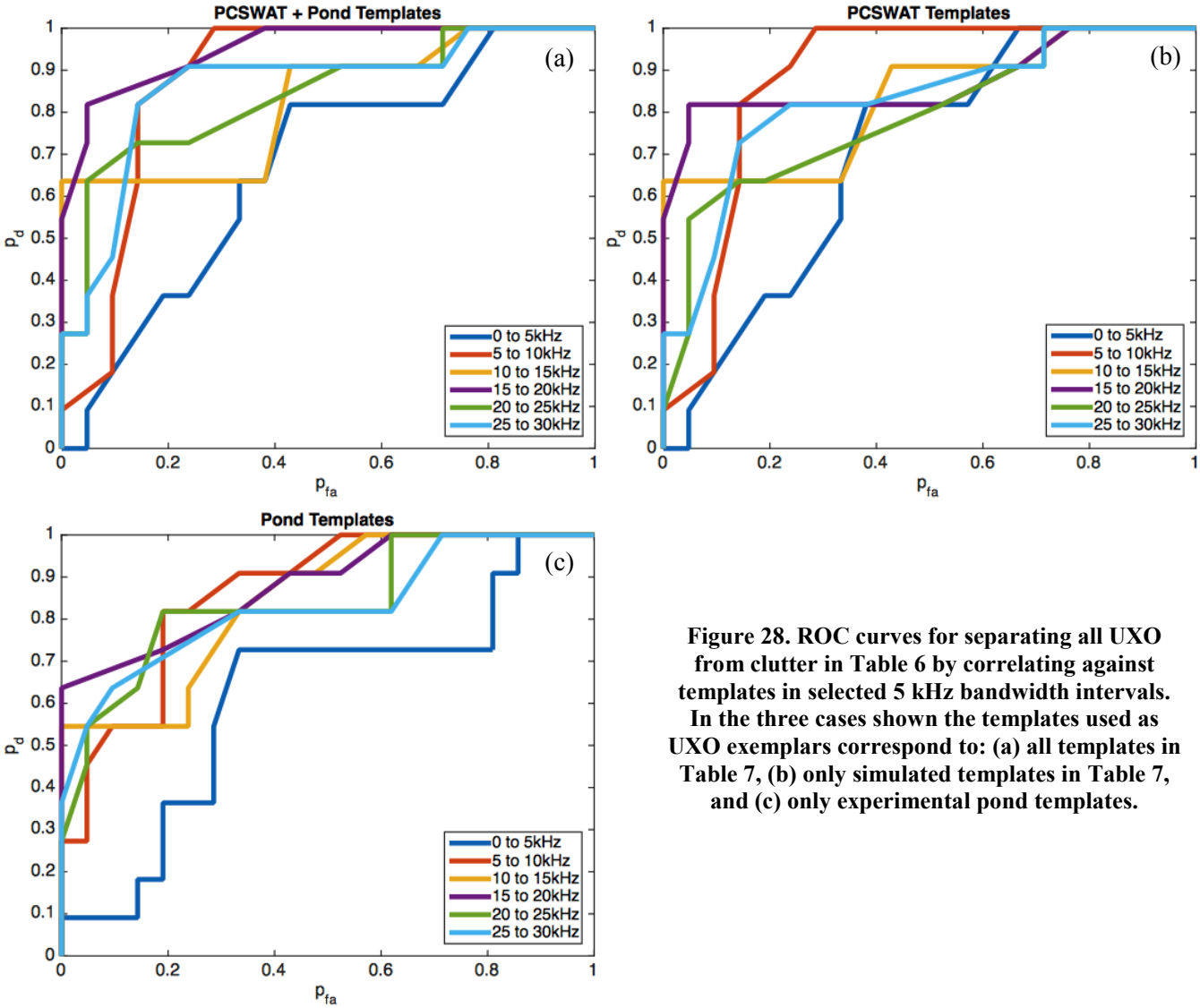

Figure 28. ROC curves for separating all UXO from clutter in Table 6 by correlating against templates in selected 5 kHz bandwidth intervals. In the three cases shown the templates used as UXO exemplars correspond to: (a) all templates in Table 7, (b) only simulated templates in Table 7, and (c) only experimental pond templates.

Only the 5-10 kHz ROC curve appears the same between these two sets. In this band, the UXO color data correlate higher with the simulated templates than the pond templates listed in Table 7. As noted with Fig. 27, this is consistent with an environmental effect. However, irrespective of whether simulated templates, pond templates, or both of these are used as the exemplars correlated with, in each case this band yields the lowest P_{fa} allowing P_d=1 so that all UXO are correctly classified with fewest false alarms. The higher bands exhibit less preference and produce ROC curves that span a greater range of performance than seen in Fig. 27. This suggests the lower frequency 5-10 kHz band is particularly important for classification since it is common in all the bands represented in Fig. 27(a) except 0-5 kHz and classification performance appears more consistent compared to Fig. 28(a).

Also revealed from Fig. 28(a) is the ROC curve associated with the 15-20 kHz band, which shows performance better than the 5-10 kHz band provided some false alarms are accepted. This curve utilizes exemplars from both simulated and pond data to achieve the best performance.

Further tests of the robustness of this band and work to understand the phenomena contributing to it are needed to help identify potential classification features from them.

The final frequency band configuration considered for separating the UXO in Table 6 is shown in Fig. 29, where ROC curves analogous to those in Fig. 27 are shown except these curves correspond to limiting the correlations to data in 6 specific high-pass frequency bands: 25-30 kHz, 20-30 kHz, 15-30 kHz, 10-30 kHz, 5-30 kHz, and 0-30 kHz. The lowest P_{fa} allowing P_d=1 is seen with the complete band and the band with the next lowest P_{fa} excludes only the 0-5 kHz band. This is consistent with expectations since the wider bands should allow better matches between like objects and help distinguish unlike ones. This bandwidth vs performance trend is generally followed within all three sets of curves (a)-(c), where the performance criterion is set for the fewest false alarms with all UXO correctly classified. However, in this case, it is notable how the range of P_{fa} over which each set of curves reaches P_d=1 varies in comparing Fig. 27 to the corresponding plots of Fig. 29. With the exception of the 0-5 kHz curve, the low-pass ROC curves in Fig. 27 reach P_d=1 over a narrower P_{fa} range. (As noted earlier, the 0-5 kHz curve is

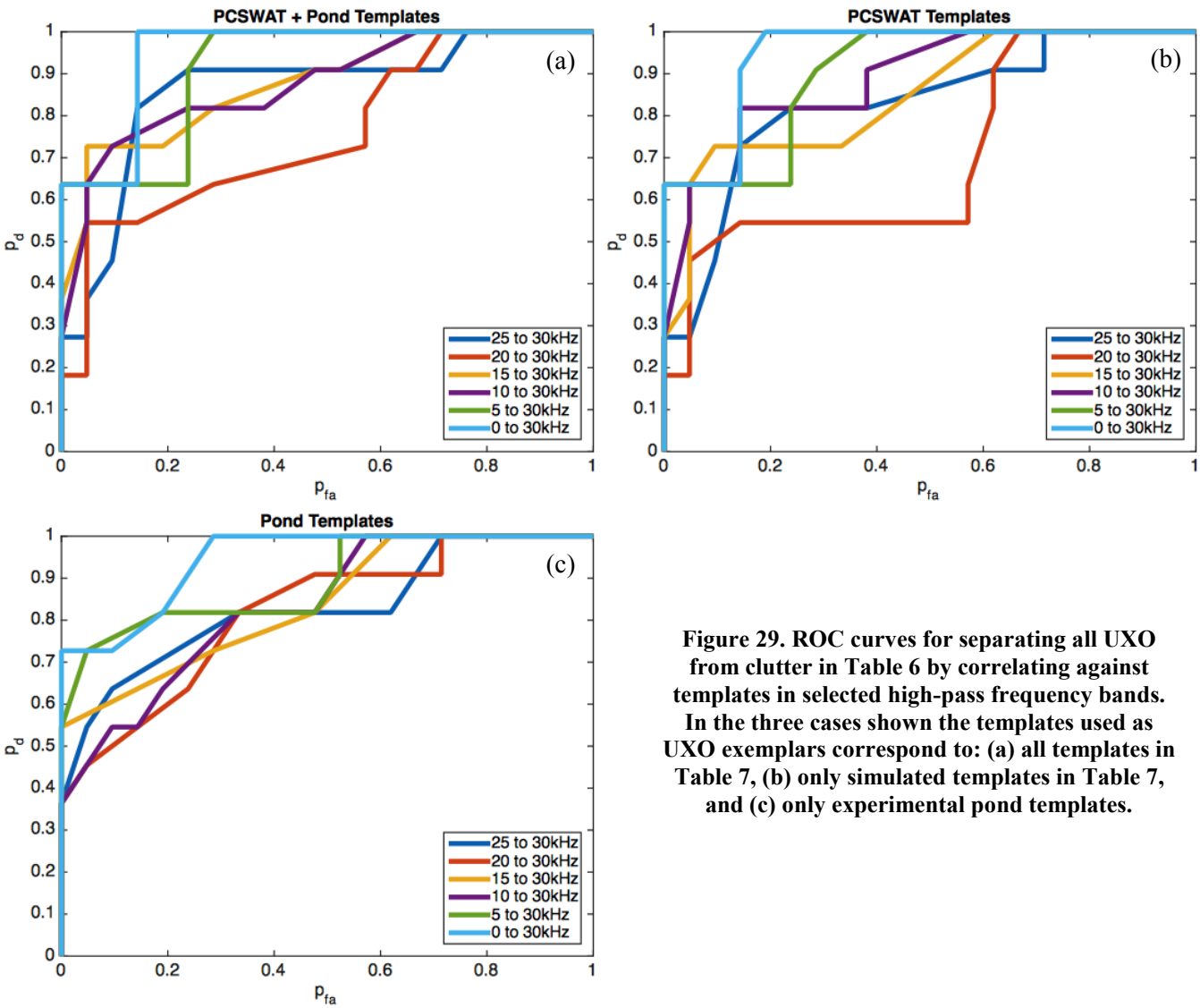

Figure 29. ROC curves for separating all UXO from clutter in Table 6 by correlating against templates in selected high-pass frequency bands. In the three cases shown the templates used as UXO exemplars correspond to: (a) all templates in Table 7, (b) only simulated templates in Table 7, and (c) only experimental pond templates.

exceptional because data collection over this band was limited.) In line with previous reasoning, this is consistent with the lower frequencies passed in each low-pass band playing a dominant role in setting classification performance based on the template matching approach used here. The high-pass ROC curves in Fig. 29 do not share a similarly discriminatory band of frequencies so their intersection with P_d=1 is more spread out.

Aside from the two widest bands, the other high-pass bands in Fig. 29 appear to produce comparable performance irrespective of the set of exemplars used except for the 20-30 kHz band. The 20-30 kHz band ROC curve shows degradation in classification when correlating with only the simulated exemplars. This indicates the simulated templates are not as good a set of exemplars as the pond templates in this band. The simulations performed for the mud environment involved both model and environmental assumptions (e.g., burial depth, mud attenuation level, etc.) that would be expected to be less certain at higher frequency so this departure may reflect that uncertainty.

As a final template-matching study, class separating the UXO in Table 6 as a function of the aspect range available on detections was considered. Here, it is recognized that, to efficiently search large areas, sonar usually detects objects on the seafloor while conveyed past them along linear tracks. Unless objects are detected multiple times along different non-parallel tracks, the range of target aspects available in the data collected is limited by sonar design parameters such as source and receiver beamwidths. To assess the effect of these limits on classification, Fig. 30 presents ROC curves obtained by correlating acoustic color plots that are truncated in aspect range with all exemplar templates in Table 7. Aspect angle windows of three widths ((a) 15°, (b) 30°, and (c) 45°) centered on seven aspects spaced 30° apart from 0° to 180° are considered. Correlations are computed over the full available frequency bandwidth of the plots. The maximum correlation of each window with each exemplar template is found by circularly shifting the aspect window relative to the template by a full 360° at angular steps corresponding to the angular resolution, computing a correlation at each shift, and saving the maximum correlation found. This process takes into account that, in aspect windows processed from real data, the orientation of the detected object is unknown so the correct corresponding windows on the exemplar templates to match to would be unknown. Therefore, it is assumed that the correct window to match to can be found by shifting in aspect angle until the maximum correlation is found. A Matlab routine using fast Fourier transforms was written to do this efficiently as a convolution. For each window width, seven ROC curves are superposed in Figs. 30(a)-(c) to show how classification varies as the window center is changed to another aspect.

A number of observations can be made from inspection of Fig. 30, some fitting expectations and others requiring further study. As expected, the worst classification performance is consistently centered on the nose-on aspect. UXO typically exhibit low SNR at this aspect so correlations with UXO templates are likely to be noisy and low. Also to be expected, better classification performance is achieved with the wider windows and, in both the 45° and 30° windows, one of the best aspects to center on is broadside (90°). Broadside is typically the aspect with the highest SNR and elastic activity excited at this aspect is likely to produce spectral phenomena unique to man-made target types. However, the best aspect for classification appears to be 30° from nose-on. This contrasts with performance at 150° (i.e., 30° from the tail-end), which is noticeably worse. While this result is less easily explained, it is hypothesized that the nearby nose-on target

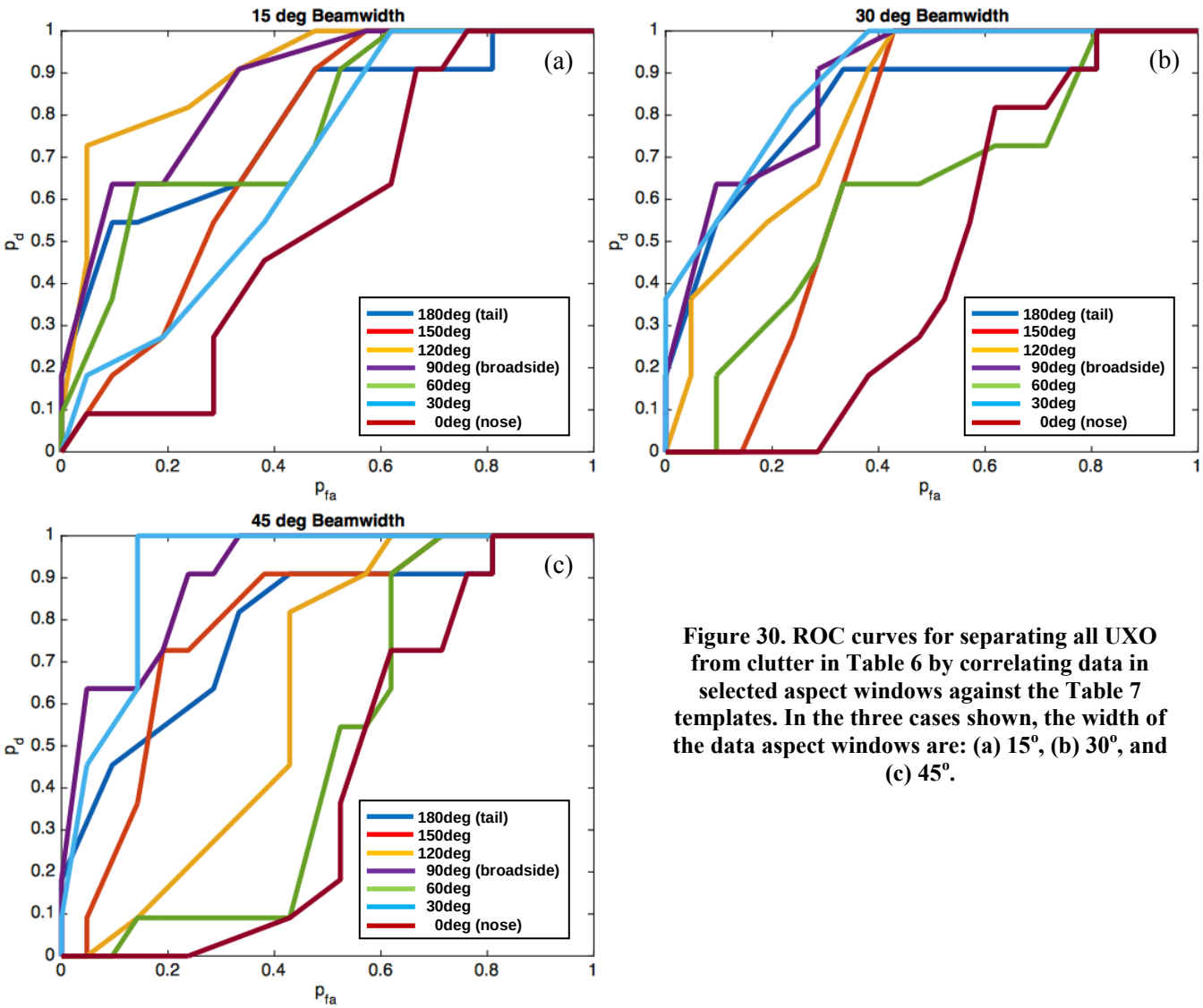

Figure 30. ROC curves for separating all UXO from clutter in Table 6 by correlating data in selected aspect windows against the Table 7 templates. In the three cases shown, the width of the data aspect windows are: (a) 15°, (b) 30°, and (c) 45°.

strength null characteristic of UXO enables higher UXO correlations with the flexural resonances near 30°. Correlations are weaker at the 150° aspect because the tail structure causes spectral highlights that are more variable among the UXO and interfere with the flexural resonance correlations near 150°. The influence of the nose/tail null/highlights to the off-axis ROC curves is consistent with results when the aspect window is narrowed to 15°; i.e., the narrower window reduces the influence of the nose or tail so the ROC curves at 30° and 150° become more similar.

The results above provide a look at how sensitive classification performance based on acoustic color template matching is to sonar frequency, aspect range, and template choices. The trends seen help isolate regions of acoustic color plots with the highlights most discriminating for UXO. Of course, further validation of these trends is needed with more diverse environments and target sets to define performance with better statistics.

Classification analysis of high grazing angle data:
When SNR is low and classification features are best extracted from strong SNR target aspects, template matching with TFD plots might provide a feasible feature. In this regard, Mr. R. Arrieta and Ms. I. Paustian made an effort to find TFD representations of broadside aspect data that best exhibit signal components associated with elastic radiation, especially resonances, which tend to have stable characteristics potentially useful for classification. After testing several distributions on available pond data, two distributions appear most promising: the binomial and the Born-Jordan. These two distributions display more structure than standard spectrograms and, therefore, appear better suited for template and feature matching.

Figure 31 illustrates examples of binomial TFD plots of circular rail data collected at the test pond using a solid aluminum replica of a 100 mm UXO target. Figure 31(a) corresponds to the target being placed proud of the bottom whereas Fig. 31(b) is for a partially buried configuration. Both plots are obtained by averaging time-aligned received signals within $\pm 3^{o}$ of broadside to increase SNR and possibly improve the robustness of phenomena observed near broadside. The averaged result is time windowed to isolate the target signal, cross-correlated with a replica of the transmitted chirp, scaled to remove source and receiver effects, and then processed using the TFD method. By processing the cross-correlated chirp, the resulting TFD is rotated in the time-frequency plane so that the portions of a TFD plot irrelevant to the target can be easily cropped out. Results are plotted in terms of frequency versus relative time. Figure 31 exhibits a rich structure distinguishing the two burial configurations.

Figure 32 shows an example of a Born-Jordan TFD plot of the proud 100 mm Al replica circular rail data for comparison. Of note here is that an elastic whispering gallery wave, identified by comparison with predictions of a cylinder model, can be isolated in this distribution.

A target database of TFD distributions of broadside target scattered signals has been created using data obtained from the Circular Rail facility at NSWC-PCD. Numerous UXO (100 mm, 105 mm, 155 mm shells) and clutter (WSU paddle, 2-to-1 solid cylinder and pipes, tire, cinder block, rock, and crab trap) objects are represented in the database. Since buried target detection and identification often deals with signals of low SNR but remains an important goal, initial investigations have concentrated on the broadside return because it provides a higher SNR scattered signal that can be easily modeled and understood for many axisymmetric UXO. Figure 33 gives examples of the binomial TFD for some of the targets in the database.

The differences seen in Fig. 33 would suggest template matching applied to TFDs could be effective in separating UXO and clutter in data collected under realistic conditions. This was tried using a correlation-based approach like that used with acoustic color plots by utilizing the pond TFDs to separate UXO in high-grazing angle data collected at TREX with the Bottom Object Scanning Sonar (BOSS). This downward looking sonar was deployed at TREX to collect data from the TREX target field under ONR support. Figure 34 is a BOSS beamformed and mosaicked image of the TREX target field, showing the limited resolution available for classifying the UXO detected. Data were collected in the 5-23 kHz band. A source pulse replica produced by the system, collected under other SERDP funding for calibration purposes, was used to deconvolve BOSS system responses out of the TFDs. Unfortunately, the TREX data were found to be under-sampled and tended to produce aliasing artifacts in the TFD processing

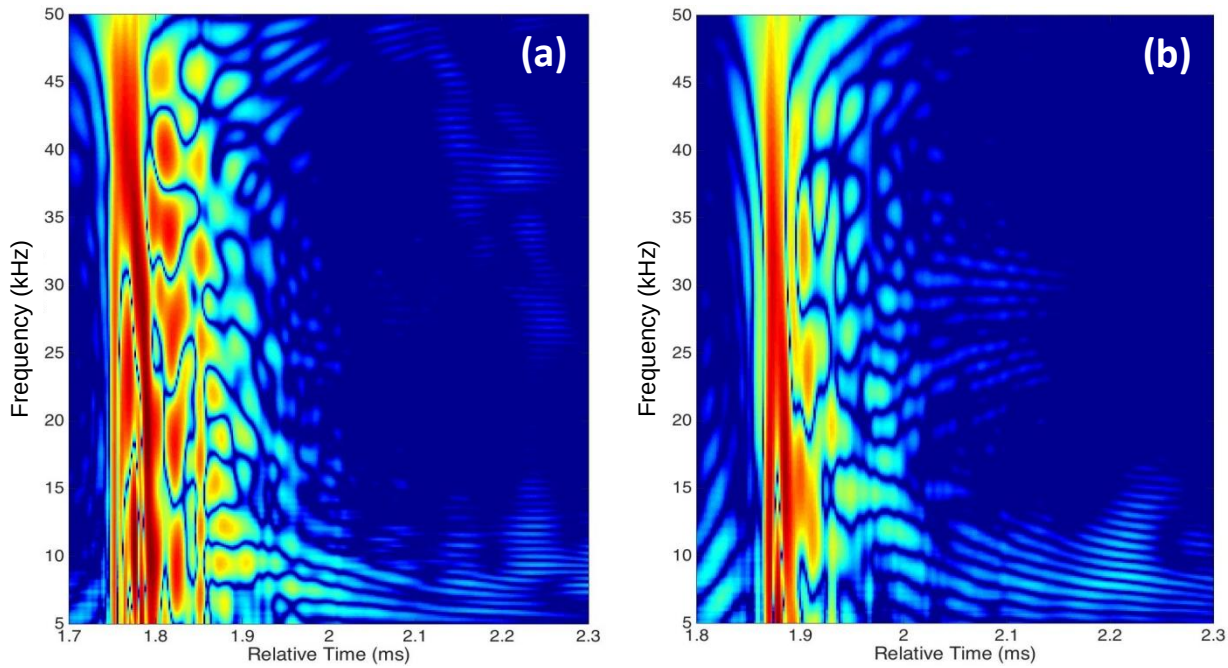

Figure 31. Binomial TFD plots of circular rail test pond data for an aluminum replica of a 100 mm UXO target. (a) Proud. (b) Partially buried.

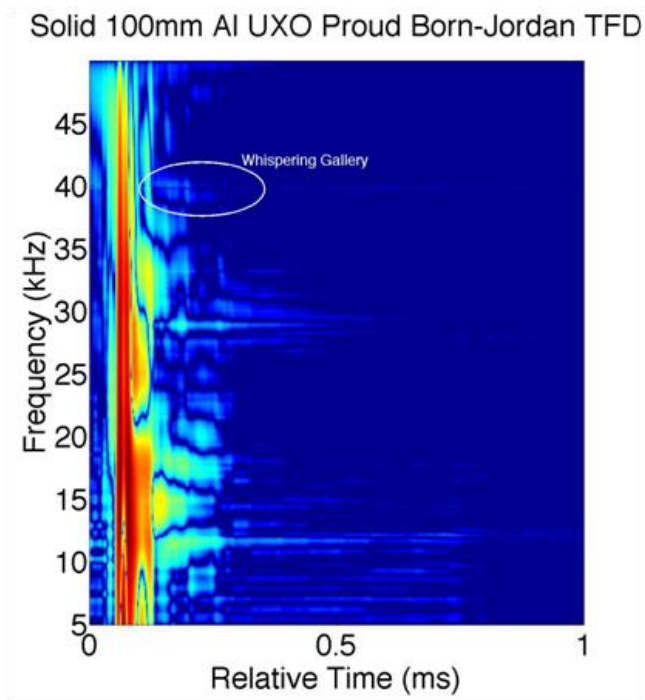

Figure 32. Born-Jordan TFD plot of circular rail test pond data for a proud aluminum replica of a 100 mm UXO target. A whispering-gallery wave is exhibited in this TFD.

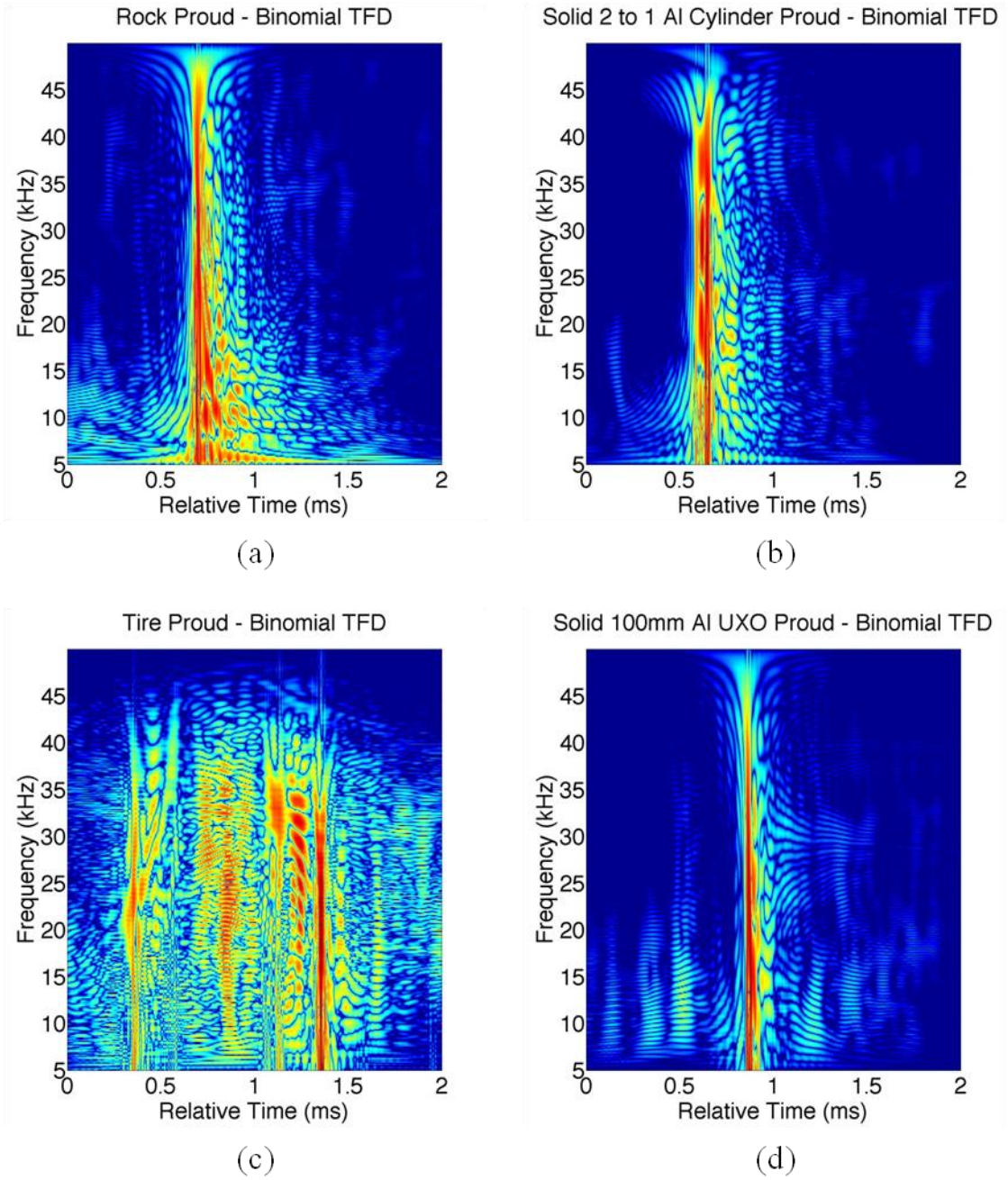

Figure 33. Binomial TFD results for 4 target types.

that made it hard to use the level of correlation as a feature consistently. Therefore, a different approach was tried to extract physics-motivated features related to dynamics that remain robust to environmental changes such as burial state. Potential dynamics considered were elastically excited surface wave and resonance phenomena.

A technique previously used to classify UXO detected at high grazing angles [1] was adapted for use with the Buried Object Scanning Sonar (BOSS) data collected at TREX and at a previous SERDP-funded experiment with UXO buried in St. Andrew Bay. Arietta originally demonstrated the technique to be successful classifying UXO by using feature vectors made up of properties of

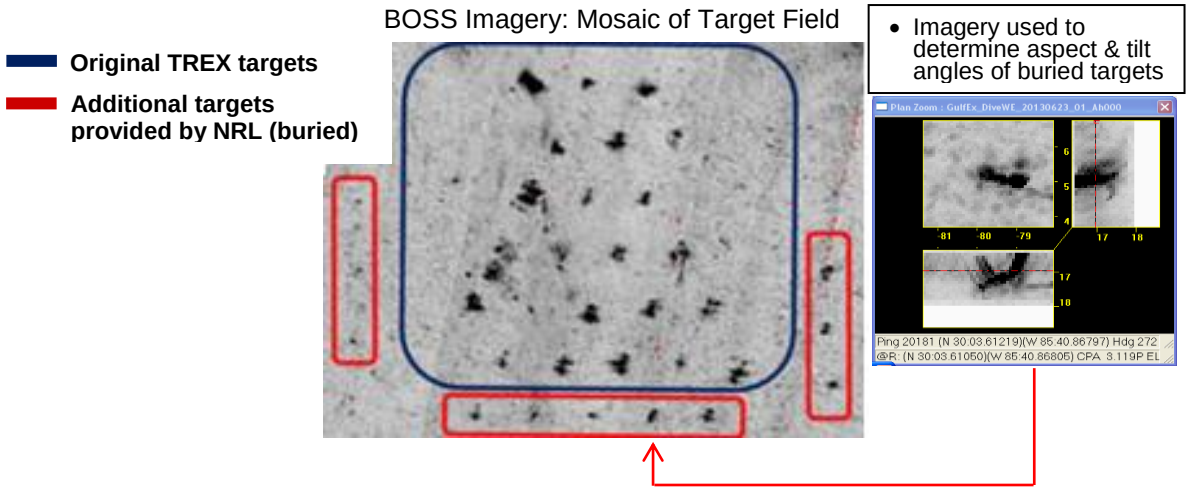

Figure 34. Beamformed and mosaicked image of TREX field from the BOSS system.

spectral peaks associated with axially guided elastic waves excited on elongated targets. In current work, he has adapted it to use properties of pseudo-Rayleigh (PR) and whispering gallery (WG) waves that propagate circumferentially on axisymmetric UXO shapes of metallic construction. The reason for focusing on these circumferential waves is that PR and WG waves will be observable when detection is biased towards the highest SNR target aspects such as broadside (e.g., by burial). As an initial test of this approach, high-grazing-angle data collected from a linear rail in NSWC PCD's pond facility was used to show that metallic UXO could be detected and localized in a non-imaging fashion by keying on spectral characteristics of broadside PR or WG waves that appear in Fourier transforms computed in short time windows shifted along collected pings.

On metal objects, the observed PR and WG waves are of a transverse nature and produce dips in the power spectrum (the frequency response) of the object (Figs. 35-36). These dips are due to the strongly leaky nature of these waves along their circular paths and their destructive interfere with the specular waves in the back direction. This leakiness (radiation into the medium as the wave circumnavigates the object) is characteristic of metallic targets where the transverse wave speed in the metal is higher than the sound velocity in the surrounding fluid. On most nonmetal axisymmetric objects, the resonances express themselves as peaks in the power spectrum and algorithms tuned to ignore peaks can, therefore, be written to distinguish metallic from nonmetallic axisymmetric objects. Studies carried out based on standard scattering models of cylinders and cylindrical shells of various composition embedded in various matrices indicate this difference is very pronounced and applies not only to solid axisymmetric objects, but also to thick-walled shells. The ability of PR and WG waves to propagate on buried corroded and encrusted objects has also been tested in scaled test tank experiments. These experimental results indicate these waves are robust to these types of changes (although their position may vary). Other wave types such as the guided helical waves seem to be completely attenuated in our scaled experiments with buried targets. By comparing model results with published examinations of the resonances of similar targets, a fairly robust algorithm that uses PR and WG waves as a means of classifying proud and buried objects of interest has been designed and implemented.

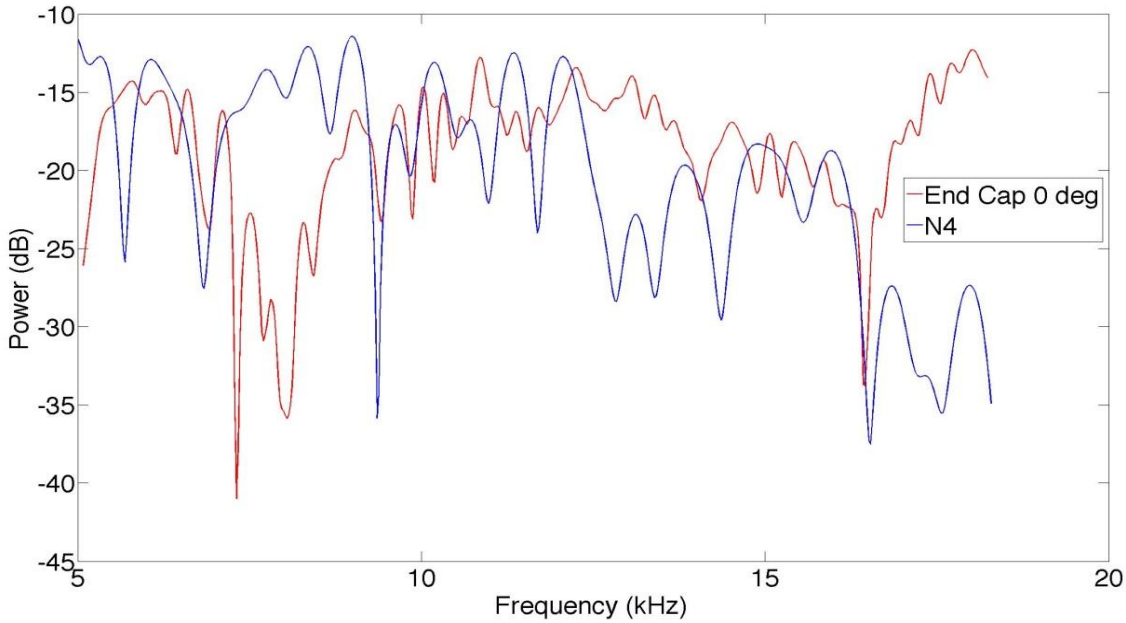

Figure 35. Target type N4 data from Pond and TREX

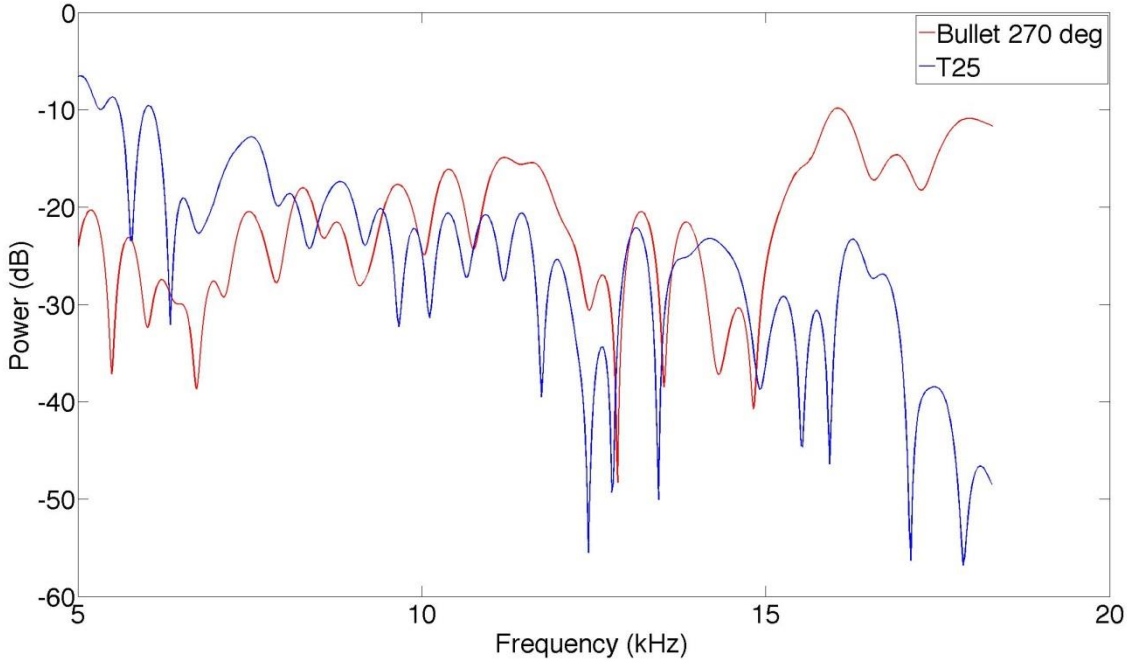

Figure 36. Target type T25 data from Pond and TREX

In work performed, progress was made in developing a technique for extracting PR and WG wave information from a sample of BOSS data collected over the TREX experimental field and establishing target characterization with data collected with the circular rail in NSWC PCD's freshwater pond facility. For buried targets, single aspect power spectra from high energy returns were found to be easiest to correlate between different systems. Reasonably good matches were found between BOSS and circular rail data by extracting broadside aspect power spectra from the circular rail data. Therefore, algorithms to automate finding and classifying the PR and WG excitations that are characteristic of metal objects insonified in a broadside backscatter configuration (direction of sound wave normal to long axis of object) were developed. The algorithms were configured to search the BOSS data for targets and then automatically pick their strongest ping response (associated with the broadside aspect) and extract the optimal time window to create their power spectra. The intent is to obtain spectra that are minimally affected by other objects and yet have a high enough frequency resolution to display the WG and PR elastic responses. WG resonance and PR wave spectra can be distinguished by their sharpness. Using estimated derivative spectra, the spectra of these two elastic effects can be reliably differentiated. Based on this differentiation, routines were developed to automatically locate, count, and compute spectral widths for each wave type and create a list of these characteristics from which to extract features for classification.

Figures 35 and 36 compare power spectra processed from the BOSS and circular rail data for two targets. Figure 37 illustrates the positions and widths of the spectral dips associated with PR and WG elastic excitations extracted by applying the automatic routines described above to both data sets in Fig. 36. Initial feature vectors utilized to distinguish between target types were constructed with elements based on parameters such as the number of spectral dips, relative positions, and amplitudes associated with each of these two wave types. The burial conditions for deployed targets varied between the two data collection sites so matching the exact location and amplitude of spectral dips is generally not effective for classification. Instead, class separation

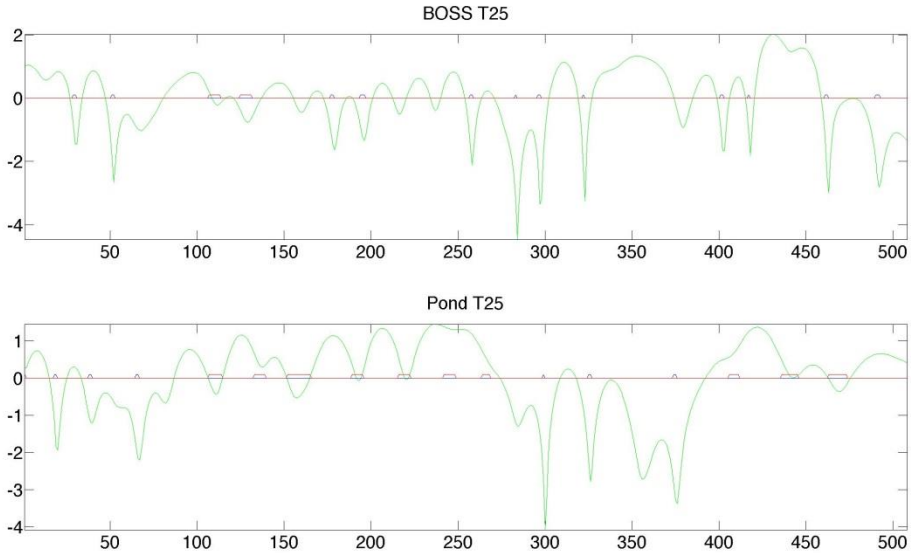

Figure 37. Power spectra of the same target collected by different systems in two underwater environments with sand sediment. The WG-PR sequences are marked on the red line.

was investigated by finding a two-dimensional frequency plane to project feature vectors onto, where target projections cluster away from clutter projections. Thus, relative similarities in the spectra were exploited, which resulted in positive matches made with all the target types detected with BOSS for which there was circular rail data. This included two low intensity targets on the starboard side of the BOSS imagery that were not as well "illuminated" due to the positive roll of the vehicle.

To further demonstrate that fairly simple feature vectors based on elastic response characteristics can be effective in classifying targets, BOSS data from five buried 155 mm Howitzer shells in the TREX field are considered. The lower frequencies used by the BOSS in order to penetrate attenuating sediments do not allow it to compete with commercially available sonar in imaging resolution, but, as seen in Fig. 34, the BOSS is still capable of determining gross dimensions and burial depth. For these buried targets, various feature vectors based on the sequences of PR and WG wave spectra and the gross dimensional and depth information were extracted and assessed for their performance in class separating the Howitzers from other detections.

Currently, the automatically generated lists of PR and WG spectral characteristics are used to create a five dimensional vector for each target. Then, the vectors are transformed using principal coordinate analysis in order to create a 2-D representation of the feature space. Although classification could be performed with the full-dimensional data, visualization and physical understanding is better accomplished in the reduced 2-D plane. Several such 2-D projections have been found where these buried shells gather into compact regions. Figure 38 shows one such 2-D principal coordinate representation. Figure 39 shows the result of applying k-means clustering to the target feature projections on this plane. While the clustering algorithm does group the Howitzers in a compact cluster (indicated with black asterisks), a few cylindrical proud targets are also included. Figure 40 shows how including burial depth information to the feature vector further enhances the separation. Adding burial depth to the feature vector, and reprocessing the principal coordinate data through k-means clustering, creates a cluster that contains only the buried 155 mm shells. This cluster is very well separated from the other clusters in the TREX field.

The TREX BOSS data set used to demonstrate these results is more limited than the data sets available at shallow grazing angles so further work utilizing broadside pings from the shallow angle data sets would be worth trying. Current work suggests features associated with elastic responses have high discrimination potential but automating the process to find and extract characteristics of these responses (e.g., relative time delays, spectral positions, spectral widths, spectral amplitudes, spectral intervals, dip count, peak count, etc.) can require tuning that depends on a good understanding of how the environment or detection configuration can modify the response. Whether the PR and WG elastic responses are significantly affected by the grazing angle needs to be ascertained. This will be a focus of future work.

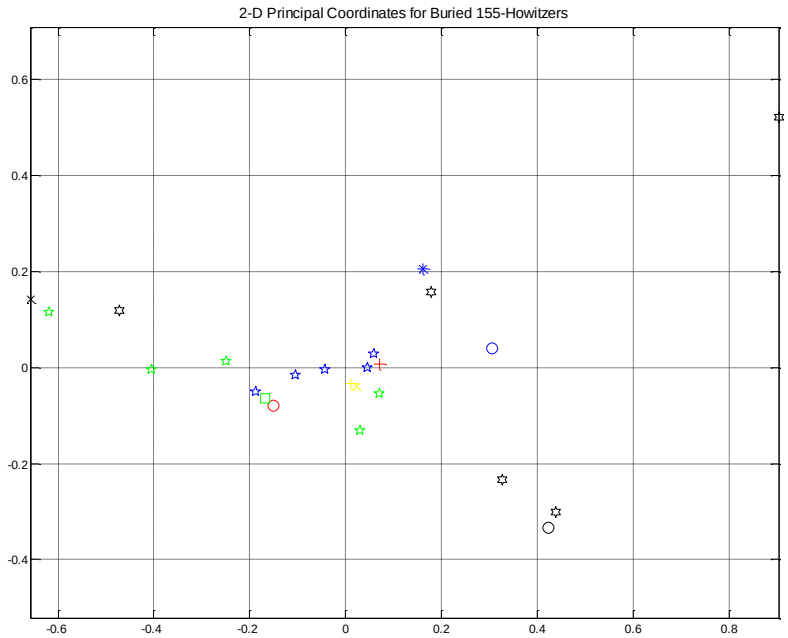

Figure 38. 2-D Principal Coordinate plane created by transforming 4-D feature vectors. The blue stars are buried 155 mm Howitzer shells.

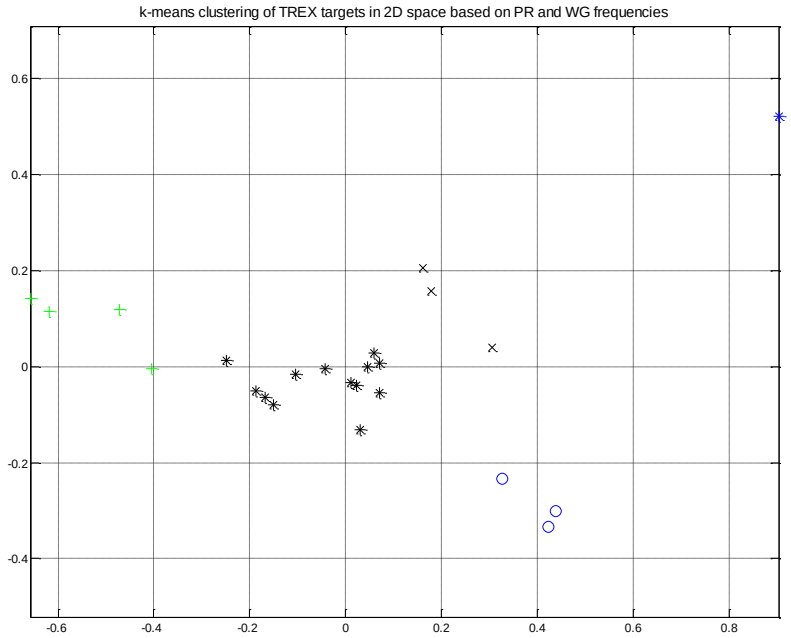

Figure 39. k-means clustering based on 2-D Principal Coordinates. The black asterisk cluster contains all buried 155 mm Howitzers along with a few cylindrical proud targets.

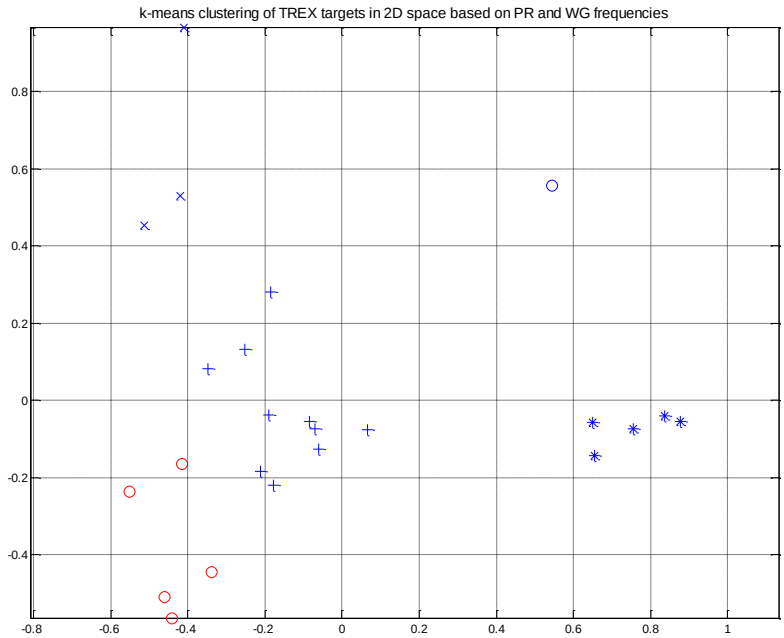

Figure 40. k-means clustering based on 2-D Principal Coordinates where an estimate of the burial state was included in the feature vector for each target. Burial state can be determined from the beamformed volumetric created by beamforming BOSS data. Adding burial state as an element in the feature vector before principal coordinate analysis separates the buried Howitzers (blue asterisks) from the other targets in the field.

Conclusions and Implications for Future Research/Implementation

For SERDP project MM-2230, NSWC PCD carried out data collection, data processing, data simulation and target modeling, and ATR processing to advance current capabilities to classify underwater UXO with sonar. A critical component of these efforts was supporting the TREX and BAYEX field measurements in 2012-2014. Data collected from UXO in 2012 established the feasibility of using APL-UW's rail system to collect sonar data from small targets deployed in an open ocean environment and the data collected in 2013 provided ground-truthed field data for ATR analysis of UXO and clutter deployed on sand sediment. Completion of the 2014 BAYEX data collection and processing provided ground-truthed field data for ATR analysis of UXO and clutter deployed on mud sediment. These data have been processed into imagery, acoustic color plots, and time-frequency plots for analysis. When added to the UXO target responses collected in NSWC PCD's pond, a growing database of measurements is being created from which physics-based feature extraction can be utilized to make classification more reliable and ATR algorithms can be tested. Further data collection efforts such as the continuation of data collection efforts in new field environments are recommended. Plans for deployment of APL-UW's rail in a cluttered area of St Andrews Bay off Panama City, FL in 2016 should provide useful additional data if carried out and completed.

In addition to the collection of field data, computational tools to simulate target responses on a large scale have been built and continue to be checked against the TREX and BAYEX data to

augment the target database being developed. Key components of these computational tools are having the right combination of accuracy and speed, which are difficult to achieve simultaneously. Because simulating the intrinsic target response is felt to be critical to the extraction of ATR features, this has received some attention by modeling the full 3D dynamics of a target, taking steps to make sure convergence is achieved, and making an effort to obtain accurate dimensional and material inputs. However, to allow for faster simulations, schemes that approximate the coupling of the target response to the environment have been implemented to produce data sets quickly that don't require additional long 3D FE runs for bottom deployed targets when only seafloor properties are varied. For simpler shapes, improved analytic models have also been formulated to speed up target response computations and extend their frequency range beyond that available with 3D FE. Given the cost of data collection and the extensive data requirements typically needed to properly train ATR algorithms, the development and use of these computational tools are expected to be of great value. Although making sure the approximations implemented are appropriate requires further checking, they will enable augmentation of ATR databases to a degree practical for ATR training/testing and interpretation of target acoustics in a timely fashion so that robust ATR features may be found. It is anticipated that robust features will significantly lower training data requirements.

A simple correlation analysis was devised to analyze the shallow-angle TREX and BAYEX data for classification potential based on matching acoustic color plots of the data to templates processed from controlled pond experiments or simulations. So far, results suggest that, at least for backscatter data with sufficient SNR over a large range of target aspects, projecting data onto acoustic color space yields good potential for class separating the UXO from clutter. Although model results show a definite dependence of acoustic color on range sampling (e.g., see Figs. 20-21), it was observed that exemplar templates were not needed at many ranges to achieve reasonable class separation of UXO. This may be a consequence of the limited scattering configurations at TREX and BAYEX. Also, anomalous cases like those depicted in Figs. 15-16 were not included in the analyses so far. Still, studies focused on the importance of particular frequency bands and aspect ranges suggest classification may be more strongly influenced by highlights exhibited at lower frequencies and particular aspects. The regions indicated are correlated with the occurrence of low frequency flexural excitations common to elongated UXO shapes. Further analyses of these trends with more diverse data sets are needed to be conclusive.

Use of templates from simulated data was also seen to be quite feasible provided relevant environmental and material inputs are available to generate the data. UXO in selected data sets chosen to mimic sonar reconnaissance of contaminated sites with mixed mud and sand sediment separated reasonably well using simulated data for the mud environment to generate exemplar templates. Compared with the use of pond templates for sand sediment, the simulated results for mud often produced better ROC curves for class separating the UXO. This is consistent with having more mud deployed targets to class separate and may reflect an environmental influence. Further studies with environmentally diverse data sets are needed to verify this influence.

The search for viable ATR features for low SNR data, such as encountered with buried targets, was also considered in time-frequency space and with feature vectors derived from backscattered PR and WG waves. Broadside aspect pond and TREX target data collected with the BOSS system were processed using several TFD types to identify the most discriminating

representations. So far, processing issues with the BOSS data have made matching BOSS TFD plots with pond TFD templates problematic but developing algorithms to extract characteristics of PR and WG waves seen in the TFD plots to use as components of a feature vector proved more successful for isolating target class. This was demonstrated by using a clustering algorithm to isolate the Howitzer shells detected by BOSS at TREX.

Elastic reradiation is often observed in acoustic echoes from man-made objects and is known to have spectral or spatial characteristics unique to target construction. The clustering analyses carried out in this project showed that these characteristics can be exploited for classification of particular UXO. The correlation analyses also suggest the aspect and frequency ranges of low frequency flexural modes in acoustic color plots can play an important role in classification of bullet shaped UXO. Furthermore, in both of these studies, there appears to be value in including some other information about the orientation or deployment configuration; e.g., enough aspect range in acoustic color windows to distinguish nose-on from tail-on orientations or target depth in feature vectors used in cluster analysis. The results seen so far would suggest feature vectors composed of both characteristics of elastically reradiated responses as well as deployment/orientation parameters available from imagery of desired targets would be worth constructing and testing in future work. However, elastic reradiation due to target vibrational modes or surface guided waves is often weak compared to specular echoes, is sometimes mixed in with these echoes, is not always radiated in the back direction, is not uniformly excited at all aspects, and can be contaminated by reverberation or confused with diffractive effects. Mitigating these issues requires understanding the elastic responses to be utilized well enough to develop algorithms capable of isolating the relevant responses reliably so that features can be extracted. Even if a feature vector of elastic response characteristics appropriate for all aspects is not possible, it may be possible to construct several to cover a range of most aspects and/or fuse them with image-based vectors.

Literature Cited

[1] R. Lim, “Sonar Detection and Classification of Underwater UXO and Environmental Parameters,” SERDP PROJECT MR-1666 Final Report, 2012

[2] K. L. Williams, S. G. Kargl, E. I. Thorsos, D. S. Burnett, J. L. Lopes, M. Zampolli, P. L. Marston, “Acoustic scattering from a solid aluminum cylinder in contact with a sand sediment: measurements, modeling, and interpretation,” *J. Acoust. Soc. Am.* **127**(6), 3356-71, 2010.

[3] S. G. Kargl, K. L. Williams, T. M. Marston, J. L. Kennedy, and J. L. Lopes, “Acoustic Response of Unexploded Ordnance (UXO) and Cylindrical Targets,” Proceedings of MTS/IEEE Oceans 2010, Seattle, WA, Sept. 20-23, 2010.

[4] P. C. Waterman, “T-matrix methods in acoustic scattering,” *J. Acoust. Soc. Am.* 125, 42-51 (2009).

[5] A. Doicu, Y. Eremin, and T. Wriedt, Acoustic & Electromagnetic Scattering Analysis Using Discrete Sources, Academic Press, London, 2000.

[6] B. Boashash, editor, "Time–Frequency Signal Analysis and Processing: A Comprehensive Reference", Elsevier Science, Oxford, 2003, ISBN 0-08-044335-4.

[7] G. C. Gaunaurd and M. F. Werby, "Similarities between Lamb waves in submerged spherical shells, and Rayleigh waves in elastic spheres and flat halfspaces," *J. Acoust. Soc. Am.* **89**, 2731-2739, 1991.

[8] J. L. Kennedy, T. Marston, K. Lee, J. L. Lopes, and R. Lim, "A rail system for circular synthetic aperture sonar (CSAS) imaging and acoustic target strength measurements: design/operation/preliminary results," *Rev. Sci. Instrum.* **85**, 014901 (2014); doi: 10.1063/1.4861353.

[9] J. L. Kennedy and T. Marston, "Multipass and Non-Concentric Target CSAS," SERDP MR-2439 annual report submitted Jan 2015.

[10] D. S. Plotnick, P. L. Marston, K. L. Williams, and A. L. España, "High frequency backscattering by a solid cylinder with axis tilted relative to a nearby horizontal surface," *J. Acoust. Soc. Am.* **137**, 470-80, 2015.

[11] APl.-UW High-Frequency Ocean Environmental Acoustic Models Handbook, Applied Physics Laboratory University of Washington Technical Report APL-UW TR 9407, Seattle, WA, October 1994; J. E. Moe, "Near and Far-Field Acoustic Scattering through and from Two Dimensional Fluid-Fluid Rough Interfaces," Applied Physics Laboratory University of Washington Technical Report TR 9606, Seattle, WA, October 1996.

[12] R. H. Hackman, "The transition matrix for acoustic and elastic wave scattering in prolate spheroidal coordinates," *J. Acoust. Soc. Am.* **75**, 35-45, 1984.

[13] R. H. Hackman and D. G. Todoroff, "An application of the spheroidal-coordinate-based transition matrix: The acoustic scattering from high aspect ratio solids," *J. Acoust. Soc. Am.* **78**, 1058-1071, 1985.

[14] A. Boström, "Scattering of stationary acoustic waves by an elastic obstacle immersed in a fluid," *J. Acoust. Soc. Am.* **67**, 390-398, 1980.

APPENDIX A: Supporting Data

List of FEM models built

1. 2 by 1 ft Aluminum Cylinder : (3) Proud on sand sediment, Half Buried in sand sediment, Tilted (20.5^o) : Grazing angle 21.35^o, Aspect angle from 0 to 180° by increasing 1° , frequency range from 5 kHz to 50 kHz by increasing 0.2 kHz.
2. 2 by 1 ft Pipe of Aluminum and Steel : (6) Proud on sand sediment, Half Buried in sand sediment, Tilted (20.5^o) : Grazing angle 21.35^o, Aspect angle from 0 to 180° by increasing 1°, frequency range from 5kHz to 50kHz by increasing 0.2kHz.
3. 105 mm Bullet : (3) Proud on sand sediment, Half Buried in sand sediment, Tilted (55°) with no filler : Grazing angle 21.35^o, Aspect angle from 0 to 180° by increasing 1°, frequency range from 5 kHz to 50 kHz by increasing 0.2 kHz.
4. 100 mm Replica UXO of Aluminum and Steel : (6) Proud on sand sediment, Half Buried in sand sediment, Tilted (55°) with no filler : Grazing angle 21.35^o, Aspect angle from 0 to 180° by increasing 1°, frequency range from 5 kHz to 50kHz by increasing 0.2 kHz.
5. 155 mm Howitzer shell : (6) Proud on sand sediment, Half Buried in sand sediment, Tilted (55°) with end cap, no filler and with no end filled with water, cap no filler : Grazing angle 21.35^o, Aspect angle from 0 to 180° by increasing 1° , frequency range from 5 kHz to 50 kHz by increasing 0.2 kHz.
6. Multiple targets (two Howitzers filled with water and a tilted Bullet 105 mm filled with water) : (1) Proud on sand sediment, Grazing angle 21.35^o, Aspect angle from 0 to 180° by increasing 1°, frequency range from 2 kHz to 30 kHz by increasing 0.2 kHz.
7. 500 lb bomb Head : (3) Free Field, Proud on sand sediment, Tilted (10°) : Grazing angle 11.5^o (0° in freefield) , Aspect angle from 0 to 180° by increasing 1°, frequency range from 2 kHz to 30 kHz by increasing 0.1 kHz.
8. 500 lb bomb without internal part in tail tube : (3) Free Field, Proud on sand sediment, Tilted(10°) : Grazing angle 11.5^o (0° in free field), Aspect angle from 0 to 180° by increasing 1°, frequency range from 2 kHz to 30 kHz by increasing 0.1 kHz.
9. 500 lb bomb with internal part in tail tube : (3) Free Field, Proud on sand sediment, Tilted (10°) : Grazing angle 11.5^o (0° in freefield), Aspect angle from 0 to 180° by increasing 1°, frequency range from 2 kHz to 30 kHz by increasing 0.1 kHz.
10. Generic shell target : (2) in Free Field filled with half water and half sand , filled with only water : Grazing angle 0°, Aspect angle from 0 to 180° by increasing 1°, frequency range from 2 kHz to 30 kHz by increasing 0.2 kHz.
11. Generic shell target : (2) Proud on sand sediment filled with half water and half sand, filled with only water : Grazing angle 21.8^o, Aspect angle from 0 to 180° by increasing 1°, frequency range from 2 kHz to 30kHz by increasing 0.2 kHz.
12. Paddle (Notched Cylinder) : (4) in Free Field (up notch , 45° rotated notch), Proud on sand sediment (25° rotated notch), Flush (25° rotated notch) : Grazing angle 21.35^o (0° in free field), Aspect angle from 0 to 360° by increasing 2°, frequency range from 3 kHz to 50 kHz by increasing 0.2 kHz.
13. Cylindrical Shell : (8) Proud on mud and sand sediments with 4 Grazing angles (0.573, 1.146, 2.291, 4.547)^o, Aspect angle from 0 to 180° by increasing 1°, frequency range from 1 kHz to 30 kHz by increasing 0.05 kHz.
14. Cylindrical Shell : (8) 1/3 Buried in mud and sand sediments with 4 Grazing angles (0.573, 1.146, 2.291, 4.547)^o, Aspect angle from 0 to 180° by increasing 1°, frequency range from 1 kHz to 30 kHz by increasing 0.05 kHz.
15. Cylindrical Shell with Hemispherical EndCaps: (1) Free Field with Grazing angle 20°, Aspect angle from 0 to 180° by increasing 1°, frequency range from 1 kHz to 50 kHz by increasing 0.1 kHz.
16. Rock Clutter Models : (3) Proud on sand sediment (the same length and aspect ratio of 100 mm UXO replica, 105 mm Bullet, and 155 mm Howitzer) Grazing angle 21.35^o, Aspect angle from 0 to 180° by increasing 1°, frequency range from 1 kHz to 30 kHz by increasing 0.1 kHz.
17. Rigid Models : (2) in Free Field (100 mm Aluminum UXO replica , 105mm Bullet Steel) with Grazing angle 20°, Aspect angle from 0 to 180° by increasing 1°, frequency range from 5 kHz to 50 kHz by increasing 0.1 kHz.

18. Fully Buried : (3) 100 mm aluminum UXO replica (Flush, one inch below, and two inches below) in mud sediment, Grazing angle 21.35^{o}, Aspect angle from 0 to 180° by increasing 2°, frequency range from 3 kHz to 30 kHz by increasing 0.2 kHz.

APPENDIX B: List of Scientific/Technical Publications

Journal/Conference publications:

Kargl, S.G.; Espana, A.L.; Williams, K.L.; Kennedy, J.L.; Lopes, J.L., "Scattering From Objects at a Water–Sediment Interface: Experiment, High-Speed and High-Fidelity Models, and Physical Insight," *IEEE Journal of Oceanic Engineering*, vol.PP, no.99, pp.1,111, doi: 10.1109/JOE.2014.2356934,

M. Zampolli, A. L. Espana, K. L. Williams, S. G. Kargl, E. I. Thorsos, J. L. Lopes, J. L. Kennedy, and P. L. Marston, "Low- to mid-frequency scattering from elastic objects on a sand sea floor: Simulation of frequency and aspect dependent structural echoes," *J. Comp. Acoust.*, **20**, 2012.

R. Lim, D. E. Malphurs, K. H. Lee, J. L. Kennedy, and J. L. Lopes, "Comparisons of SAS Processed Data from Ordnance Replicas over Various Size Scales: Experiments and Acoustic Models," Proceedings of MTS/IEEE Oceans 2012 Conference, Hampton Roads, VA, October 2012.

J. L. Kennedy, T. M. Marston, K. Lee, J. L. Lopes, and R. Lim, "A rail system for circular synthetic aperture sonar imaging and acoustic target strength measurements: Design/operation/preliminary results," *Rev. Sci. Inst.*, **85**, 2014.

R. Lim, "A more stable transition matrix for acoustic target scattering by elongated objects," accepted for publication in *J. Acoust. Soc. Am.* (copy attached).

Conference/Symposium Abstracts:

R. Lim, "A new T matrix for acoustic target scattering by elongated objects in free-field and in bounded environments," *J. Acoust. Soc. Am.*, **136**(4) Pt. 2 of 2, 2087, 2014.

R. Lim, D. E. Malphurs, J. L. Prater, K. H. Lee, and G. S. Sammelmann, "A correlation analysis of the Naval Surface Warfare Center Panama City Division's (NSWC PCD) database of simulated and collected target scattering responses focused on automated target recognition," **136**(4) Pt. 2 of 2, 2112, 2014.

R. Lim, "A New T Matrix for Acoustic Target Scattering by Elongated Objects in Free-field and in Bounded Environments" submitted for 170th Meeting of the Acoustical Society of America, Jacksonville, FL, November 2015.

David E. Malphurs, Raymond Lim, Kwang Lee, and Gary S. Sammelmann, "Correlation Trends in NSWC PCD's Database of Simulated and Collected Target Scattering Responses Focused on Automated Target Recognition" submitted for 170th Meeting of the Acoustical Society of America, Jacksonville, FL, November 2015.

A more stable transition matrix for acoustic target scattering by elongated objects[1]

Raymond Lim, Naval Surface Warfare Center Panama City Division, Panama City, FL

Running title: Transition matrix for elongated objects

ABSTRACT

The transition (T) matrix of Waterman has been very useful for computing fast, accurate acoustic scattering predictions for axisymmetric elastic objects but this technique is usually limited to fairly smooth objects that are not too aspherical unless complex basis functions or stabilization schemes are used. To ease this limitation, a spherical-basis formulation adapted from approaches proposed recently by Waterman [*J. Acoust. Soc. Am.* 125(1), 42-51 (2009).] and Doicu, et al. [*Acoustic & Electromagnetic Scattering Analysis Using Discrete Sources*, Academic Press, London, 2000] is suggested. This is implemented by simply transforming the high-order outgoing spherical basis functions within standard T-matrix formulations to low-order functions distributed along the object's symmetry axis. A free-field T matrix is produced in a nonstandard form but computations with it become much more stable for elongated aspherical elastic shapes. Some advantages of this approach over Waterman's and Doicu, et al.'s approaches are noted and sample calculations for a 10:1 Al prolate spheroid and a 10:1 Al superspheroid of order 10 are given to demonstrate the enhanced stability.

PACS numbers: 43.20.Fn, 43.30.Gv

[1] Submitted to J. Acoust. Soc. Am. 27 Apr 2015.